

Development of a fast readout system for the DISC DIRC prototype of PANDA

**Dissertation zur Erlangung des
Doktorgrades der Naturwissenschaften**
im Fachbereich 07
(Mathematik und Informatik, Physik, Geographie)
der Justus-Liebig-Universität Gießen

vorgelegt von
İlknur Köseoğlu-Sarı

II. Physikalisches Institut
Justus-Liebig-Universität Gießen

Gießen,
June 2021

For my mother and father..

Abstract

PANDA is one of the four major experiments at the future *Facility for Antiproton and Ion Research* (FAIR) in Darmstadt, Germany. The physics goal of PANDA is to better understand unknown phenomena in the non-perturbative QCD region, the structure of hadrons including the strong and weak forces. The program of PANDA is planned to be studied at different momenta of the antiproton beam during collisions with a fixed proton target. After the antiproton-proton annihilation, all possible decay products are to be detected using a hermetic 4π detector. The PANDA detector is designed as double spectrometer. The forward spectrometer utilizes several subdetectors including a dipole magnet. The target spectrometer is designed in the form of an onion shell structure with a combination of compact subdetectors such as a calorimeter, a tracking system with magnets and muon identification. Since a classical hadronic calorimeter is missing, charged hadrons are discriminated by two DIRC (Detection of Internally Reflected Cherenkov light) in a barrel and disc shape to cover the polar angle range from 5° to 140° .

The world's first disc-shaped detector Endcap Disc DIRC (EDD) is a part of particle identification of the PANDA system to cover the polar angle range 5° to 22° . The separation power of charged pions and kaons is aimed to have 3 standard deviations up to $4\text{ GeV}/c$ momentum. When these charged particles traverse the fused-silica radiator of the EDD, Cherenkov photons are emitted and reflected internally to the readout system, thereby carrying the angle information of the charged particle. The hit pattern of Cherenkov photons will be detected via highly granulated Microchannel-plate photomultiplier tubes (MCP-PMTs), and the analog signals of the MCP-PMT anode pins will be digitized by a readout system. This thesis focuses on a development of a fast readout system of the EDD to achieve the specified performance.

The readout system of the EDD consists of the ASIC based TOFPET2 system which was designed by the PETsys company for PET applications. In order to improve the readout electronics for our purposes, deficiencies of the existing system were determined in different steps such as test beam experiments at CERN in 2018. The ASICs from 2018 production batch were further improved in an experimental test setup called Giessen Cosmic Station (GCS).

The GCS was built in the University of Giessen to use the cosmic muons with a selection of 600 MeV minimum energy as a generator of Cherenkov photons. It consists of scintillator bars to reconstruct the track of the cosmic muons. The GCS was continuously enhanced by designing a light-tight cases for optical elements, and by changing the air-cooling into more stable liquid cooling for electronics. A full-sized EDD quadrant was integrated into the GCS setup. By using optimized ASICs, data was acquired with a triggerless system similar to the one used in PANDA. Data analysis confirmed by Monte Carlo (MC) shows the expected detection performance of the readout system.

The custom PCB which will be used for the final EDD in PANDA was designed in a tight collaboration with PETsys company by implementing only the required electronic elements and removing the ones related to SiPM applications. Thereby radiation hardness, communication with the PANDA central DAQ system, and compatibility to the

magnetic field had to be newly considered. In addition to that, the readout system of the final EDD has to fit into a compact space. This limits the possible positions of the electronic elements with different dimensions. Regarding all spatial constraints, one design was chosen out of three different suggested designs considering the number of readout modules in the available space.

One of the critical issues is keeping temperature of the electronics in a compact PCB around 20° . For that, a permanently running liquid cooling system was designed. After the production of the custom design PCB, a light-tight experimental setup was prepared for testing purposes with permanent magnets depending on test purposes. The readout system with the presented designs and implementations reached a powerful state that allows for pursuing the next phases of the PANDA project.

Contents

List of Acronyms	v
1. Introduction	1
2. PANDA at FAIR	3
2.1. Facility for Antiproton and Ion Research (FAIR)	3
2.2. PANDA experiment	5
2.2.1. Target system	5
2.2.2. Tracking system	6
2.2.3. Magnets	9
2.2.4. Calorimetry	10
2.2.5. Particle Identification	12
2.2.6. RICH Detector	14
2.2.7. Barrel TOF	14
2.2.8. Muon Range System	14
2.2.9. Luminosity Detector	15
2.2.10. Data Acquisition	15
2.2.11. Physics Program	20
3. Particle Identification and Cherenkov Detectors	23
3.1. Particle Identification (PID)	23
3.1.1. Energy Loss	23
3.1.2. Time of Flight	26
3.1.3. Cherenkov Radiation	27
3.2. Cherenkov detectors	29
3.3. DIRC Detectors	32
3.3.1. Detectors based on focusing concepts	33
3.3.2. Imaging Time of Propagation Detector in Belle-II	33
3.3.3. TORCH at LHCb	34
4. The Disc DIRC Detector	35
4.1. Working principle of the EDD	35
4.2. The setup of the detector	36
4.3. Assembly	39
4.4. Mechanical Components for EDD	41
4.5. Spatial Constraints	42
4.6. Sensor choice	44

Contents

4.7. Readout System	48
4.7.1. Overview of the Front-end Electronics	48
4.7.2. Frontend Electronics	50
4.7.3. The TOFPET2 Readout	50
4.7.4. The readout system of the final EDD for Phase-2	53
4.8. Custom PCB design for the final readout system	56
4.8.1. Custom PCB test	57
5. Giessen Cosmic Station	67
5.1. Introduction	67
5.2. Mechanical Components of GCS	70
5.2.1. GCS construction	73
5.3. GCS readout system	77
5.4. Results of the GCS Data Analysis	78
5.4.1. Performance of the SiPM Boxes	78
5.4.2. The Performance of Radiator	81
6. CERN Beam Time Experiments	89
6.1. Introduction	89
6.2. Testbeam Results	90
6.2.1. Prototype Components	90
6.2.2. Preparation of the Optical Elements	91
6.2.3. Data Acquisition	94
6.2.4. Offline Analysis	96
6.2.5. Position and Momentum Scans	100
7. Summary and Outlook	115
A. Appendix	117
List of Figures	129
List of Tables	131
Bibliography	138

List of Acronyms

- ADC** Analog-to-Digital Converter
- ALD** Atomic Layer Deposition
- APD** Avalanche Photo Diode
- ASIC** Application-Specific Integrated Circuit
- CAD** Computer Aided Design
- CERN** European Organization for Nuclear Research
- CMOS** Complementary metal-oxide-semiconductor
- CR** Collector Ring
- DAQ** Data Acquisition
- DC** Data Concentrator
- DCR** Darkcount Rate
- DIRC** Detection of Internal Reflected Cherenkov Light
- dSiPM** Digital Silicon Photomultipliers
- EDD** Endcap Disc DIRC
- EMC** Electromagnetic Calorimeter
- FAIR** Facility for Antiproton and Ion Research
- FEE** Front-End Electronics
- FEL** Focusing Element
- FET** Field Effect Transistor
- FSC** Forward Spectrometer Calorimeter
- FPGA** Field Programmable Grid Array
- FS** Forward Spectrometer

Contents

GEM Gas Electron Multiplier
GSI Gesellschaft für Schwerionenforschung
HEP High Energy Physics
HESR High Energy Storage Ring
LAPD Large Area Photo Diode
LINAC Linear Accelerator
LHC Large Hadron Collider
LHCb Large Hadron Collider bottom quark
MCP Microchannel Plate
MDT Mini-Drift Tube
MOSFET metal-oxide-semiconductor field-effect-transistor
MVD Micro Vertex Detector
PANDA Antiproton Annihilation at Darmstadt
PASTA PANDA Strip ASIC
PCB Printed Circuit Board
PET Positron Electron Tomography
PLL Phase Locked Loop
PID Particle Identification
PMT Photo Multiplier Tube
RESR Recycled Experimental Storage Ring
RICH Ring Imaging Cherenkov Detector
RMS Root Mean Square
ROM Readout Module
SciTil Scintillator Tile
SiPM Silicon Photomultiplier
SIS Schwerionen-Synchrotron
SLAC Stanford Linear Accelerator

SM Standard Model of Particle Physics

SODA Synchronization of Data Acquisition

STT Straw Tube Tracker

TDC Time to Digital Converter

TDR Technical Design Report

TOF Time of Flight

TOFPET Time of Flight Positron Electron Tomography

ToT Time over Threshold

TOP Time of Propagation

TRB TDC Readout Board

TS Target Spectrometer

QED Quantum Electrodynamics

QCD Quantum Chromodynamics

VHDL Very High Speed Integrated Circuit Hardware Description Language

1. Introduction

The present work covers the implementations and studies for a fast readout system of the Endcap Disc DIRC (EDD) which is a subdetector of PANDA (Antiproton annihilation in Darmstadt) experiment. The goal of the PANDA experiment is to explore the non-perturbative region of QCD which can be studied in the energy regime of charm mesons. Many subdetectors are required in PANDA to study this physics program. Details of the PANDA detector and its physics program are discussed in Chapter 2.

The PANDA detector utilizes different types of subdetectors to separate true signals from background noise. Different particle identification techniques are also discussed in Chapter 3. Since no hadronic calorimeter will be used, two DIRC detectors were developed for hadron identification. DIRC is an abbreviation of Detection of internally reflected Cherenkov light. DIRC detectors are a specific type of a Cherenkov detector that make use of the Cherenkov effect to determine the particle velocity. Their working principle is similar to a Ring Imaging Cherenkov detector (RICH). The design of the Barrel DIRC for PANDA is adopted from the BaBar DIRC. The DIRCs will identify all hadrons in the polar angle range between 5° and 140° in the barrel [PANDA17b] and endcap region. The particle identification techniques and the different designs of the DIRC detectors are detailed in Chapter 3.

The Endcap Disc DIRC (EDD) is a novel design of a DIRC detector with a disc-shaped radiator and the electronics at the outer rim. It covers the polar angles at the endcap region between 5° and 22° . Chapter 4 deeply investigates the EDD detector regarding working principle, mechanical design, spatial constraints, sensor choice, readout system etc. The thesis mainly focuses on the readout system of the EDD. The current readout of the EDD is based on TOFPET2 system which is designed by PETsys company for other types of applications. It is a fast readout system based on specialized electronics such as ASICs, FPGA, etc. In Chapter 4, the current design and the target design of the readout system are explained. The final design of the FEE is discussed in detail considering the requirements of the spatial constraints and environmental factors such as magnetic field and radiation hardness. The design was done by PETsys company according to our specifications. To test this custom PCB design for the readout system, a magnet box was developed. The magnet box is a light-tight system with a laser feedthrough provided to lighten the sensor surface at different positions with short laser pulses. It allows testing the custom design PCB in a magnetic field provided by 8 permanent magnets at two edges with 500 mT magnetic field. This thesis is focused on the fast readout system of the prototypes, the mechanical structure of the light-tight cases, and data analysis of the test beam experiments compared to Monte Carlo simulations based on GEANT4.

The final design of the readout system and the quadrant of the EDD will be iterated and tested in the experimental setup called Giessen Cosmic Station (GCS). GCS was built

1. Introduction

to use cosmic muons with a minimum energy of 600 MeV as generator of Cherenkov photons in a quadrant of the EDD. The setup consists of four tracking boxes to reconstruct the position and direction of muons hitting the radiator. The Cherenkov angle of individual photons can be reconstructed from the hit position in the photon Chapter 5 explains the elements, the construction of the GCS and the data analysis with Monte Carlo (MC) simulations.

In 2018, a rectangular version of the EDD prototype was tested at CERN. The preparation of the experiment, calibration and data acquisition are explained in Chapter 6. Offline data analysis was done to show the characteristic distribution patterns of Cherenkov photons. The last Chapter 7 summarizes the studies that have been done.

2. PANDA at FAIR

2.1. Facility for Antiproton and Ion Research (FAIR)

FAIR is a future international accelerator facility located at GSI¹ in Darmstadt. In Figure 2.1, a sketch of FAIR can be seen with the existing and future facilities labeled by blue and red color, respectively. FAIR will provide particle beams that create by collisions very different conditions such as extreme temperatures, high densities and pressures depending on the experiment type:

- **APPA**² is aimed to research cancer therapy with ion beams, plasma physics, radiation biology, material research, atomic physics and fundamental symmetries.
- **CBM**³ is an experiment to understand the nuclear matter under different extreme temperature and pressure conditions such as a neutron star.
- **NUSTAR** aims to understand the atomic nucleon structure, astrophysics and the reactions.
- **PANDA**⁴ aims to understand strong force, hadron structure and dynamics by annihilation and generation of new particles by using cooled antiproton beams.

The goal of constructing the new accelerators is to provide $7 \cdot 10^{10}$ cooled antiprotons per hour, an intense proton beam, ion beams of all elements and secondary beams of rare isotopes. In order to reach these goals, the Proton LINAC (p-LINAC), SIS100/300, HESR⁵ and CR Ring are in the phase of construction as can be seen in Figure 2.1. The existing parts are the UNiversal Linear ACcelerator (UNILAC), ring (SIS18⁶) accelerators and ESR. UNILAC has been designed to accelerate all types of ions up to 60,000 km/s, that is 20% speed of light, for being injected into the ring accelerator SIS18 [uni20]. The injected beam can then be accelerated to about 90% speed of light in the SIS18. The beam from SIS18 can be distributed to four experiments in parallel or stored in the storage rings. The ions beams are planned to be accelerated in UNILAC and ring accelerator SIS18. Afterwards, the ion beams can be stored in the Heavy Ion Storage Ring ESR at

¹Gesellschaft für Schwerionenforschung

²Atomic, Plasma Physics and Applications

³Compressed Baryonic Matter

⁴Antiproton Annihilation at Darmstadt

⁵High Energy Storage Ring

⁶Schwerionensynchrotron 18

2. PANDA at FAIR

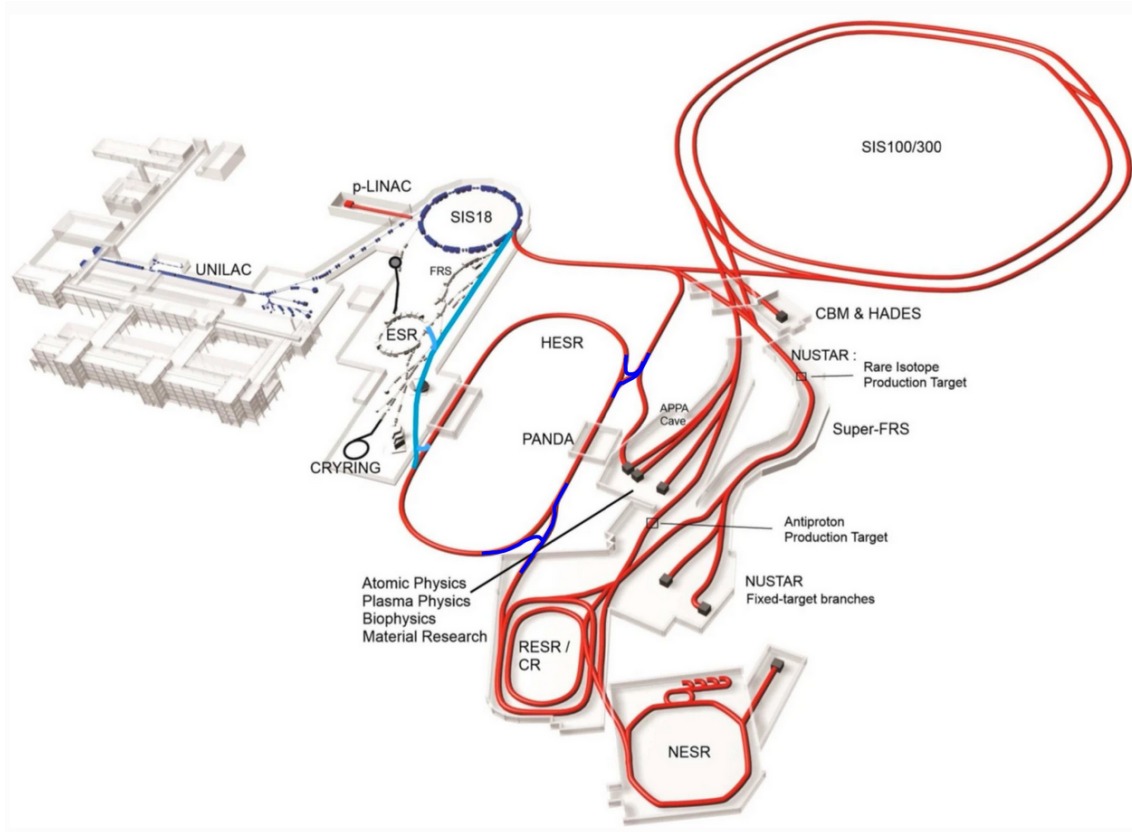


Figure 2.1.: The sketch of FAIR with existing facilities, planned facilities, and experiments [SSS15].

several million circulations per second. In future, the planned facilities will be used together with the existing facilities. UNILAC and p-LINAC will be operated together to accelerate protons up to 70 MeV and then send the beam to SIS100/300 with a magnetic rigidity of 100 Tm and 300 Tm, respectively. SIS100 and SIS300 are going to be built on the same tunnel with the same circumference [KPS⁺07]. SIS100 will provide 30 GeV protons with $2.5 \cdot 10^{13}$ intensity and $2.7 \text{ GeV/u } ^{238}\text{U}^{28+}$ with $4 \cdot 10^{11}$ intensity. SIS300 will provide $^{238}\text{U}^{92+}$ ions with $2 \cdot 10^{10}$ intensity between 35 GeV/u to 45 GeV/u energy. Highly energetic protons will collide with a metal target to create antiprotons. Antiprotons will be separated from protons and other secondary particles by using a magnetic horn and sent to the CR [SKS⁺12]. Afterwards, the antiproton beam will be cooled down and sent to HESR from the CR. Stochastic cooling and electron cooling are two important techniques [Dim14] to obtain a high beam quality for the two operation modes of the HESR: high luminosity (HL) and high resolution (HR) mode. However, high luminosity mode will be only available after RESR is constructed. The electron cooling can be done up to 9 GeV/c energy of antiprotons. The method is based on Coulomb scattering while the electrons and antiprotons have the same average velocity. The cooling can be done till

the electrons and the antiprotons approach the thermal equilibrium. Stochastic cooling can be applied at any momentum level of antiprotons. The idea is based on measuring and correcting the deviation of each antiparticle compared to the statistical mean value in a finite statistical sample.

2.2. PANDA experiment

The PANDA experiment [PAN05] will be operated at the HESR [Pra14]. The antiproton injection is done at a momentum of 3.8 GeV/c from the CR/RESR to the HESR with 574 m circumference. HESR provides an antiproton beam at different momenta range between 1.5 GeV/c to 15 GeV/c depending on the two operational modes which are the HL with a luminosity of $\mathcal{L} = 2 \cdot 10^{32} \text{ cm}^{-2} \text{ s}^{-1}$ and the HR mode with a momentum resolution of $\Delta p/p = 4 \cdot 10^{-5}$. In HR mode momentum range will change between 1.5 GeV/c to 8.9 GeV/c with a maximum number of 10^{10} antiprotons stored. For HL mode the momentum is changing from 1.5 GeV/c to 15 GeV/c with 10^{11} antiprotons stored [PANDA09c]. The PANDA detector setup as shown in Figure 2.2, is constructed as a combination of two different sub-spectrometers: the target spectrometer (TS) is in a shape of onion shell-like detector around the interaction point covered by a solenoid magnet and the forward spectrometer (FS) which covers small polar angles up to 5° and 10° in the vertical and the horizontal directions respectively. The goal is to achieve a 4π acceptance, an excellent particle identification, tracking, calorimetry, event selection and a central clock system to synchronize subdetectors for data recording. In the following sections all subdetectors with their working principles will be summarized to provide a better understanding.

Two different project phases have been planned for the PANDA experiment setup. During phase-1, some of the detectors will not be fully equipped. In Figure 2.2, the red labelled detectors will be upgraded for phase-2.

2.2.1. Target system

The target system of PANDA can be seen in Figure 2.3 where it crosses the beam pipe at the interaction point. The beamline provides antiprotons with a minimum energy of 1.5 GeV/c to a maximum 15 GeV/c momentum to make them collide with the fixed target which results in 5.5 GeV/c in the cm-system. The proton target is chosen to be made of hydrogen atoms. Depending on the experiments of a physics study, three different target systems are available which are the pellet target, the cluster jet target and the other target options (fiber target). In Figure 2.3, two different target systems are shown. In cluster jet target, pre-cooled and compressed hydrogen gas travels into Laval-type nozzle from a micro-sized throat that yields an adiabatic cool down. As a result gas reaches supersonic speed during condensation. Depending on the shape and the diameter of the nozzle, the size and the number of the clusters change. This is an advantage of controlling the cluster target since the luminosity, size and density can be controlled and the volume density distribution is homogeneous. Typically a cluster target consists of $1 \cdot 10^{15}$

2. PANDA at FAIR

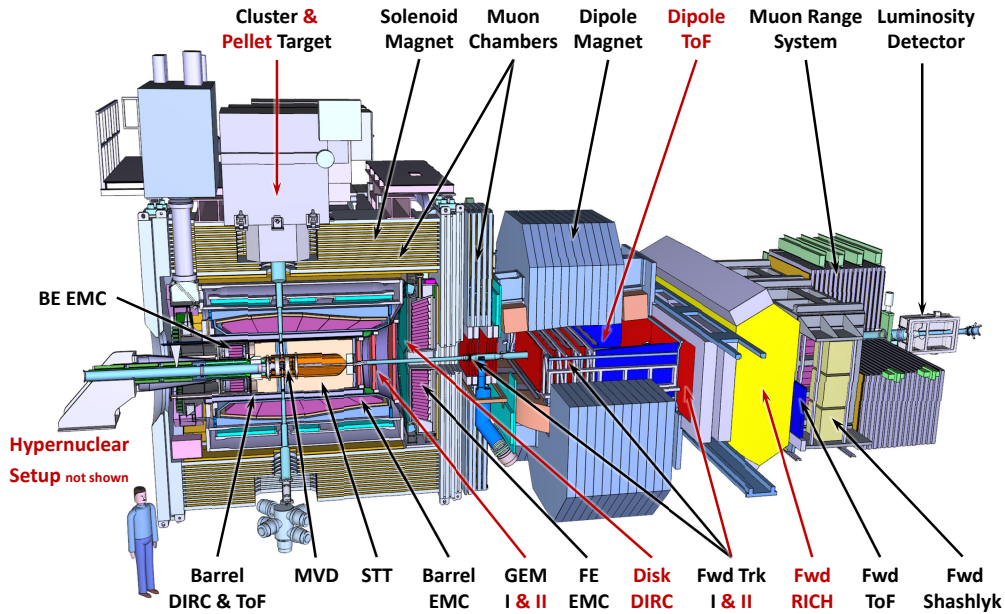


Figure 2.2.: The 3D drawing of PANDA detector [pan20a]. The detectors labeled in red will be installed in second phase of the project.

atoms/cm² [PANDA12].

The pellet target is the other internal target where hydrogen is injected into a triple point chamber throughout a vibrating nozzle. Due to nozzle vibrations, the size of the drops are similar to nozzle diameter. In order to exclude perturbing effects, the triple point chamber is filled with hydrogen. The pellet target may reach 5×10^{15} atoms/cm². In comparison to cluster jet target, the volume density distribution is not homogeneous but granular. The expected event rate is minimum 2 MHz and 20 MHz maximum. Since PANDA aims at reaching an interaction rate around 10 MHz during the high luminosity mode, it requires 4×10^{15} atoms/cm². This can be realized with a pellet target. As a conclusion both targets fulfill the requirements depending on the experimental conditions.

2.2.2. Tracking system

The tracking system of PANDA consists of four subdetectors. The goal is to discriminate the charged particles in a magnetic field using their tracking information. In the TS, a

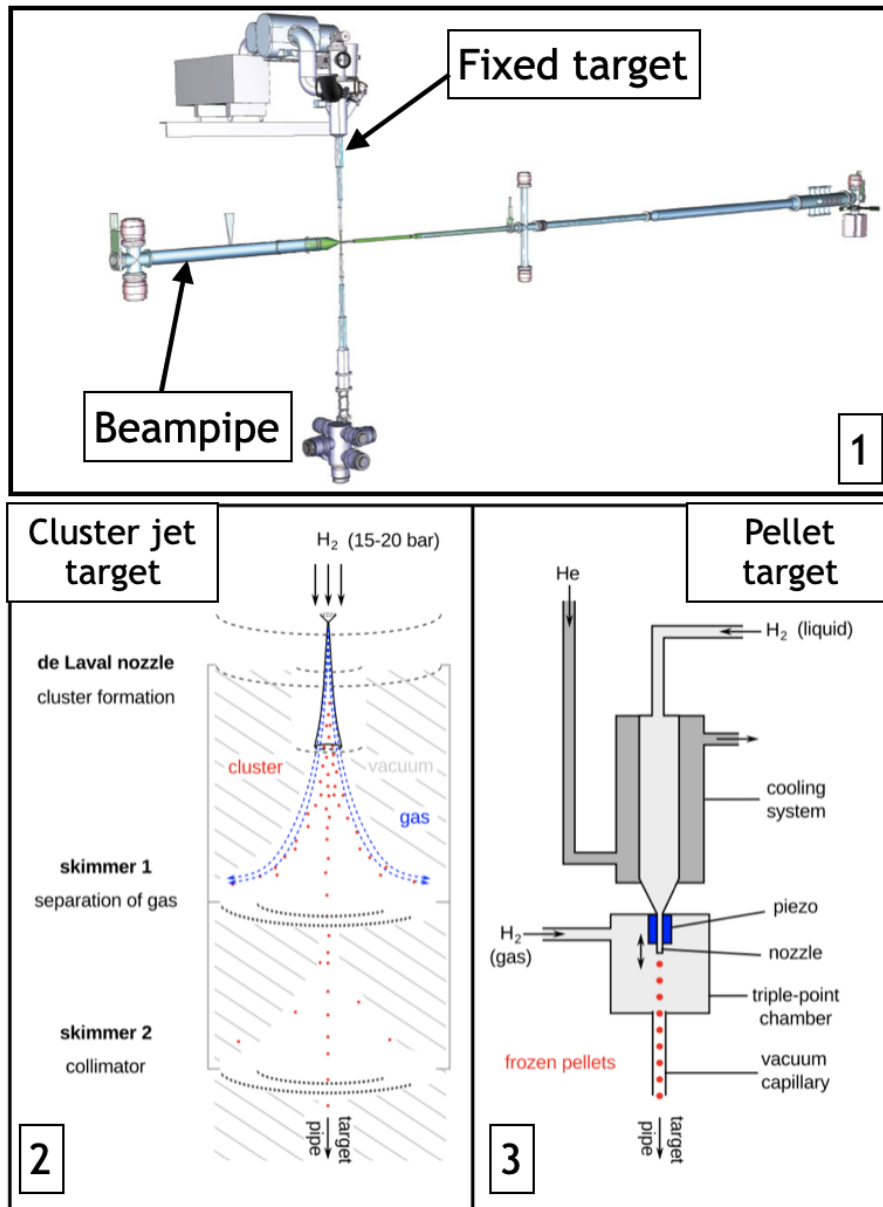


Figure 2.3.: First: The fixed target system with a beam pipe [tar20]. Second: Cluster jet targets are separated from a hydrogen gas via Laval-type nozzle and the skimmers. Third: The pellet target with a liquid hydrogen is turned out to be frozen pellets via cooling system, nozzle movements and triple-point chamber [Mer14].

silicon based Micro Vertex Detector (MVD), Straw Tube Tracker (STT), and Gas Electron Multiplier (GEM) are surrounded by a solenoid magnet which will be used for central

2. PANDA at FAIR

tracking. The particles with a small polar angle may not be detected properly since they leave the solenoid magnet before a proper measurement. These particles are planned to be detected in FS by using dipole magnet. This is called forward tracking.

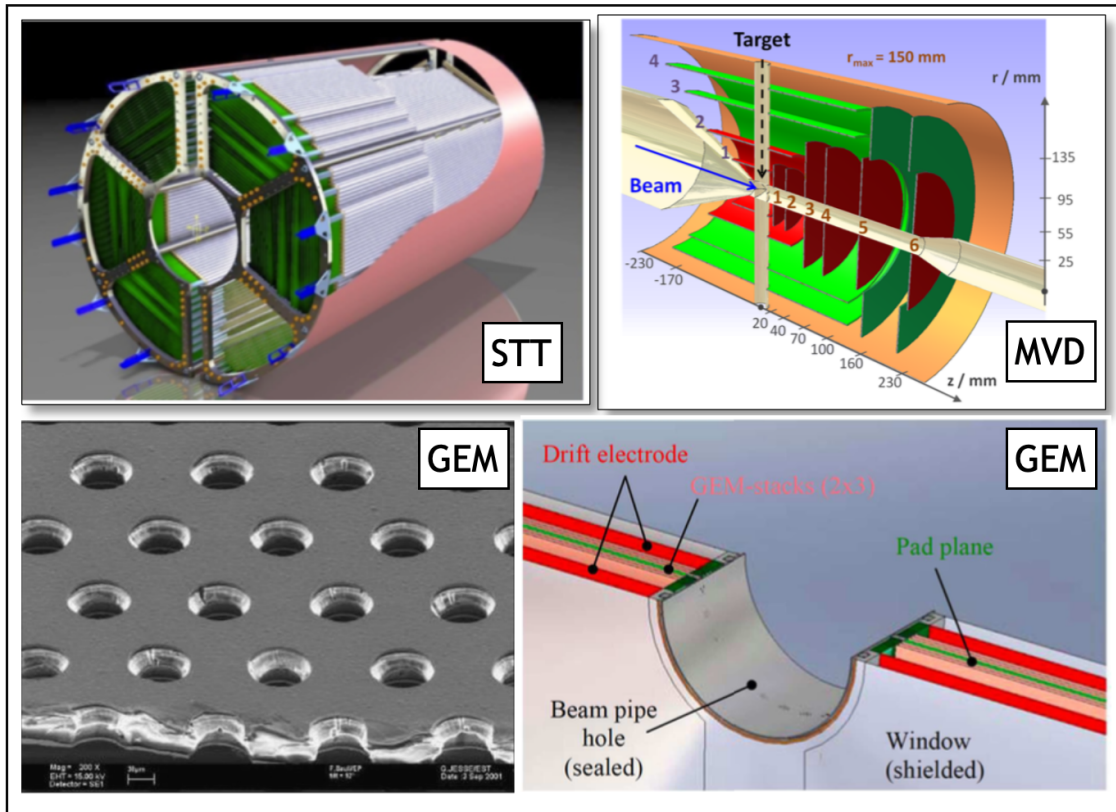


Figure 2.4.: The 3D drawings of the target detectors in TS of PANDA. Image sources STT [PANDA13], MVD [E⁺12], Electron microscope picture of a typical GEM structure photo [PANDA14], GEM 3D drawing

Micro Vertex Detector

The MVD is the closest detector to the interaction point. It provides 3D hit information with a precise timing of secondary decay vertices of charged particles. A precise timing of the MVD is crucial to assign the correct timing of a corresponding track of D mesons or hyperons which consist of a charm or strangeness [E⁺12]. In addition, the outer detectors can use MVD timing as a reference. MVD is made out of four barrel layers around the interaction point and six disks starting from 20 mm in z direction after interaction point. The disk layer cover polar angles between 3° to 40° where the barrel layers covers between 40° to 150°.

The innermost barrel layers and the four disks closer to the IP of the MVD will be

exposed to high number of particles. These layers will consist of silicon hybrid pixel detectors. The two outermost disks utilize the combination of pixel detectors in the inner radius and trapezoidal-shaped double-sided strips in the outer radius. The two outermost barrel layers use the double-sided silicon strip detectors.

Straw Tube Tracker

The STT will be built around the MVD detector. Its 4636 single straw tubes have 1500 mm length, 10 mm inner diameter and consist of a $27\mu\text{m}$ thin aluminum foil to make them self-supporting due to the inner pressure. Straws tubes are filled with a gas mixture of Ar and CO_2 at up to 2 bars of pressure to keep the straws in a cylindrical shape. There is a conductive inner layer in the straws as a cathode, and anode wire in the center. The goal of the STT is to provide a precise spatial reconstruction in helical trajectories of charged particles in the solenoidal field with a momentum range between 100 MeV/c and 8 GeV/c and specific energy-loss (dE/dx) for PID purposes. When a particle traverses STT, it ionizes the gas inside and creates an electrical signal. In order to have a precise position resolution the drift time is critical. While the electrons are drifting, more gas is ionized and causes an electron avalanche. As a result, a measurable signal occurs at the anode. This signal is transmitted to the readout system. The PID information from the STT will be used to separate protons, kaons and pions with a momentum region below 1 GeV/c [PANDA13].

GEM Detector

Three independent GEM (gas electron multiplier) detectors are positioned at the forward endcap region of TS just before EDD to cover the polar angle range from 5° to 22° . The goal is to achieve a precise tracking of long lived hadrons containing a charm and a strange quark which are not detected by the STT and MVD. Each layer of GEM is made of a kapton foil with thin copper layers on both sides. There are small holes inside the GEM detector that can be seen in the electron microscope photo at the bottom-left in Figure 2.4. When high voltage applied, an electric field created between the two sides of the holes. The particle track in the GEM ionizes the gas inside the detector and results an electron avalanche. These electrons are detected by an anode structure.

2.2.3. Magnets

In the PANDA experiment, a solenoid magnet in the TS and a dipole magnet in the FS are used. The strong magnets are crucial for PANDA to measure high-momentum charged particles. In the tracking region, the cryostat for the superconducting coil is covering all subdetectors in the TS and provides a homogeneous 2 T magnetic field with a uniformity of $\pm 1.6\%$ [PANDA09a]. The dipole magnet with 2 Tm bending power is positioned in the forward region to allow reconstruction of charged particles with a momentum resolution better than 1% in the vertical direction from 0° up to 5° and from 0° up to 10° in the horizontal direction. The figure 2.2 shows the cryostat and the dipole magnet in PANDA.

2. PANDA at FAIR

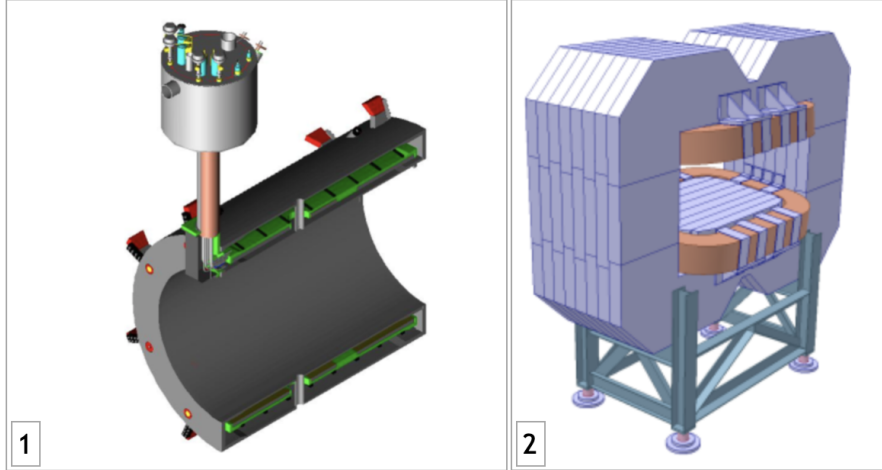


Figure 2.5.: The CAD drawings of Cryostat (left) [sol21] in TS and Dipole magnet (right) [dip21] in FS.

2.2.4. Calorimetry

In order to measure photons and electrons in PANDA, an electromagnetic calorimetry is built that covers most of the angular range and consists of differently shaped crystals depending on the position in the TS. The energy deposition of γ and lepton pairs are measured by stopping them in crystals made of inorganic material (PbWO_4). The aim is to obtain a precise measurement of an electron, positron, and efficient recognition of the light mesons to exclude the background at almost 4π coverage. The shape and alignment of the crystals are designed to force the particles to cross the medium by minimising the dead zones. It is planned to achieve an energy resolution of

$$\frac{\sigma_E}{E} = a \oplus \frac{b}{\sqrt{E/\text{GeV}}} \quad (2.1)$$

where $a \leq 1\%$, $b \leq 2\%$ and \oplus is a quadratic summation[PANDA08]. a is the constant term which dominates the equation at high energies.

Electromagnetic calorimeters can be seen in Figure 2.6. In the first CAD drawing the barrel EMC and disc shape-like endcap EMC with the crystals are shown. In the second drawing, the Forward Spectrometer Calorimeter can be seen with the crystals. The crystals are aligned in the same way. The third drawing shows a section cut of the backward endcap EMC (BE-EMC) which is equipped around the beampipe and MVD subdetector. The beampipe connects to interaction point where the beam crosses the fixed target. The crystals for all calorimeters use inorganic material that is made of lead tungstate (PbWO_4) in 200 mm length. The barrel calorimetry utilizes 11360 crystals, forward and backward endcap EMC uses 3600 and 592 respectively. The crystals have to be cooled down to -25° with a dedicated cooling system since the light yield depends on the temperature as -3% per $^\circ\text{C}$. The cooling system has to be insulated well to prevent a

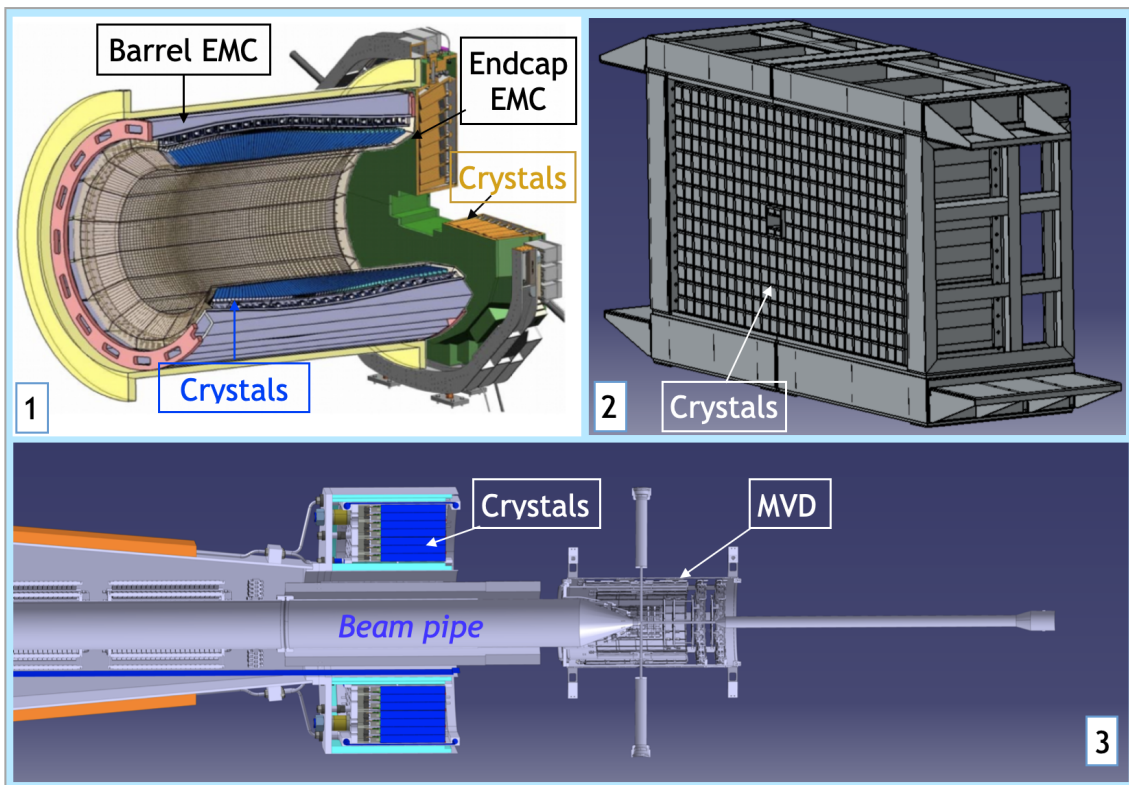


Figure 2.6.: The CAD drawing of the calorimeters in PANDA. 1: Barrel EMC and forward Endcap EMC with crystals [Alb15]. 2: 3D drawings from the step file from actual PANDA geometry, Shashlyk calorimeter in the FS. 3: Drawing of Backward Endcap EMC with crystals (blue), beam pipe and MVD tracking detector.

temperature gradient around the neighbor detectors and to stabilize the temperature inside. The readout system is based on APFEL⁷ ASICs that are connected to Large Area Avalanche Photo Diodes (LAAPDs) and Vacuum Photo TeTodes (VPTTs). The readout system is radiation hard and able to work within a magnetic field [PANDA08].

In addition to the TS, there is a shashlyk technology is chosen for FSC to detect electrons and photons. It is positioned behind the dipole magnet to cover an angular range up to 5° in the vertical and 10° in horizontal direction. The Shashlyk-type calorimeter in 3D CAD drawing is shown at second photo in Figure 2.6 with 378 modules. Each module has four independent cells with a dimension of $55 \times 55 \text{ mm}^2$. The calorimeter is made of a combination of passive and active elements which are lead plates as absorbers and

⁷ASIC for PANDA Front End Electronics

2. PANDA at FAIR

organic scintillator tiles. The energy resolution for shashlyk calorimeter is

$$\frac{\sigma_E}{E} = \frac{b}{\sqrt{E/\text{GeV}}} \oplus c \quad (2.2)$$

where $c \approx 1\%$ and $b \approx (2 \dots 3)\%$ [PANDA17c].

2.2.5. Particle Identification

In the PANDA experiment, a hadronic calorimeter is not used. Instead different subdetectors for particle identification in the TS and FS are used together. The tracking detectors and the calorimeters contribute to PID; however, the detection of charged hadrons requires special techniques achieved by dedicated subsystems. These subdetectors are combinations of two DIRC detectors, muon detectors, and time-of-flight for particle identification (Figure 2.7).

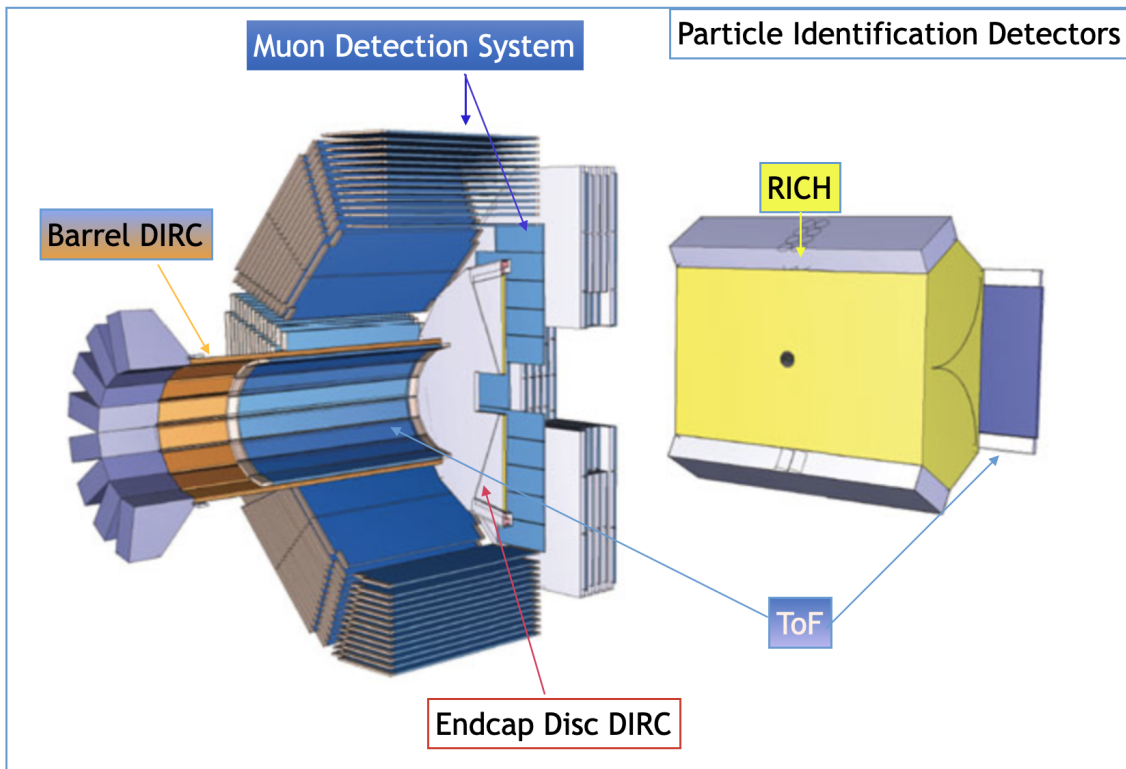


Figure 2.7.: PANDA subdetectors for particle identification in TS and FS [pan20a]. The beam is coming from the left.

The two DIRC detectors are positioned in the target spectrometer to measure Cherenkov photons. These photons are emitted by charged hadrons (pions, kaons, protons) traversing a transparent radiator with a momentum above 1 GeV/c. The required performance

of the DIRC detectors is a π/K separation of 3σ at $4\text{ GeV}/c$ momentum for polar angles $5^\circ < \theta < 22^\circ$. For larger polar angles of $22^\circ < \theta < 140^\circ$, 3.5σ separation power at $3.5\text{ GeV}/c$ is needed. The polar angle from 22° to 140° is covered by the Barrel DIRC (Figure 2.7). It is designed in a similar structure as in BABAR DIRC[A⁺05]. The details of the Barrel DIRC can be found in technical design report [PANDA17b] and some aspects will be discussed in the following chapters.

The PANDA Barrel DIRC

The PANDA detector utilizes a Barrel DIRC detector for particle identification in the polar angle range between 22° and 140° with 3 s.d. up to $3.5\text{ GeV}/c$ momentum. In order to cover such a large polar angle range, the barrel DIRC utilizes a bar-shaped fused silica radiator with 2400 mm length (two 1200 mm bars are glued in the longitudinal direction). Three radiator bars are enclosed as a sector and 16 sectors are available in total as shown in Figure 2.8. Each sector is coupled to a three-layer spherical lens which has a middle layer made of N-LaK33B glass [3la21] sandwiched between two fused silica layers [S⁺20]. It has a defocusing and focusing effect to provide a flat focal plane where Cherenkov photons enter a 300 mm deep fused silica prism and hits a 2×4 MCP-PMT array. PADIWA discriminator boards are directly plugged onto the anodes of the MCP-PMTs. The time of arrival and time over threshold signals from these boards are measured by Trigger Readout Board version 3 (TRB3) of the HADES collaboration [U⁺13]. A flat mirror is placed at the end of the bar to reflect the Cherenkov photons back to focusing elements.

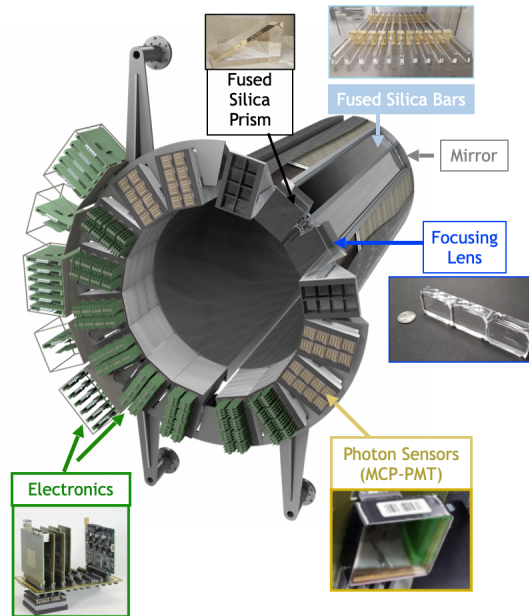


Figure 2.8.: Barrel DIRC with its fundamental elements.

2. PANDA at FAIR

The performance of the Barrel DIRC was confirmed during the test beam experiments at different facilities. The analysis results from the test beam at CERN, in 2018 were published [PANDA20].

The PANDA Endcap Disc DIRC

The Endcap Disc DIRC (EDD) is a novel design detector as a disc-shaped to occupy less space of the polar angle range from 5° to 22° in the forward region. The working principles of the EDD is similar to the other DIRC detectors in spite of the different detector design. Details of the EDD are described in Chapter 4.

2.2.6. RICH Detector

The RICH (Ring Imaging CHerenkov) Detector is used to detect particles with higher momenta in the FS. These particles create Cherenkov photons in a non-homogeneous aerogel radiator.

2.2.7. Barrel TOF

The Barrel TOF system utilizes the mechanical support of the Barrel DIRC and it covers a polar angle range between 22° and 140° . It is made of 16 independent sections (called super-modules) which consist of sensitive area, signal transmission lines and electronics in a $24600(L) \times 180(W) \times 20(T)$ mm³ volume. The readout system is based on a scintillator tile module connected to four serial SiPMs. The signals are digitized by the TOFPET2 ASICs, the readout system used for the EDD [Z⁺19].

2.2.8. Muon Range System

The muon range system consists of an iron-scintillator sandwich installed in the return yoke of the solenoid in the barrel and forward endcap region. In the barrel region, the muon range system consists of 13 sensitive layers with a thickness of 3 cm (only the 'zero' layer is 6 cm thick). In the forward endcap region, six detection layers are positioned around five iron layers of 6 cm thickness. The muon filter is sandwiched also in the magnet doors where it provides a magnetic screen between the cryostat of the TS and the dipole magnet in the FS. Rectangular-shaped aluminum Mini Drift Tubes (MDT) are used as sensors. It provides good spatial and time resolution with negligible aging effect. The performance of the MDT was approved in different experiments such as D0 at Fermilab or COMPASS at CERN. The MDT uses Iarocci streamer tubes with Ar/CO₂ (70/30%) gas mixture. The Frontend electronics is based on ASICs amplifier and discriminator [PAN12]. The muon range system in forward region will be also used to discriminate muons and pions using their tracking information [PAN12].

2.2.9. Luminosity Detector

The luminosity detector is positioned between 10.5 m and 12.5 m downstream of the IP to measure the tracks of elastically scattered antiprotons which will travel to the forward region with small scattering angles in the range of 3 mrad to 8 mrad. The tracks can be reconstructed by extracting the time-integrated luminosity from the data. The time-integrated luminosity can be calculated by integrating the instantaneous luminosity \mathcal{L} over a period of time dt as $\mathcal{L} = \int \mathcal{L} dt$. The instantaneous luminosity \mathcal{L} equals to $\mathcal{L} = \Phi \rho_T d$ where d is the thickness, and ρ is the density of target. Φ is called the accelerator beam flux. The elastically scattered antiprotons are measured using a detector layout based on a Roman pot system at 11 m distance to the IP. From the elastic scattering process, the total cross-section can be calculated using the optical theorem. The planes consist of silicon pixels $80 \times 80 \mu\text{m}^2$ with four layers of HV-MAPS ($50 \mu\text{m}$ thickness). HV-MAPS are radiation hard and provide a very high spatial resolution with a low material budget[PAN18].

2.2.10. Data Acquisition

The PANDA experiment will have a free-running data acquisition (DAQ) system, i.e. not using a hardware trigger. This will allow subdetectors to use their own self-triggering modes and to record as much data required to detect complex and diverse physical phenomena. The DAQ system is designed to be sensitive to physics phenomena. The most crucial issue of working with different subdetectors is to have one central clock to provide a common synchronization signal. This will allow to group bunches of hits from the separate systems as one event within a certain time slot. This is only possible by synchronizing the readout systems by using the same clock source which is provided by the synchronization protocol SODANET [PAN20b]. In the following section the architecture of the DAQ system with the protocols for the PANDA readout system is explained.

The PANDA readout system

The highest expected data rate is $2 \cdot 10^7$ events/s for the final PANDA detector phase-2 that will lead to 200 GB/s data rate without any selection criteria. For the high luminosity of PANDA ($\mathcal{L} = 2 \cdot 10^{32} \text{cm}^{-2} \text{s}^{-1}$), the total amount of data is around 114 GB/s. The contribution from the subdetectors is shown in Figure 2.9.

MVD	STT	Barrel DIRC	EDD	BTOF	Target EMC	Fw Tracker	Lum. Det
5 GB/s	20 GB/s	25 GB/s	11 GB/s	7 GB/s	32 GB/s	10 GB/s	4 GB/s

Figure 2.9.: Data rates of subdetectors [PAN20b].

For phase-1, all subdetectors except for Dipole ToF, EDD, and FRICH will be constructed. Luminosity will be gradually increased from $10^{30} \text{cm}^{-2} \text{s}^{-1}$ up to $2 \times 10^{31} \text{cm}^{-2} \text{s}^{-1}$

2. PANDA at FAIR

[PANDA21]. The lower amount of the luminosity will lead to the reduction of data rate 10 orders of magnitude compared to the final design. Since the final data rate is high, the useful data has to be selected before being stored in the PANDA Compute nodes (CN).

The different planned modes of the PANDA DAQ system are:

- Phase-2 production mode will run the whole PANDA detector with all subdetectors loaded.
- Only one or a few PANDA subdetectors are fully loaded.
- Only one or a few PANDA subdetectors are partly loaded.
- Only parts of one subsystem run in stand-alone mode.

Each mode explained above should allow for enabling/disabling data processing if some of the components are not in use or not implemented at a certain period of time such as tracking when the magnet is off. Besides, debugging should be possible for any subsystem while the rest of the systems are running.

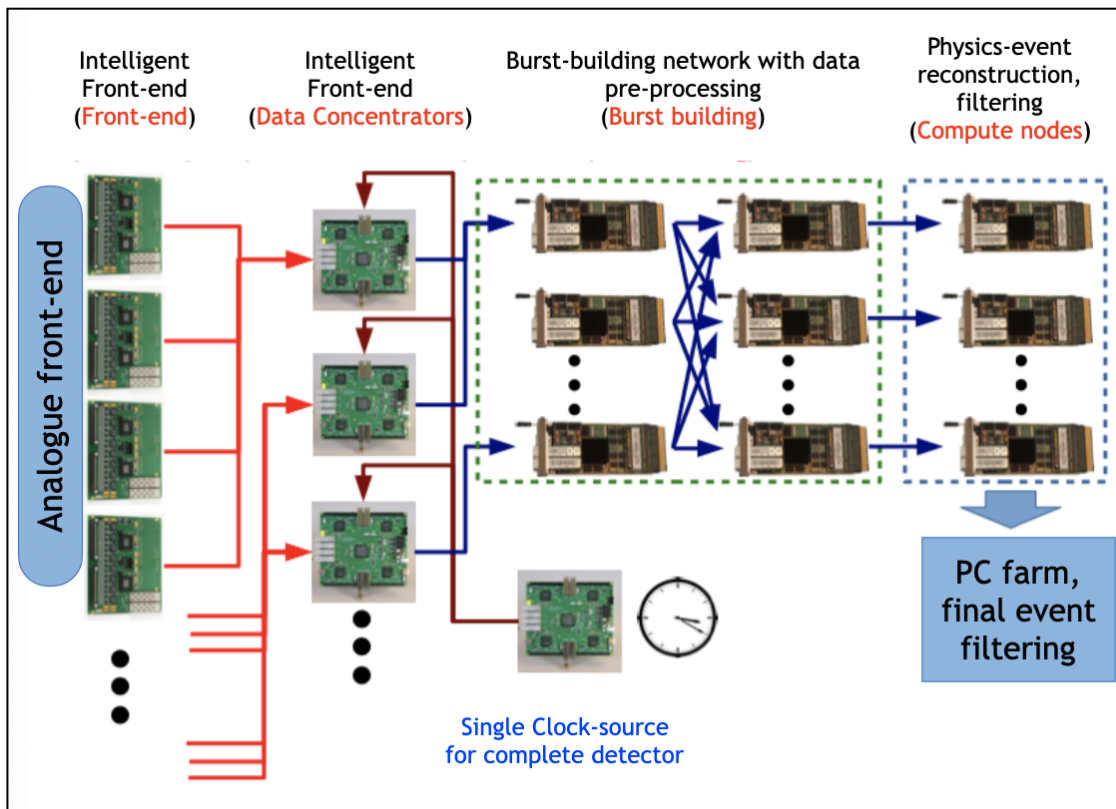


Figure 2.10.: PANDA readout system leading from analogue front-ends to a PC farm for final event filtering [PAN20b].

The system architecture of the PANDA readout system is shown in Figure 2.10 starting from the analog signals of the sensors. The elements of the DAQ system are shown with the specifically designed modules for each step. Analog signals are digitized by the FPGAs of the subsystems dedicated Front-end boards (FEBs). The digitized data is sent to data concentrators which receive the synchronization signal from a reference clock source. The data concentrators assign timing information of the input data and stream it to the Burst Building Network (BBN). The blue arrows in Figure 2.10 represent the re-orientation of the input data by time which is coming from the same or from different subdetectors. For the reconstruction of an event, event filtering etc. the time ordered data sent to the compute nodes. At a final point, data reaches to a PC farm for final event filtering. The following sections explain the DAQ system for phase-1 since the phase-2 scenario is still unclear.

The data concentrator (DC)

The DC is connected to the FEBs of every subdetector. It provides a reference time stamp from a single clock source.

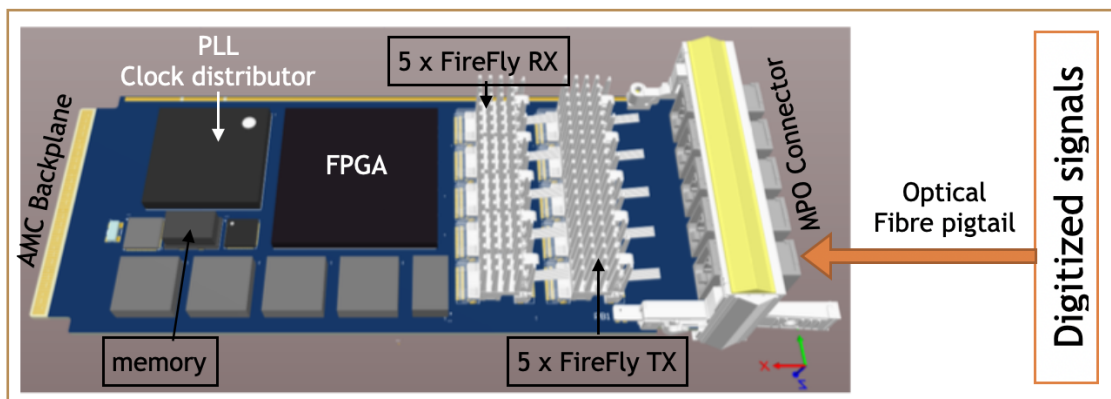


Figure 2.11.: The preliminary design of the data concentrator with labels [PAN20b].

In Figure 2.11, the preliminary design of the data concentrator and its components are shown. The data concentrators consist of an on-board Kintex Ultrascale FPGA to buffer the data within a certain period of time. The FPGA is connected to the AMC⁸ bus via a LVDS connection for slow control (up to 2 GB/s). The AMCs are connected to a MicroTCA crate that provides 12 V to every data concentrator. This voltage is distributed via DC-DC converters to the components on the module, such as FPGAs.

In the preliminary layout the data concentrator is equipped with a 12-channel simplex FireFly receiver and 12-channel simplex FireFly transmitter from Samtec [sam21]. This combination provides to achieve 12 duplex channels. The digitized signals are transmitted via fibre optic cables, and the pigtail of the fibre is connected to the 12-channel

⁸Advanced Mezzanine Card

2. PANDA at FAIR

FireFly simplex transmitter via the MPO-12. The data is buffered and processed via a Kintex Ultrascale FPGA. The clock information in the data concentrator is provided via a clock distributor with dual-PLL jitter cleaner. In order to group data within a certain time interval, the synchronization signal from a single clock source is used in the data concentrator. Meanwhile, the created data bursts are grouped via the Super Burst number (SB number) and sent to a BBN. The details of the protocol and the generation of the number will be explained in the upcoming sections.

The burst building network (BBN)

The BBN routes the incoming data to different compute nodes according to the SB number. For phase-1, 30 optical links (see Figure 2.12) are reserved to transmit the data from DC to BBN. In Figure 2.12, the scheme of the readout system of PANDA is starting from the data concentrator. The number of data concentrators for the corresponding subsystem was determined. Since the thesis is about the readout system of the EDD, some details are mentioned. In total, 8 data concentrators are assigned to the EDD which will send the data to the BBN, CN, and HPC (high performance computing nodes). During phase-1, the EDD will be equipped with its existing DAQ system which is developed by PETsys [pet20] for collecting data. It needs the reference clock signal and synchronization from the PANDA system. The clock and synchronization signal will be distributed through an optical fiber. Moreover, the same protocol will determine the format of the collected data which will be sent to the DAQ. In order to make the existing readout compatible with the PANDA readout system, there are two possible solutions.

The first approach is to design a custom adaptor board in between the PETsys DAQ and PANDA DAQ. This adaptor board should be designed in a way that

- it can receive SODANET clock and synchronization commands.
- the received signals are translated to be recognized by PETsys DAQ system. This might be done by a combination of hardware and software changes.
- the data should be sent to the common PC clusters after reformatting according to SODANET format.

The second possibility is more optimistic in a way that no major change is required, but only some small modifications. This can be achieved if the readout is able to receive all control signals via optical fiber, and to use the PANDA data concentrator to perform all tasks listed above. For the other subdetectors in Figure 2.12, they all have the assigned data concentrators that will pre-process the burst before sending it to CN. The BBN can be implemented to the hardware of the data concentrator as a virtual network of an FPGA which is also shown in Figure 2.12.

The compute node

The CNs are designed with an ATCA architecture which sends the data to PC farms for the final event selection in HPC clusters. The FPGA based CNs are designed with a

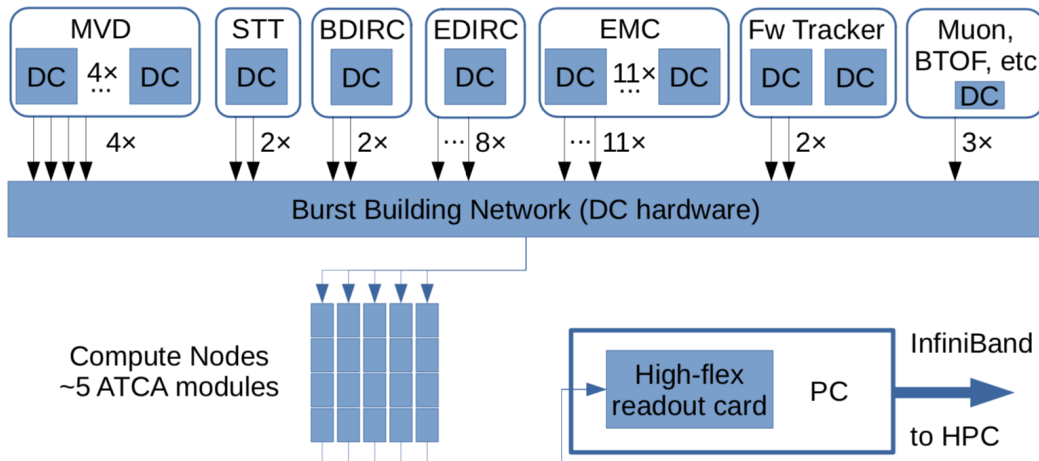


Figure 2.12.: The scheme of the readout system starting from the data concentrator level of the subdetector [PAN20b].

ATCA⁹ architecture. They are capable of handling a multi-Gbit/s bandwidth for high-level algorithms such as event pre-selection, tracking, etc. the level of event filtering. In the compute nodes, the data from different data concentrators are reassembled according to the SB number. Since the DC level may differ between the subdetectors, the latency may occur in the CN which leads to wait till the all packets are arrived. After one data packet is completed, it is processed in the required numbers of CNs depending on the data complexity.

The HPC interface

For the final event reconstruction and filtering process, the data is sent to a high performance computing (HPC) cluster that is based on FPGA compute nodes. It utilizes High-Flex readout cards to receive the data from the detectors back-end. Utilizing InfiniBand [C⁺17] interfaces the data can be sent to a GPUs cluster. To perform the online data reconstruction, the direct communication between the FPGA to GPU can be established by a High-Flex readout card. It is a faster approach compared to the CPU based one. It is planned to use a local CPU/GPU based technique for standalone systems. For the PANDA experiment, the InfiniBand will be used for Event Building Network.

SODANET protocol

SODANET is based on the *burst* structure which is directly related to the momentum of antiprotons. The time between the beam on the target and the time gap (400 ns) before the upcoming beam-on period determines the burst length which is in a range of 1.4 μ s

⁹Advanced Telecommunications Computing Architecture

2. PANDA at FAIR

to $2\ \mu\text{s}$. Data in the DCs are merged with each of the 16 bursts and the gaps that create super bursts. The reason of choosing 16 bursts is to group the outgoing packages with an optimal size so that one FPGA can buffer few SBs. This number can be optimized depending on the final hardware. At each merge, the specific SODANET command **SB-start** ('start to super-burst') creates a number of the starting the super burst period. This periodic behaviour sets all timing circuits at the FEE side to zero since they share the same clock. The order of the created number of super burst is checked by the SODANET. If it is not ordered, the situation is reported to the slow-control system to report the error.

The sketch in Figure 2.13 shows the SODANET source with slow control, HUB, DC, and FEE. When the command 'start to super-burst' is sent, the time in every FEE is set to zero. Each time-stamp requires a correction with the T_d value of the FEE. After the time correction, the SB-number is created and then sent to data concentrator. The data concentrator assigns the hit to the corresponding SB-number and send the burst to the BBN. The output data format of the SODANET consists of super-burst number, system ID (EDD, Barrel DIRC etc.), packet number within super burst data, and a flag for the last data packet.

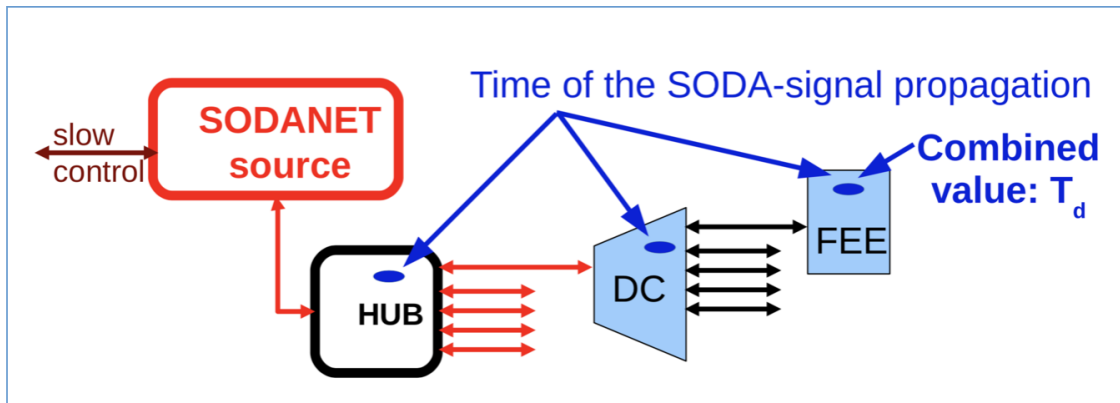


Figure 2.13.: The SODANET based synchronization system of the PANDA readout [PAN20b].

2.2.11. Physics Program

The goal of the PANDA physics program is to explore the strong force which is one of the four fundamental forces. The quantum electrodynamics (QED) is a well-understood theory which allows very precise computations by using perturbation series since the $\alpha_{QED} \approx 1/137$ is small. For quantum chromo dynamics (QCD), the situation is different, because α_s is large at lower energy regions, therefore the perturbative corrections do not work. For high energies, the strong coupling α_s becomes weak and the perturbation theories can be applied which is similar to QED. Whenever the distances among quarks becomes comparable to the size of the nucleon, α_s gets larger. That leads to strong forces

between the quarks become very strong and the quarks cannot be further separated. This is the non-perturbative region of QCD which is the research topic such as quark confinement and hadron masses for PANDA.

The PANDA detector with the subsystems explained will be planned to have a systematic approach for addressing four main physics problems by providing high statistics in a clean environment. These problems are (1) hadrons in nuclei, (2) strangeness physics, (3) nucleon structure, and (4) charm and exotics [PANDA09c]. Figure 2.14 shows the states that PANDA can reach depending on the antiproton momentum. The lower horizontal axis shows the mass of hadrons where the upper axis shows the antiproton momentum range of HESR.

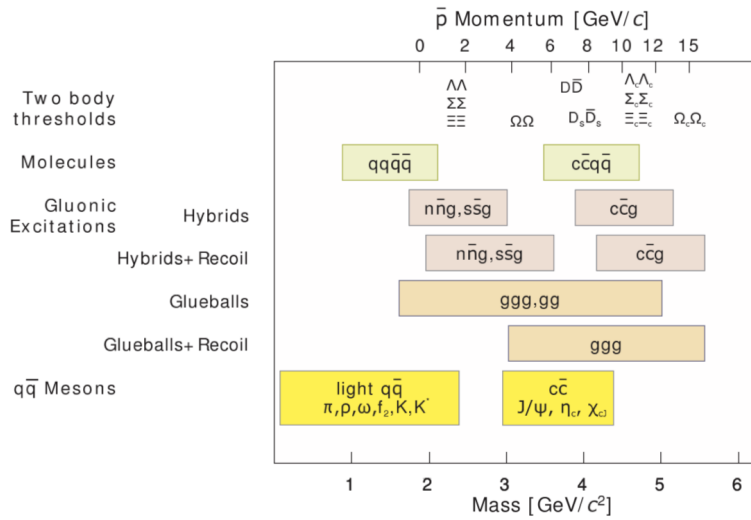


Figure 2.14.: The mass of generated hadronic states as a function of antiproton momentum provided by the PANDA experiment [PANDA09b].

The quark confinement refers to baryon structures with a color confinement and also a comparable weak interaction of quarks in mesons. The area between the perturbative and non-perturbative regime corresponds to the energy regime of $(\bar{c}c)$ meson which is one of the researched topics in PANDA. When the charmonium meson $(\bar{c}c)$ decays to one charm and one light quark state, it is called an open charm state that is also known as D states. Below the open charm threshold (see Figure 2.15), theory shows a good agreement with experiments in the explored region. Some of the experiments in BaBar, CLEO and Belle found some of the states above the threshold value; however, the results do not perfectly fit with the theoretical expectations. This requires a fine scan to measure the parameters with a high accuracy. Due to that reason, the PANDA experiment with the high luminosity mode is planned to provide the required setup to collect several thousand of $\bar{c}c$ states per day.

The other research topic is gluonic excitation which covers the glueballs (only gluons) and hybrids which includes valence quark and antiquark with excited gluon(s). The

2. PANDA at FAIR

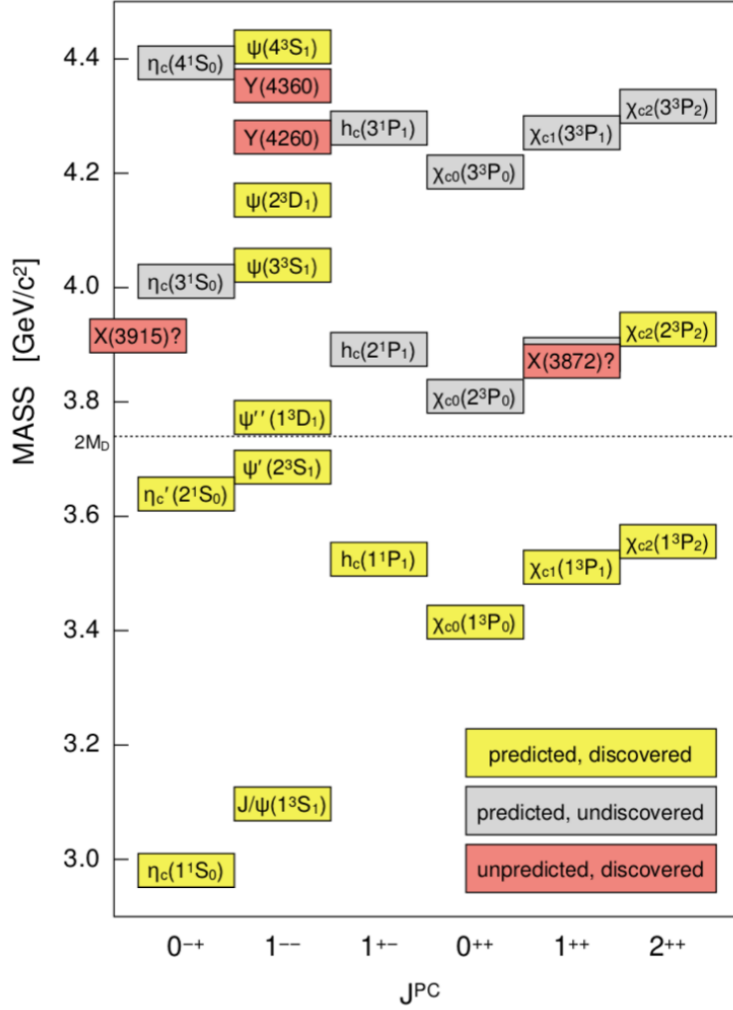


Figure 2.15.: The graph shows the charmonium spectrum with predicted-discovered, predicted-undiscovered and unpredicted-discovered states [BESIII13].

gluonic hadrons have the exotic quantum numbers $J^{PC} = 0^{--}$ and $J^{PC} = 2^{+-}$. The PANDA detector setup with $\bar{p}p$ annihilation has a center-of-mass energy in the range between $2.2 \text{ GeV}/c^2$ and $5.5 \text{ GeV}/c^2$ which allows studying the gluonic hadrons. Similar to the charmonium situation, it will be possible to create many exotic particles for the high luminosity mode which is a great advantage of the PANDA detector over other detectors worldwide.

In addition to the topics mentioned above, nucleon structure and a gamma-ray spectroscopy of hypernuclei can be investigated in PANDA for which the details can be found in [PANDA09c].

3. Particle Identification and Cherenkov Detectors

Particle IDentification (PID) and the DIRC detectors in PANDA were briefly discussed in the previous sections. The motivation for this section is to explain the techniques for particle identification depending on the detector and particle type.

3.1. Particle Identification (PID)

PID techniques utilize particle properties such as charge, or specific physical interaction mechanisms with the detector. Depending on the particle type, specialized detectors are used. The PANDA experiment is designed to study the field of hadron spectroscopy by using annihilation of proton and antiprotons. In order to identify particles which PANDA is looking for (such as i.e. hyperons, charm, etc.), all final states have to be precisely identified by using a 4-vector notation. This requires the calculation of momentum and energy of particles by using the information obtained from the subdetectors.

The topology of PID is shown in Figure 3.1. The dashed lines indicates missing signals in contrast to the continues lines. Charged particles ionize materials of tracking detectors which discriminates them from neutral particles. The electric charge of particles can be distinguished negatively or positively by tracking these paths in a magnetic field. The momentum of particles is found by measuring their curvature. Figure 3.1 shows how photons, e^+ and e^- deposit the energy in the electromagnetic calorimeter (EMC) via bremsstrahlung and pair production. Highly energetic particles start emitting energy when entering a dense material. Electrons and positrons lose their energy in a factor of $1/e$ while traveling in the material within what is called a radiation length. The electromagnetic shower continues till the multiple new particles get stuck with little amount of energy. Hadrons are stopped inside the hadronic calorimeters (HCAL) by draining their energy via hadronic showers. Since no HCAL is used in PANDA, a combination of two DIRC detectors is planned for the purpose of PID. The identification of μ^\pm will be provided by the muon detectors. Only neutrinos are invisible particles for the experiments due to their very weak interaction. They can be detected by looking at missing momentum (momentum conservation).

3.1.1. Energy Loss

Heavy charged particles ($m_{\mu, \pi, \dots} > m_e$) lose their energies due to ionization of the surrounding detector matter which can be converted into electronic signals. Signal infor-

3. Particle Identification and Cherenkov Detectors

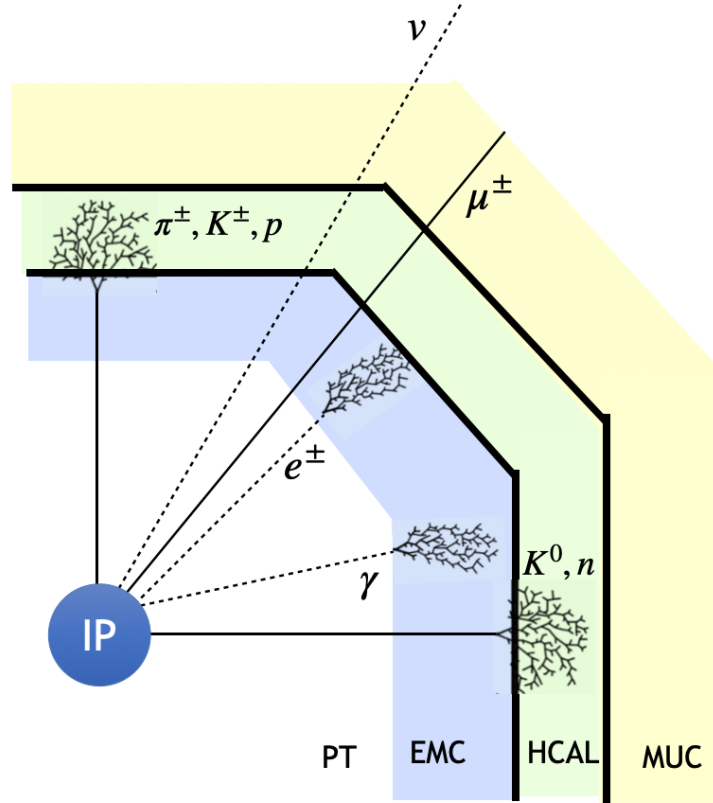


Figure 3.1.: The location of the particle identification is shown in the scheme depending on the detector type which are Particle Tracking (PT), Electromagnetic Calorimeter (EMC), Hadronic Calorimeter (HCAL) and MUon Chambers (MUC).

mation from tracking detectors is necessary to identify hadrons together with the signal from HCAL. In other words, the *stopping power* of the detector is well defined depending on the particle type, energy and the material of the detector. The stopping power can be calculated with the Bethe-Bloch formula:

$$-\frac{dE}{dx} = 2\pi N_a r_e^2 m_e c^2 \rho \frac{Z z^2}{A \beta^2} \left[\ln \left(\frac{2m_e \gamma^2 c^2 W_{max}}{I^2} \right) - 2\beta^2 - \delta(\beta\lambda) \right] \quad (3.1)$$

with $2\pi N_a r_e^2 m_e c^2 = 0.307 \text{ mol}^{-1} \cdot \text{cm}^2$.

3.1. Particle Identification (PID)

r_e : electron radius = 2.817×10^{-13} cm
 N_a : Avogadro's number = 6.022×10^{23} mol $^{-1}$
 Z : atomic number of absorbing material
 ρ : density of absorbing material
 $\beta = v/c$
 c : speed of light

m_e : electron mass
 I : mean excitation potential
 A : atomic weight of absorbing material
 z : charge of incident particle (i.p.)
 $\gamma = 1/\sqrt{1 - \beta^2}$
 λ : wavelength

W_{max} is the maximum energy transfer to an electron from a particle with mass M .

$$W_{max} = \frac{2m_e c^2 \beta^2 \gamma^2}{1 + \gamma \frac{m_e}{M} + \left(\frac{m_e}{M}\right)^2} \quad (3.2)$$

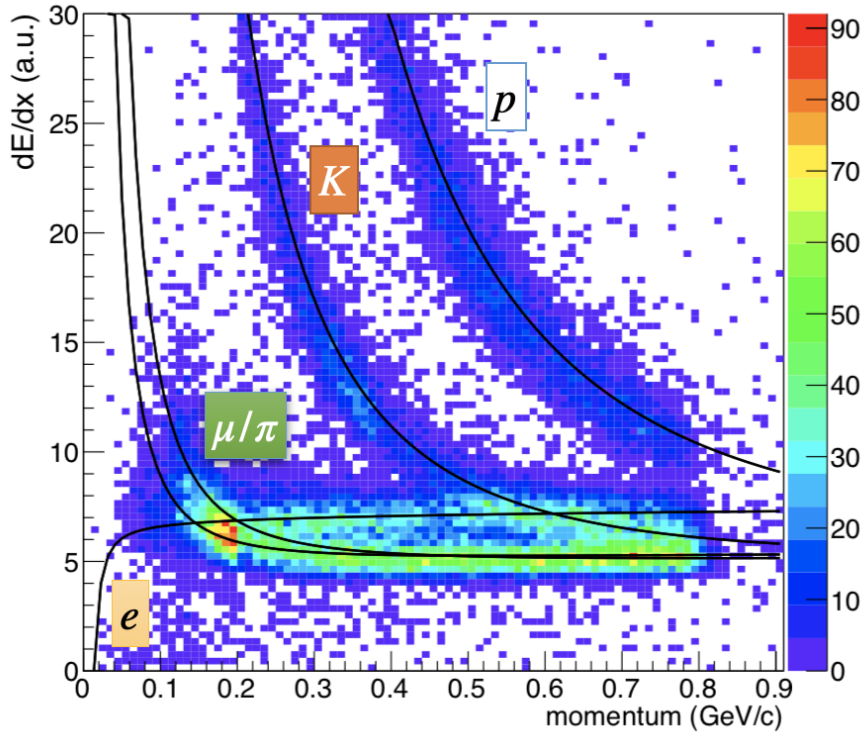


Figure 3.2.: Truncated mean values of dE/dx as a function of reconstructed momentum for electrons, muons, pions, kaons and protons in STT of the PANDA detector [PANDA13].

The STT of the PANDA detector will be filled a gas mixture of Argon and CO_2 . The energy deposition in the STT in arbitrary units depending on the momentum of a particle is plotted in Figure 3.2 for different particles. The band of muons and pions overlap due to the discrimination method used (for further information see [PANDA13]).

3. Particle Identification and Cherenkov Detectors

3.1.2. Time of Flight

In order to calculate a mass of the charged particles, the Time-of-Flight (ToF) measurement can be applied assuming that the momentum is measured from tracking in the magnetic field. Two detectors (scintillators) are placed apart in a well defined distance L . One particle with m mass and momentum $p = |\vec{p}|$ travels the distance L in time t :

$$t = \frac{L}{v} \quad (3.3)$$

where $v = \beta c$ and β is:

$$\beta = \frac{p}{\sqrt{(mc)^2 + p^2}}. \quad (3.4)$$

$$t = \frac{L}{c} \frac{\sqrt{p^2 + (mc)^2}}{p} \quad (3.5)$$

where the velocity of light is c in vacuum. The mass is used to identify the particle type. This technique is very efficient to calculate the time difference Δt between two particles which have the same charge and momentum but different masses m_1 and m_2 :

$$\Delta t = \frac{L}{c} \left[\sqrt{1 + \left(\frac{m_1 c}{p}\right)^2} - \sqrt{1 + \left(\frac{m_2 c}{p}\right)^2} \right]. \quad (3.6)$$

These two particles are highly relativistic which leads to $\frac{mc}{p} \ll 1$ in the Taylor expansion term:

$$p \sqrt{1 + \left(\frac{mc}{p}\right)^2} = p \left[1 + \frac{(mc)^2}{2p^2} + \left(\frac{mc}{p}\right)^4 + \dots \right]. \quad (3.7)$$

First-order expansion leads to a simplified formula 3.6 of:

$$\Delta t = \frac{Lc}{2p^2} (m_1^2 - m_2^2). \quad (3.8)$$

In order to separate the particles via ToF detectors, there are some limitations to be taken into account. The time difference (Δt) cannot be measured when it is smaller than the resolution of the detector readout systems. This may occur when $p \rightarrow \infty \Delta t \rightarrow 0$.

In Figure 3.3, the separation of π/K as a function of the particle momentum and time resolution of the ToF detectors is shown for 2 m distance between two ToF stations. As indicated the separation power decreases with the increased momentum.

Separation power is defined as follows:

$$n_\sigma = \frac{|\mu_1 - \mu_2|}{\frac{\sigma_1 + \sigma_2}{2}} \quad (3.9)$$

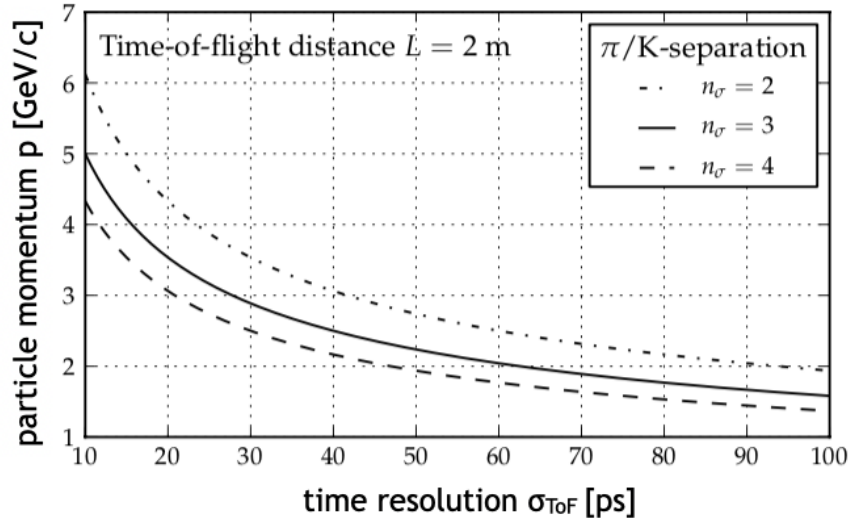


Figure 3.3.: π/K separation power for three different σ values as a function of particle momentum and time resolution of ToF stations [Mer14].

where μ_i is the mean value of the distribution of certain particle types as a function of time difference between the ToF stations and σ_i is the standard deviation. In order to separate the different particle species, this method was applied for the test beam experiments which will be explained in the test beam analysis chapter.

3.1.3. Cherenkov Radiation

The Cherenkov effect was experimentally discovered by Pawel A. Cherenkov in 1934 [Che34] by observing a weak emission of visible light under γ and β irradiation of uranium salt. Since this effect was not known at that time, his supervisor Vavilov and he suggested a preliminary theory about the reason of the radiation. They proposed that the γ radiation produces Compton electrons which would yield a type of bremsstrahlung radiation. However, the reason of the radiation was not bremsstrahlung which was explained by M. Frank and I.Y. Tamm a few years later [FT37]. It was the charged particles with a speed exceeding the phase velocity light speed that emit Cherenkov photons while traversing a transparent medium. As a result of the discovery, Cherenkov was honored with the Nobel Prize in 1958.

The speed of light inside a material is calculated via

$$c' = \frac{c}{n} \quad (3.10)$$

where n is the refractive index of the material bigger than zero in most cases. This shows that the speed of light inside the material is always smaller than the speed in vacuum.

3. Particle Identification and Cherenkov Detectors

When a fast charged particle traverses a radiator, the speed of the particle may be bigger than the speed of the light in the material $v_{par} > c'$. It polarizes the atoms around the moving direction and leads to an asymmetric dipole field as can be seen in Figure 3.4. As a result of this effect, Cherenkov photons are emitted in a cone around the track of a charged particle. This event is similar to Mach Shock waves (sonic boom). The angle between the emitted photons and particle track is called Cherenkov angle.

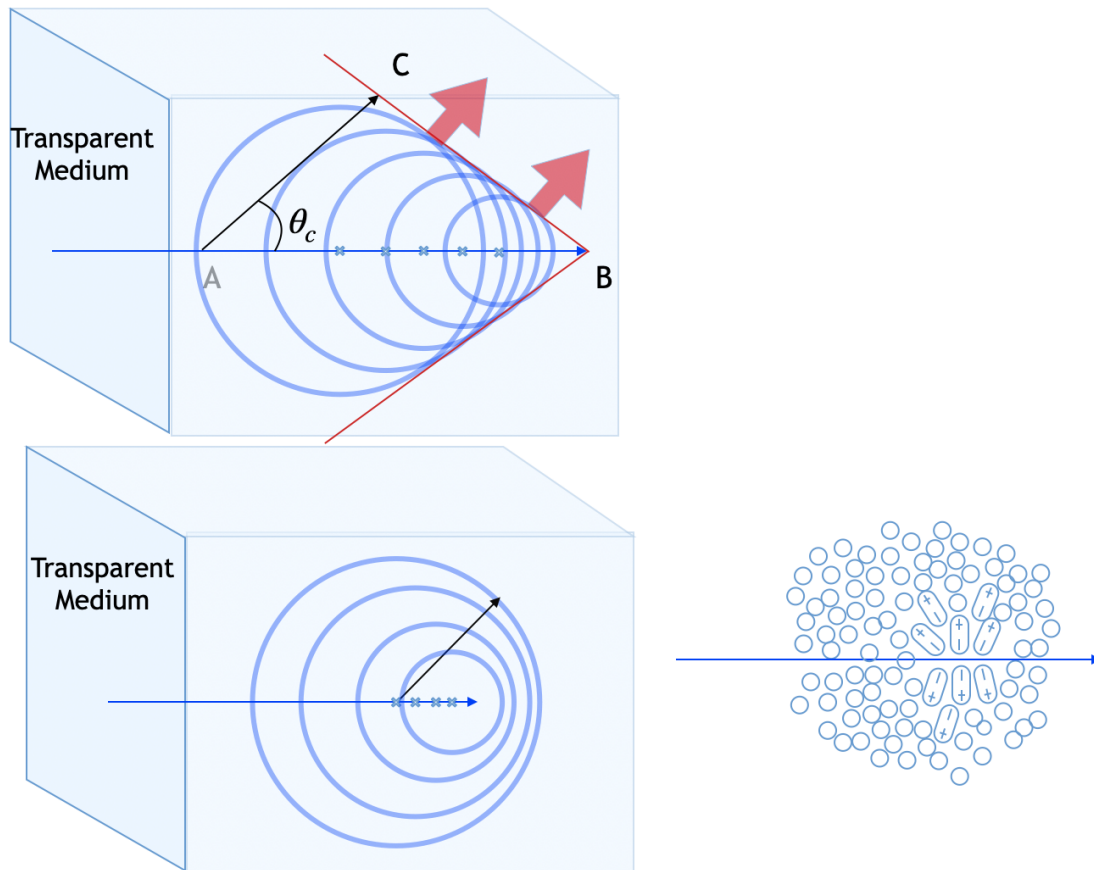


Figure 3.4.: A positively charged particle traverses a transparent medium, it polarizes the atoms nearby. The upper sketch shows the wavefronts when a particle is moving faster than local speed of light ($\beta > 1/n(\lambda)$) in the medium. The bottom left sketch shows when the speed of charged particle is not higher than local speed of light ($\beta < 1/n(\lambda)$). The polarization of this effect is visualized at bottom right.

Some unique properties of Cherenkov radiation can be summarized as:

1. The radiation is created by charged particles.
2. The emission of the light is asymmetric. The asymmetrical polarization of particles

inside the medium in front and at the rear of the charged particle direction results in a varying electric dipole momentum.

3. The intensity of the radiation is related to the particle velocity and refractive index of the material.
4. The Cherenkov radiation is emitted under specific angles.

The Cherenkov angle between the emitted photons and the particle track can be calculated

$$\cos \theta_c = \frac{AC}{AB} = \frac{ct/n(\lambda)}{\beta ct} = \frac{1}{n(\lambda)\beta}. \quad (3.11)$$

Then θ_c becomes

$$\theta_c = \arccos \left(\frac{1}{n(\lambda)\beta} \right) = \arccos \frac{\sqrt{m_0^2 c^2 + p^2}}{n(\lambda)p}. \quad (3.12)$$

where m_0 is mass of the particle. The mass of the charged particle is in the equation which shows the possibility of using Cherenkov radiation for particle identification. When the charged particle traverses the radiator and travels the distance dx , the number of emitted photons can be calculated according to the Frank-Tamm formula [FT37]:

$$\frac{d^2 N_{ph}}{dE dx} = \frac{\alpha z^2}{\hbar c} \left(1 - \frac{1}{(\beta n)^2} \right) = \frac{\alpha z^2}{\hbar c} \sin^2(\theta_c) \quad (3.13)$$

where $\alpha \approx 1/137$ is the fine structure constant and z is charge. If photons are emitted in an infinitesimal wavelength region $d\lambda$, the number of photons can be calculated by integration

$$N_{pho} = 2\pi\alpha z^2 \int_{\lambda_1}^{\lambda_2} \frac{\sin^2 \theta_c}{\lambda^2} d\lambda \int_0^L dx. \quad (3.14)$$

The refractive index $n = n(\lambda)$ is depending on the wavelength, which means that the Cherenkov angle of the pions, kaons and protons is subject of dispersion. In Figure 3.5, Cherenkov angles are plotted as a function of the momentum for the wavelength range of visible spectrum $300 \text{ nm} \leq \lambda \leq 700 \text{ nm}$. The red lines represent pions, the blue ones are kaons and the green photons are protons. The dispersion effect can be reduced by selecting a specific wavelength which can be done by using a filter in the experiment setup.

3.2. Cherenkov detectors

All Cherenkov detectors are based on the same working principles. They utilize both a transparent medium called radiator and different optics for focusing or mirroring Cherenkov light to the sensors. Depending on the studied momentum range in the experimental

3. Particle Identification and Cherenkov Detectors

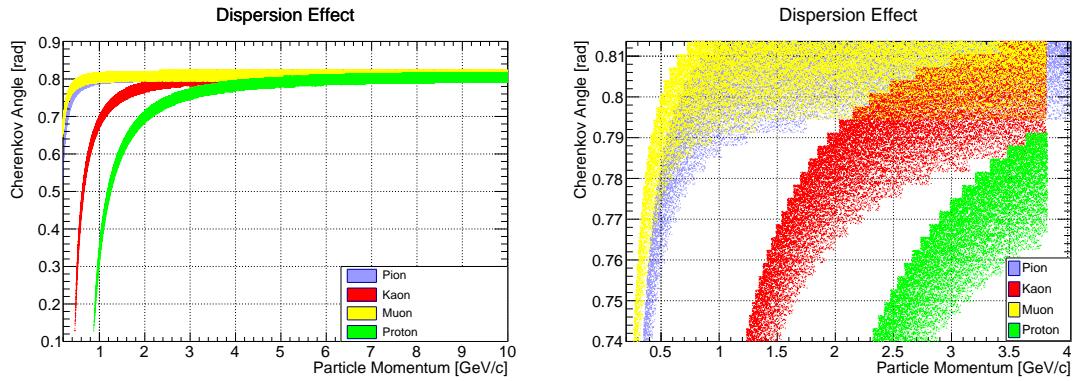


Figure 3.5.: Left: Dispersion of Cherenkov angle depending on a wavelength in the visible spectrum which is $300 \text{ nm} \leq \lambda \leq 700 \text{ nm}$. Right: Zoomed version.

setup, available space for the detector, desired separation power, and the radiator material with proper refractive index are chosen. The following sections will discuss the different Cherenkov detectors used in different experiments.

The Ring Imaging Cherenkov Detectors (RICH) [Va'14] detectors were developed to detect hadrons in 1980s for different experiments such as an E605 experiment at FNAL [G⁺83], Omega RICH [S⁺94] etc. Gas in combination with an aerogel layers is chosen as a radiator for RICH detectors. The LHCb experiment uses a combination of two RICH detectors for the identification of charged particles in the momentum range between 2 GeV/c and 100 GeV/c. The radiator choice for RICH2 is CF_4 gas while RICH1 utilizes 16 tiles of silica aerogel with a 50 mm thickness inside C_4F_{10} gas. More details of about LHCb RICH detectors can be found [Group13]. The RICH detector with dual radiator was used in HERMES experiment at DESY to identify protons, pions and kaons in the momentum range from 2 GeV/c to 15 GeV/c [A⁺02]. The radiator choice was a combination of C_4F_{10} and aerogel tiles. The details of the HERMES experiment can be found in [HERMES98]. A forward RICH detector with an aerogel radiator was designed for the PANDA experiment to detect the charged particles with higher momenta in the polar angle range $|\theta_x| < 10^\circ$ and $|\theta_y| < 5^\circ$ in the FS. The shape of the Cherenkov radiation in RICH can be in an elliptic or in a circular shape. The emitted Cherenkov light can be focused to the sensors by using different techniques shown in Figure 3.6. The first technique (a) represents the Cherenkov radiation using a thick radiator with a refractive index n . The Cherenkov cone on the imaging plane has a reflection with a large width. The second (b) and third (c) scenarios show two materials for different layers with a refractive index n_1 and n_2 . For the scenario (b) $n_1 < n_2$ the resulting Cherenkov ring is smaller than scenario (c). The scenario (d) and (e) show the Cherenkov ring more than two different layers of the radiator with different refractive indexes. The scenario (d) is called an index matching technique which provides Cherenkov ring with smallest thickness.

The DIRC detectors are a modification of the RICH detectors by trapping Cherenkov photons in the radiator. Figure 3.7 illustrates four different focusing techniques for Cherenkov photons. The emitted Cherenkov photons trapped inside the radiator are internally

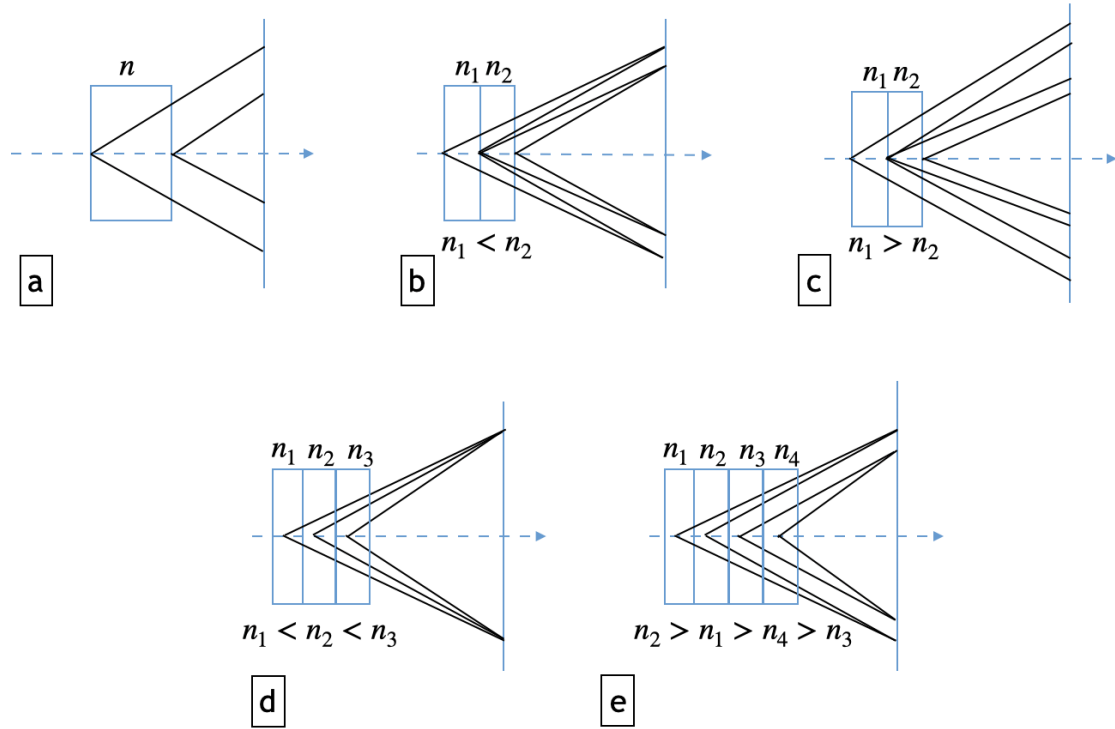


Figure 3.6.: (a) Thick radiator with a smearing effect, (b) two different aerogel layers with refractive indexes $n_1 < n_2$, (c) two different aerogel layers with the refractive indexes $n_1 > n_2$ causes a larger Cherenkov ring, (d) three different layers with refractive indexes $n_1 < n_2 < n_3$ creates a very precise Cherenkov ring image by index matching, (e) with refractive indexes $n_2 > n_1 > n_4 > n_3$ similar behavior as in scenario (b).

reflected by conserving the angle information in a zig-zag pattern determined by the readout system. Some Cherenkov photons leave the radiator if their angle is less than the critical angle needed for internal reflection. The critical angle depends on the refractive index of the radiator (n_1) and its surrounding environment (n_2). It is calculated as:

$$\epsilon_c = \arcsin\left(\frac{n_2}{n_1}\right). \quad (3.15)$$

In Figure 3.7, left upper and right upper sketches are two different techniques currently used for the DIRC detectors of the PANDA experiment. Proximity focusing and 'no imaging' techniques can also be seen in the lower sketches in Figure 3.7. These two techniques are not focusing photons which lead to smearing effects. When the photons are focused on a surface of highly granulated pixels, angle to position information can be calculated in a very certain way. The RICH techniques provide an excellent separation of particles for a wide momentum range. The techniques of a,b,c, and e in Figure 3.6

3. Particle Identification and Cherenkov Detectors

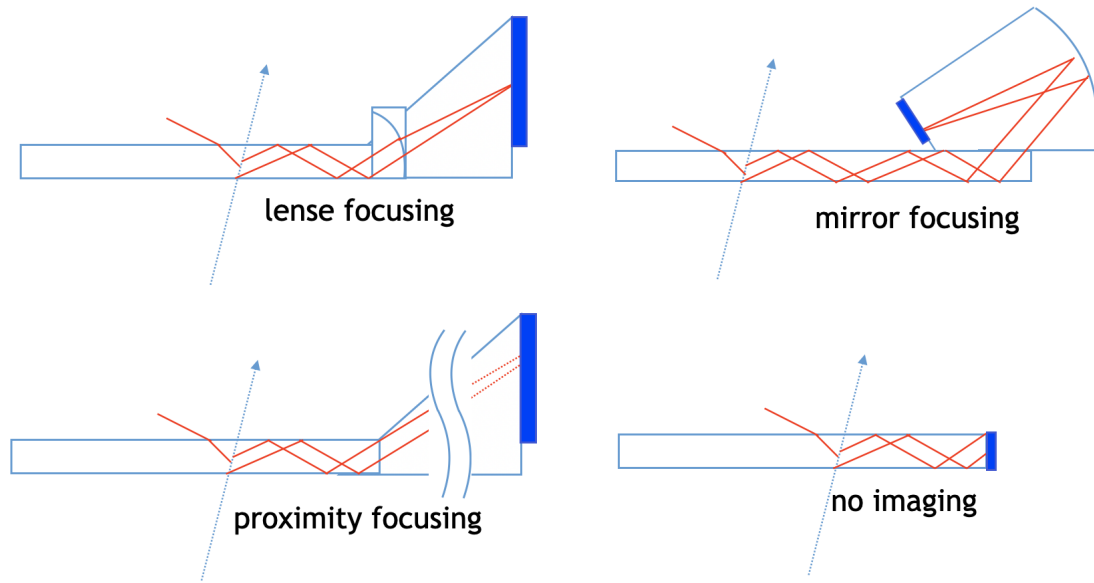


Figure 3.7.: The upper left sketch illustrates the lens focusing of Cherenkov photons created by charged particle by conserving the angle information during internal reflections. The upper right sketch shows mirror focusing of Cherenkov photons. The bottom left sketch shows the proximity focusing. The bottom right sketch shows the detection without any imaging. Here TOP is used to extract the Cherenkov angle.

provide a wide Cherenkov Ring which results in a bad resolution. The best technique is option-d which yields a very precise focusing on the detector surface.

3.3. DIRC Detectors

There are several DIRC detectors in use for particle identification in experiments at different momentum ranges. The history of the DIRC detectors started in the BaBar experiment in the barrel region. The BaBar experiment was built at Stanford Linear Accelerator (SLAC) to make a study on CP violation during B meson production. BaBar was designed to identify hadronic particles in the region of 94% of azimuth angle and 80% of polar angle range. Fused silica was used as a radiator material and 144 bars were used in total with a dimension $17.25(T) \times 35(W) \times 4900(L)$ mm³. When a charged particle traverses the bar, the emitted Cherenkov photons are internally reflected to the readout sensor system. One end of the bar was mirrored to reflect back Cherenkov photons. Cherenkov photons are expected to reach a fused-silica wedge and hit a photosensor without focusing optics. For Cherenkov photon detection, 10,752 PMTs were used in total [A⁺05].

Confirmed performance of BaBar DIRC motivated scientists to adopt the DIRC concept

to other experiments. Several DIRC concepts modifications are to deal with specific needs of different experiments. These techniques are explained in following chapters. There are Focusing DIRC concepts applied for the GLUEX, PANDA DIRCs, SuperB experiment and EIC DIRC, Time-of-propagation (TOP) counter for Belle-II, Time Of Internally Reflected Cherenkov light (TORCH) at LHCb.

3.3.1. Detectors based on focusing concepts

The GLUEX detector and the PANDA Barrel DIRC use focusing techniques. The DIRC detector in GLUEX experiment is further explained in this section since the PANDA Barrel DIRC was already explained in the previous chapter.

The GLUEX experiment is an ongoing experiment at Jefferson Lab (JLAB). The bars are positioned as a single plane in the forward region. The acceptance is $\leq 11^\circ$ in the forward polar angle region which can be covered with four boxes filled with 12 recycled fused silica radiator bars from the BaBar experiment. They are aligned symmetrically around the beam pipe that supplies a common readout system for two boxes. The bars are coupled to the Optical Box (OB) which consists of multiple flat aluminized mirrors immersed in water. The refractive index of water provides a matching between fused silica and the expansion volume to prevent photon losses. It uses Multi-Anode PMT (MaPMT) which can work in the magnetic field [Col15].

The SuperB detector concept is similar to the BaBar detector with some modifications. These modifications were necessary since the planned data sample rate is 50-100 times more higher than in BaBar DIRC [SuperB13]. The SuperB FDIRC detector uses recycled bar boxes and the mechanical structure of the BaBar detector with a new design of photon camera. The optical system consists of cylindrical and flat mirrors which focus Cherenkov photons on PMT planes [Col15].

The EIC DIRC concept is based on PANDA Barrel DIRC but aiming to cover double momentum range. Due to that reason it is called high-performance DIRC (hpDIRC). The optical elements are 3-layer spherical lenses, expansion volumes and MCP-PMTs as photosensors similar in PANDA Barrel DIRC [Kal20].

3.3.2. Imaging Time of Propagation Detector in Belle-II

The imaging TOP (iTOP) detector is another version of DIRC detectors in the barrel region of the Belle-II experiment. It uses a time-based reconstruction method for providing a better PID [RV20]. It consists of fused silica bars as a radiator with a dimension 270 cm (L) \times 45 cm (W) \times 2 cm (T). Similar to other bar-shaped DIRC detectors, a mirror is attached to one end of the bar to reflect back Cherenkov photons to a small expansion prism. The prism is couple to 32 MCP-PMT which has 16-channels [Fas17] with a wavelength filter in between.

3. Particle Identification and Cherenkov Detectors

3.3.3. TORCH at LHCb

TORCH detector at LHCb is designed to provide PID for low momentum of particles from 2 GeV to 10 GeV/c. It uses a fused silica plate and focusing optics to detect trapped Cherenkov photons. The principle is quite similar with the Belle-II TOP detector and the PANDA EDD. Cherenkov photons are detected by highly granulated MCP-PMT with 8×128 pixels [H⁺20].

4. The Disc DIRC Detector

4.1. Working principle of the EDD

In Figure 4.1, one radiator with three focusing elements are visualized. A charged particle is shown as a black arrow while traversing the radiator in three different perspectives. The first drawing in Figure 4.1, α_{FEL} is shown as an angle between the 'active' focusing element and the photon trajectory and ϕ_{rel} is the angle between photon trajectory and primary particle. The isometric view of the setup with a charged particle traversing the radiator can be found in the second drawing. The third drawing represents the side view of the effect. The asymmetric Cherenkov cone with an opening angle θ_c is colored red. Some photons will be internally reflected in the fused silica radiator ($n = n(\lambda)$) if ϕ is:

$$\phi < \arccos(n(\lambda)) \quad (4.1)$$

by following the zig-zag path which is represented in red color. The ϕ is an angle between the photon path and the radiator surface. It is calculated according to formula [Mer14]:

$$\cos \phi = \frac{A \cos \theta_c}{B} \pm \sqrt{\frac{\cos^2 \theta_p - \cos^2 \theta_c}{B} + \left(\frac{A \cos \theta_c}{B}\right)^2}, \quad (4.2)$$

in which A and B given as:

$$A = \sin \theta_p \cos \phi_{rel}, \quad B = \sin^2 \theta_p \cos^2 \phi_{rel} + \cos^2 \theta_p. \quad (4.3)$$

Photons will enter the bar of the focusing element which is shown in black color. The ϕ' angle is determined by the position of the sensor pins where the signal hits:

$$\phi' = mz + b. \quad (4.4)$$

Moreover, the relation between angle ϕ' and ϕ is dependent on α_{FEL} :

$$\tan(\phi') = \frac{\tan \phi}{\cos \alpha_{FEL}}. \quad (4.5)$$

Due to the highly granulated sensor, the Cherenkov angle can be reconstructed according to formula:

$$\theta_c = \arccos\left(\sin \theta_p \cos \phi_{rel} \cos \phi + \cos \theta_p \sin \phi\right) \quad (4.6)$$

which θ_p is the angle of the particle.

4. The Disc DIRC Detector

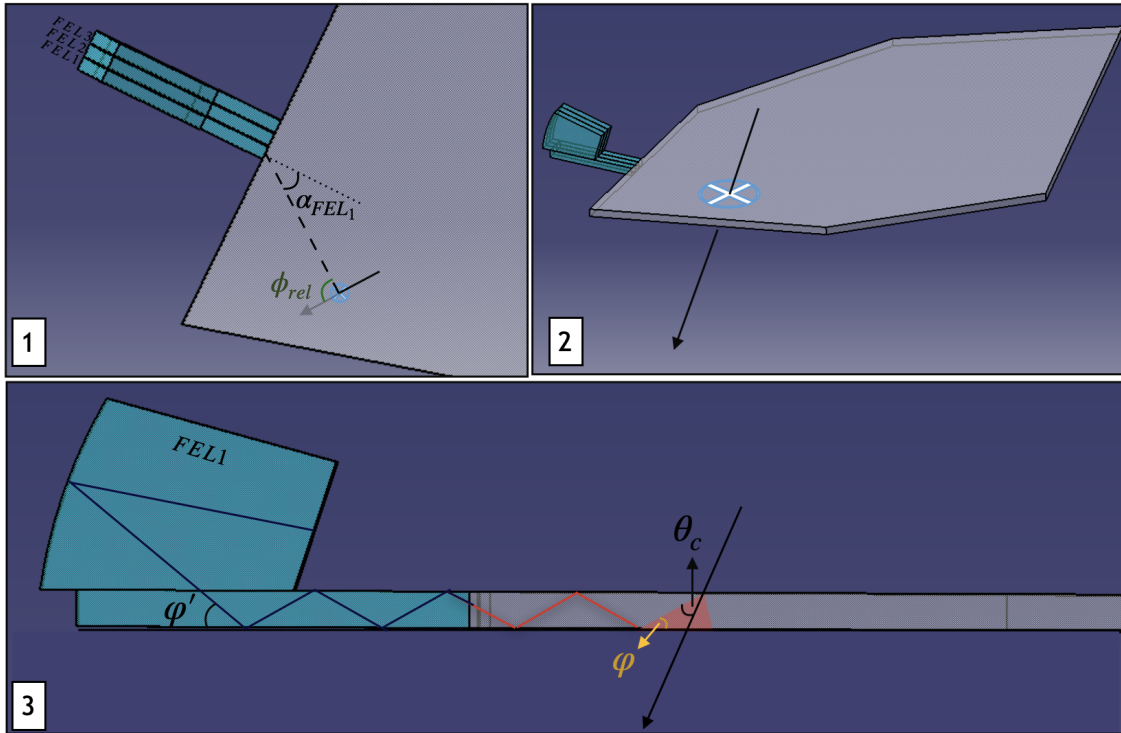


Figure 4.1.: 1: Top view of the radiator with three FELs. The angle between the charged particle and the FEL is α_{FEL} . 2: The isometric view of the radiator with the position of charged particle traversed. 3: The side view of the setup with a Cherenkov cone (red) and the angles.

4.2. The setup of the detector

The PANDA experiment requires particle identification in the target spectrometer (TS), which is going to be performed with a combination of two DIRC detectors in the polar angle range from 5° to 140° . It is planned that the Barrel DIRC will cover the polar angles from 22° to 140° and the geometry of the Endcap Disc DIRC (EDD) provides from 5° to 22° coverage of the polar angle. The EDD is the world's first disc-shaped Cherenkov detector and it requires a combination of different approaches in scientific and engineering fields to fulfill the requirements of the PANDA detector. In this chapter, the design of the detector will be explained by including the current system with additional suggestions to the final design.

The key components of the EDD are four independent symmetrical quadrants, a cross-shaped holding frame between them, focusing optics and an ASIC-based TOFPET2 [pet20] readout system. The exploded CAD view in Figure 4.2 shows the key components which are the mechanical structures and the optical elements with dedicated front-end-electronics (FEE). The radiator and focusing optics are made of accurately polished fused silica. The radiator is divided into four independent symmetrical quadrants which have a thickness

4.2. The setup of the detector

of 2 cm and an outer radius of 1.056 m. These quadrants will be placed inside of a 2 mm thickness radiator frame. The focusing optics will be positioned at the outer rim of the radiator. They have to be covered by a light-tight housing. In order not to disturb internal total reflection, it is utterly essential to make the light-tight housings stable enough to cover without contacting the surfaces. The stabilizing cross-shaped item profile will provide a durable mechanical structure for individual quadrant plates in z -direction. The stabilizing cross (SC) will be fixed on a octagon-shaped mounting plate (MP) with a circular hole in the middle. The MP can be designed as two pieces since the production and carriage of such a big structure are not easy to handle. The two pieces of the mounting plate will be placed on the upstream side of the holding structure. The holding structure is already produced to dock the Electro Magnetic Calorimeter (EMC) on the downstream side. The upstream side of the MP is reserved for the EDD.

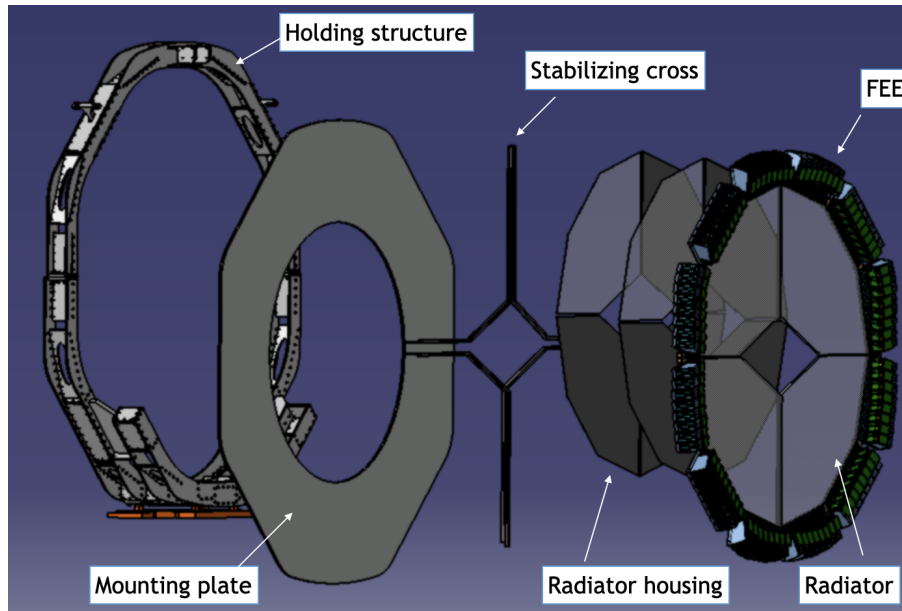


Figure 4.2.: Exploded CAD view of the EDD with the main components.

One EDD quadrant includes 24 readout modules (ROMs). Every ROM encloses three focusing elements (FEL) with a direct connection to the three bar prisms and one sensor with the glass filters. The width of the bars is 16 mm with a 1 mm distance between them, thus, inner side of every ROM is 50 mm width. In total, 96 ROMs will be utilized with one sensor each. Since each sensor delivers 3×100 signal channels, fully equipped EDD will have 28.800 pins of sensor in total.

The principle of the EDD is based on Cherenkov light which is also used in other kind of the Cherenkov detectors. The charged particle traverses the radiator disc with a refractive index $n(\lambda)$ depending on the wavelength of the photons. If $\beta = v/c > 1/n(\lambda)$, Cherenkov photons are emitted in a conical shape with the half opening angle θ_C given

4. The Disc DIRC Detector

as

$$\cos(\theta_c) = \frac{1}{\beta n(\lambda)}. \quad (4.7)$$

In Figure 4.3 from the quadrant back view, the concept is visualized with a green arrow as a charged particle. It traverses the radiator which leads to emission of Cherenkov photons (purple tracks). Due to the gap between the quadrants, photons will be reflected at the side of the radiator. They cannot leave the radiator from the sides and then enter neighboring radiator plate. These side reflections result in a pile-up of photon patterns from direct and indirect hits which can be discriminated by applying a time cut. The pattern of Cherenkov photons starting from the radiator to the filter is shown from the side view of one ROM in Figure 4.3. It is visualized in the zoomed view to show how some Cherenkov photons are always reflected internally through the readout system if $\beta \approx 1$ while the rest of them will leave the radiator. Furthermore, Cherenkov photons reach the FEL by conserving their Cherenkov angle θ_c . They are focused on the filter via the cylindrical mirror of the FEL before entering the photocathode of the MCP-PMT. An ASIC-based readout which digitizes the low intensity of MCP-PMT analog signals is shown in the exploded-view of the CAD drawing in Figure 4.3. After the photon hits the photo-sensor, the accumulated photo-electrons will hit one of the highly granulated segmented anodes of the MCP-PMT. The high granularity of the anodes provides a sufficient position resolution to reconstruct the incoming photon φ' angle. The angle reconstruction will be explained in the following sections. The ASIC-based readout system is attached to the sensor anodes with either 100×3 pins of PHOTONIS [PHO] or 128×6 pins of HAMAMATSU [HAM] with 384 effective ones.

There are two project phases for the PANDA sub-detectors. Many of them will be installed during the first phase, including the Barrel DIRC. The EDD is planned to be installed in the TS in the second phase of PANDA. For the first project phase, a prototype of one quadrant is planned to be installed to provide a test the setup in the experimental area. The fused silica plate was delivered in 2019 and the quality measurements were finished. According to the experience gained from phase-1, appropriate modifications can be applied for final EDD. To reach the fully equipped EDD, the accomplished steps and the further plans of the EDD schedule are outlined:

- As a first step, a rectangular-shaped prototype with three ROMs was tested in CERN beam time in 2018. Convincing results were obtained.
- One radiator plate was integrated into an experiment with cosmic muons in a horizontal direction. This experiment setup is referred to as Giessen Cosmic Station (GCS).
- Measurements with one ROM were started.
- Tests with three available ROMs in light-tight housings are planned.
- After completing tests in a horizontal position, the vertical holding structure will be designed and integrated into the GCS.

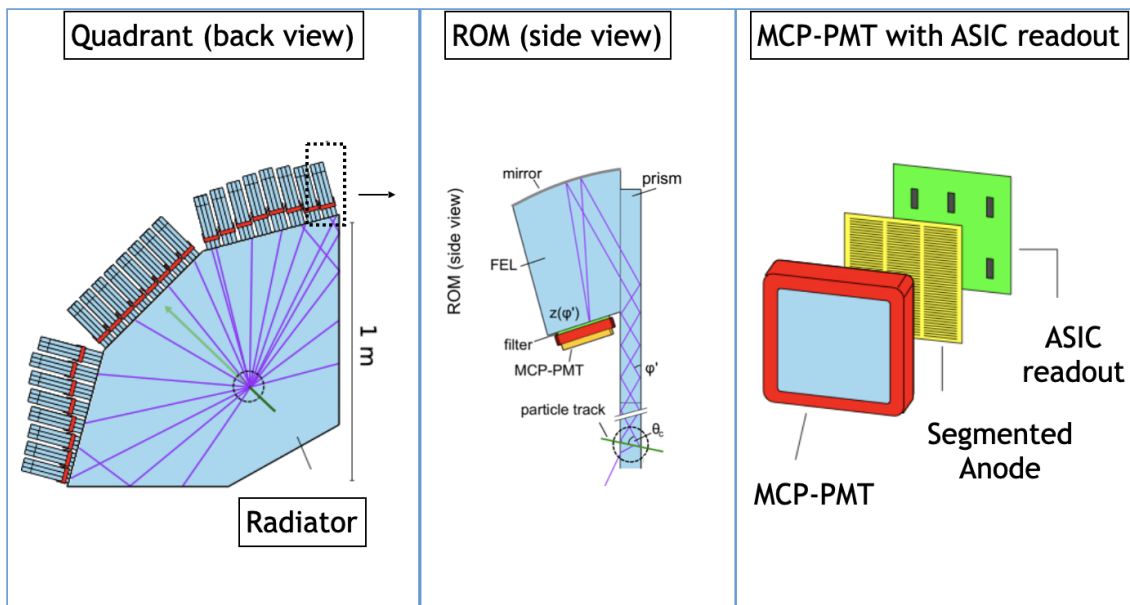


Figure 4.3.: Left: A quadrant with exemplary particle tracks. The green arrow represents the charged particle, where the purple ones are the photons. There are 24 ROMs at the outer rim. Middle: From left drawing, the dashed black rectangular is in side-view. A charged particle traverses the radiator and its emitted Cherenkov photons are internally reflected and focused on the MCP-PMT sensor. Right: The MCP-PMT photocathode and the ASIC readout.

- The vertically aligned quadrant will be prepared for phase-1, including the cooling system.
- The last step will be to prepare a fully equipped EDD with four quadrants for phase-2.

4.3. Assembly

Two different assemblies are planned for the two project phases of the EDD construction. The prototype is planned to be built for phase-1 with 16 ROMs for one quadrant. The full assembly of the EDD will be done for phase-2 of the experiment. For both phases some steps are similar:

- The 96 ROMs will be prepared including 288 optical elements with the corresponding sensor for phase-2. The 16 ROMs with 48 optical elements will be prepared for phase-1.

4. The Disc DIRC Detector

- The ASIC readout system will be directly connected to the sensor anodes without using any cable.
- ROM coupling to radiator will be done in horizontal position.
- The ROMs will be glued to the side of the quadrant(s).
- The quadrant(s) will be stabilized with a cross; afterwards, the cross will be positioned on a bagel-shaped mounting plate in a vertical position.
- For phase-1 the custom design PCB will be used with an existing DAQ system of TOFPET2 PETsys. If the custom design PCB does not require any additional modifications, it can be used for phase-2. The PANDA synchronization and clock will be used for both phases.

After these steps followed, the EDD will be loaded to the TS which is shown on the left in Figure 4.4. On the right, the CAD drawing of the fully equipped EDD can be seen almost completely except for the cables and the cooling pipes.

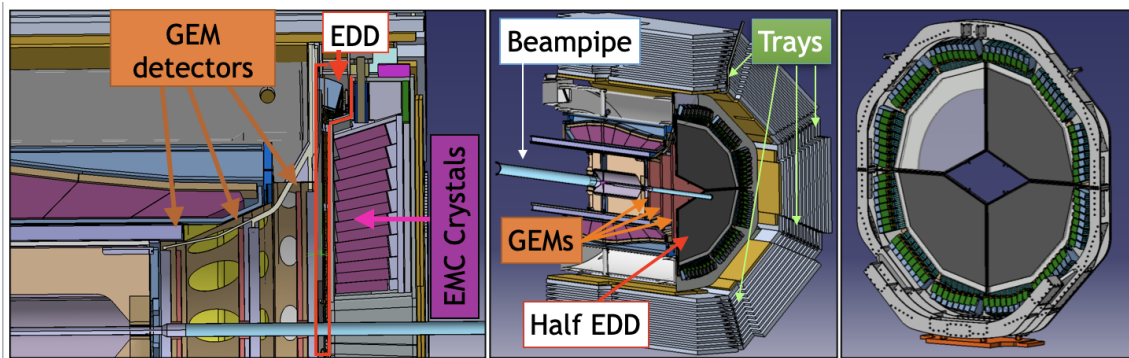


Figure 4.4.: Left: The TS of the PANDA detector from the side view. The EDD is sandwiched between the Gas Electron Multiplier (GEM) and Electro Magnetic Calorimeter (EMC) detectors. Middle: The EDD view with hidden neighboring detectors. Right: The EDD in full size with its four quadrants.

The EDD detector can be identified as being sandwiched between the GEM and endcap EMC. In the middle drawing, the endcap EMC and the muon system is made invisible to get a better understanding of the EDD position. The interaction point (IP) with the surrounding sub-detectors can be seen. The antiproton beam is entering from the left side via the blue colored pipe and interacts with the hydrogen target at the IP. The EDD is positioned 1900 mm away from the IP at the endcap region of the TS. In the center of Figure 4.4 four trays can be seen. The upper tray is reserved for GEM, and the side ones are for Endcap EMC. The bottom tray is reserved for the EDD. Those trays are entering the cryostat from the endcap region. The cryostat in Figure 4.4 covers the detectors and provides low temperature. Coils are responsible for providing a magnetic field. The

magnetic field as a function of the position is shown in Figure 4.5. The interaction point is defined as origin and the z-axis increases with the direction through the EDD. The color axis in the plots shows the magnitude of the magnetic field. The right panel in Figure 4.5 shows the simulation of the magnetic field around the EDD region.

4.4. Mechanical Components for EDD

The EDD is designed with a combination of the several components in different sizes which are made of an aluminum. The MP is the biggest component in order to cover the outer rim of the entire detector. It will carry four quadrants with the help of a 1-2 mm thin stabilizing cross (SC). The MP and SC will distribute the load equally to the holding structure. The thickness of the MP is 15 mm, and it will be mounted to the upstream side of the holding structure of the EMC. Additional screws are added to the holding structure in order to provide the required support for the MP [Etz17]. The weight of one radiator is around 50 kg and whole EDD is expected to be around 400 kg including the ROMs and additional components.

The smaller components are used in a larger quantity due to their repetitive arrangement for each quadrant. One ROM case encloses three FELs, prisms and one MCP-PMT placed on the ROM-case with an MCP-PMT holder. Eight ROMs per side are positioned with a 1 mm distance between the MCP-PMT holders. Due to the potential condensation on the optical surfaces, it is decided to keep the surface clean with a permanent gas flow. In order to allow dry nitrogen gas flow along the optical surfaces, the optical elements should not fully contact with the light-tight cases which is also critical for keeping total inner reflection. To create a 1 mm distance between the optical elements and the ROM inner case, they are held up from the optically non-critical surfaces. Since the cleaning of the optical elements is crucial, different designs of the gas containment were discussed in the previous years. The latest discussion was to have an additional volume to cover the 8 ROMs per side [Etz17]. However, the spatial limits do not allow to put an extra volume around the ROMs. Instead, the ROM case is planned to be designed both light-tight and gas-tight. This will be done by reshaping of the ROM case by covering only the optical elements and excluding the readout electronics.

The readout of one ROM is a system equipped with a custom design PCB and a sensor. A sensor will be powered by a high voltage between 2000 V and 3000 V via high voltage (HV) cables. The custom design PCB will be powered via two FEASTMP [CER] DC-DC modules with given 12 V input, and the output voltage of 3.5 V and 1.2 V. FEASTMP modules are designed to work in magnetic fields. Some electronic elements can get hot in time and require a dedicated cooling system that will be provided by cooling pipes. The cables and the cooling pipes will be sent through to each detector via trays. Due to the solenoid magnet, the magnetic field around the FEL is around 1 T. Thus, the electronic components should be non-magnetic and radiation hard in order to be used for the full PANDA running period.

4. The Disc DIRC Detector

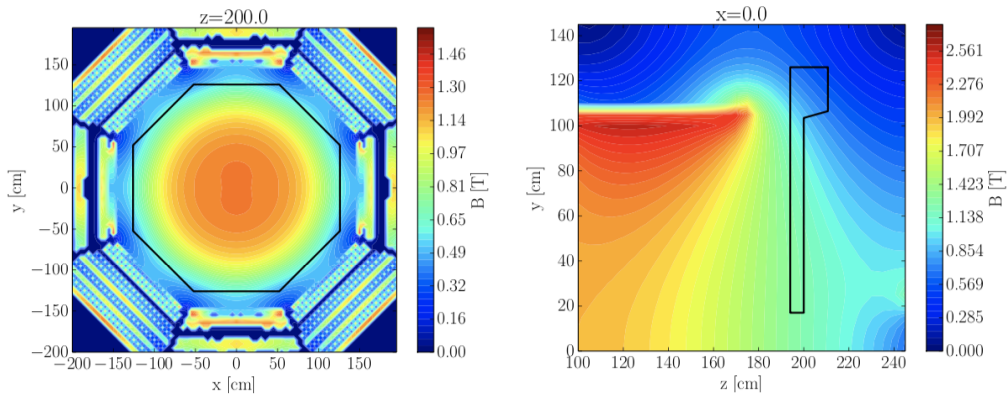


Figure 4.5.: Left: The magnetic field depending on the position in the Endcap region ($z = 200$ cm). Right: Magnetic field distribution depending on the distance from the interaction point is shown. The limits of the FEL and the radiator are shown with black frames in the magnetic field region [Mer14].

4.5. Spatial Constraints

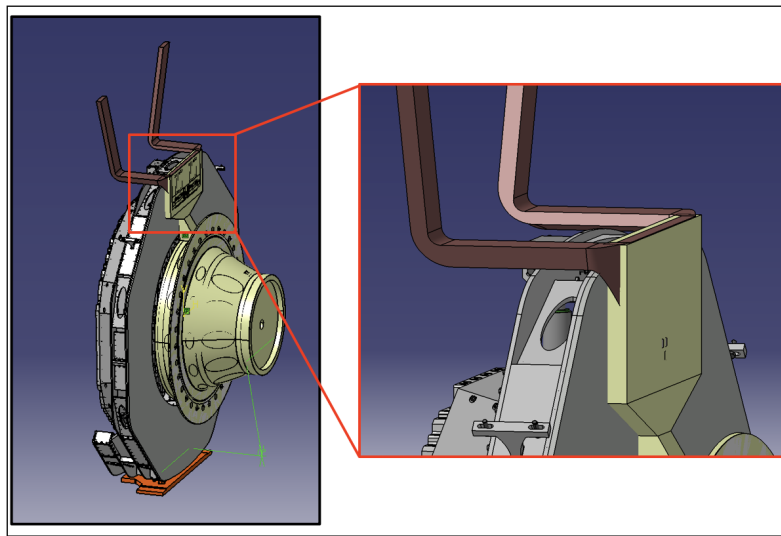


Figure 4.6.: The GEM cable bundle is colliding with the MP of EDD.

There are spatial constraints determined in radial and z -direction due to the space of neighbouring detectors occupied from upstream and downstream direction. In the upstream direction, the GEM detector is positioned in front of the EDD. In Figure 4.6, the GEM detector with the cage around is shown. The cable bundle is oriented through the NNE (North-North-East) and NNW (North-North-West) trays by passing the upstream direction of the MP. The colliding region between the GEM cable bundle and EDD is

framed in red and zoomed in on the right. The rectangular shaped bundle cage is colliding with the 15 mm MP. For the colliding parts from the MP and GEM cable bundle, the mounting plate is decided to be made thinner from 15 mm to 10 mm for these critical angles in Figure 4.6 [Was21].

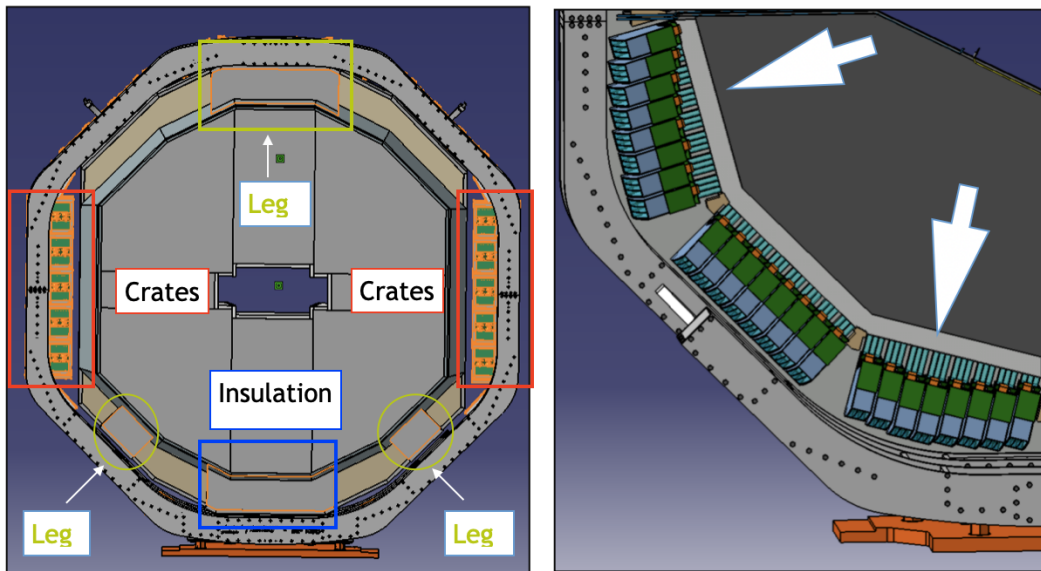


Figure 4.7.: Left: The framed parts show the limited spatial regions for EDD in the z-direction. Right: The ROM position differs due to the EMC insulation in the radial direction.

In Figure 4.7, the constraints in the downstream direction are shown for radial and z-direction. The EMC insulation and the restrictions can be seen in Figure 4.7 on the left. The thickness of the EMC insulation reduces the space in z-direction for the EDD components such as electronics, cooling system, cabling, etc. There are two crates at the sides of the holding structure that limit the space due to the bending radius of the cables. The insulation part at the bottom side is one of the most limited regions since space is reserved for cooling pipes. The space reserved for three legs to distribute the weight and to stabilize Endcap EMC in Figure 4.7 is another constraint for EDD. Enough space is available only for certain areas. In the right drawing in Figure 4.7, one can see the bars with different lengths for each ROM. The insulation of the EMC alters the bar lengths as a function of the radial position. If the ROM components are designed for the most limited region, same design can be used for any position.

In order to find solutions for the limited space, different options have been discussed. Since the Endcap EMC insulation has already been produced, there was no space available from the downstream direction. From the upstream side, 23 mm was requested from the GEM detector side. Since the minimum cable diameter has been used, the cable bundle cannot be designed in a smaller dimension. As a result of the discussions, there is cur-

4. The Disc DIRC Detector

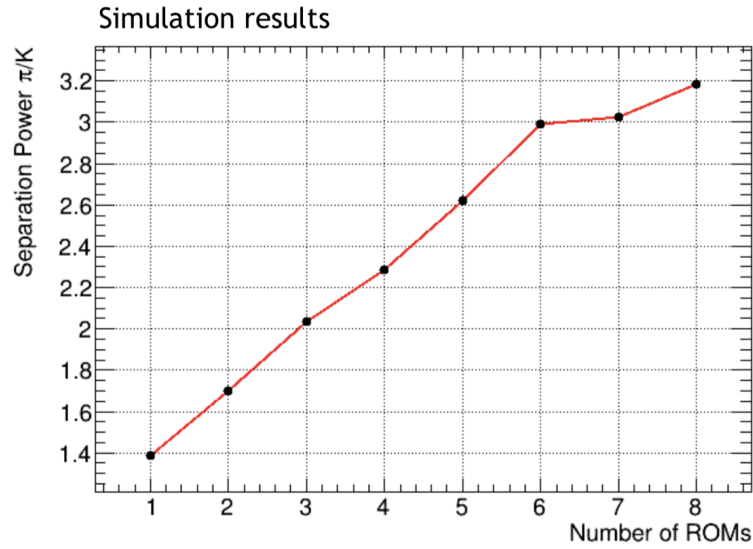


Figure 4.8.: The efficiency at 4 GeV/c momentum depending on the number of ROMs based on a MC simulation.

rently not enough space for fully equipped EDD. One of the suggested solution would be to remove one of the planes of the muon detectors to obtain enough space for the EDD. Since this is a big decision, it was decided to optimize the EDD system by keeping its performance at a high level. If the optimization does not provide the required performance, removing one of the planes of the muon detectors could be discussed. In order to optimize the system, two options are foreseen. The first one is to decrease the number of ROMs until six instead of eight per side. The second option would be the enclose less than three bars or even thinner bars and focusing elements as a ROM. These two options can be applied together or separately. The former option can keep the performance of the EDD same till 4 GeV/c momentum until six ROMs per side according to the simulations in Figure 4.8. Moreover, the custom design PCB can be mounted at the side of the ROM case instead of the top of it. Hence, the required distance in z-direction somehow can be compensated from the side of the ROM case. The latter option is still under investigation.

4.6. Sensor choice

The EDD requires a sensor that is able to detect single photons. The sensor provides a low intensity analog output signal at the anode. Depending on the anode geometry, the position of the anode gives the required information to calculate the Cherenkov angle by using a *backward reconstruction method*. Many sensor choices were discussed in the past such as dSiPMs, PMTs, and Micro Channel Plate Photo Multiplier Tubes (MCP-PMT). The mentioned photo-sensors have many differences but the working principle is similar. When the photon hits a photocathode, it generates a photo-electron. This photo-electron

is accelerated by an internal electric field which provides enough energy to create further generations of electrons. These steps continue by a chain of the same method until reaching the internal gain of around 10^5 to 10^7 . In order to choose the most applicable sensor, many aspects have to be considered regarding the requirements of the EDD and the environmental factors in the TS of PANDA. The most suitable sensor is expected to have a reasonably small dark count rate, a high granularity of the anode structure, a long lifetime during the PANDA operational time, a good collection efficiency and a high quantum efficiency. In addition to internal parameters, the sensor is expected to be radiation hard and ready to work in the magnetic field of the TS of PANDA. In the past PMTs have been considered for detection purposes; however, due to their incompatibility with the magnetic field, other choices were discussed. One of the most preferred option is SiPMs due to their great advantages compared to PMTs. They can be powered with low voltages between 25 V to 70 V instead of 1000 V to 3000 V. Two SiPM structures are

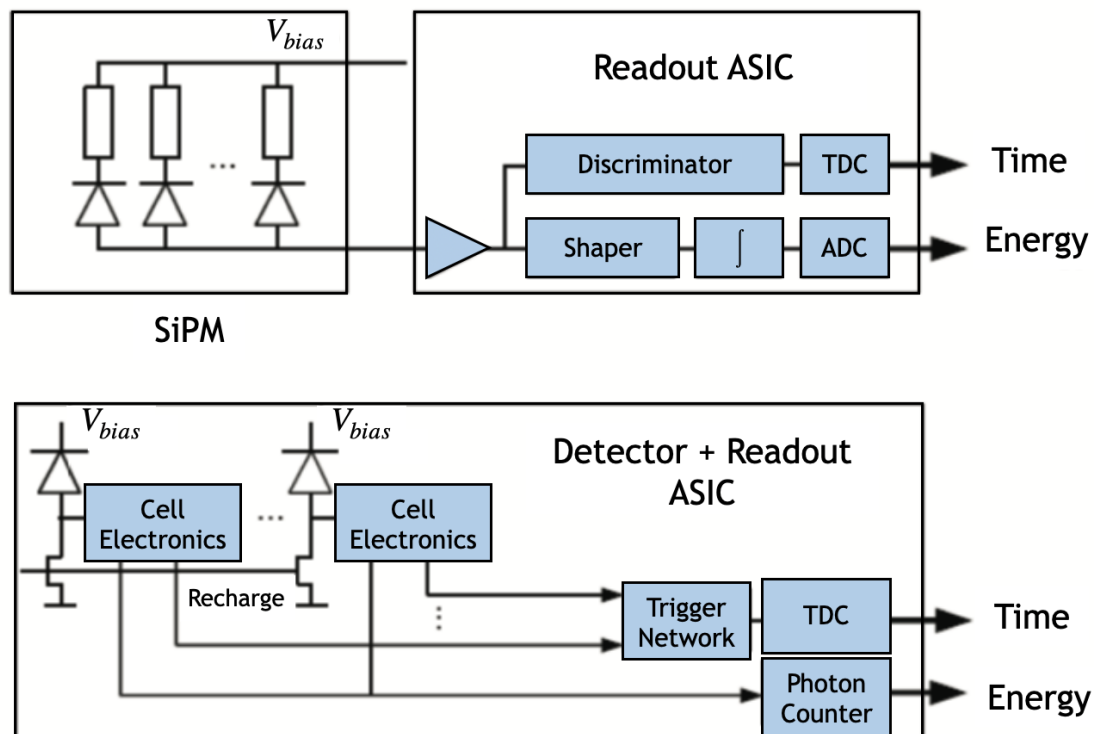


Figure 4.9.: Top: Analog SiPM (aSiPM) structure with a readout system. Bottom: Digital SiPM (dSiPM) structure with a CMOS technology. [HFDT12].

shown in Figure 4.9. A dSiPM is a good suggestion where the limits of an analog SiPM is not meeting the system requirements. In order to understand the difference between the aSiPMs and dSiPMs, their readout is shown in Figure 4.9 [HFDT12]. From the top,

4. The Disc DIRC Detector

the aSiPMs are connected in parallel. The output signal is an analog sum of all connected aSiPMs, and is transmitted to the readout system. The dSiPM structure in the bottom shows the combination of the detector and the readout system in one chip. Each dSiPM is integrated to the CMOS circuits and connected to its own readout circuit. This is helpful for quenching and recharging each dSiPM. However, existing SiPMs do not provide the required spatial resolution and are not sufficiently radiation hard. With these difficulties in mind, the MCP-PMTs [L⁺20] became the sensors of choice for EDD. The MCP-PMTs have a sufficiently compact size which is quite crucial due to the spatial constraints in the TS. They provide excellent timing properties such as fast rise time and low transit time spread, and have a high spatial resolution due to high granularity anode [Cho10]. The working principle of the MCP-PMT is visualized in Figure 4.10. The MCP-PMT requires a negative high voltage between -2000 V and -3000 V . The HV divider splits the high voltage by the resistors to provide the required voltage gradient between the layers of the MCP-PMT. In Figure 4.10 on the left, the photon (red) hits the photocathode after reaching the sensor entry window. It generates a photo-electron that is accelerated by an electric field between photocathode and MCP-in. The photoelectron reaches one of the MCP-PMT pores and starts a multiplication chain. The photoelectron shower reaches the anodes. The photoelectron shower may hit more than one anode as it can be seen on in Figure 4.10. The signal shapes at the anodes can be seen on the right plot in Figure 4.10. This concurrent effect is called charge sharing and it can be decreased with well defined magnetic field lines.

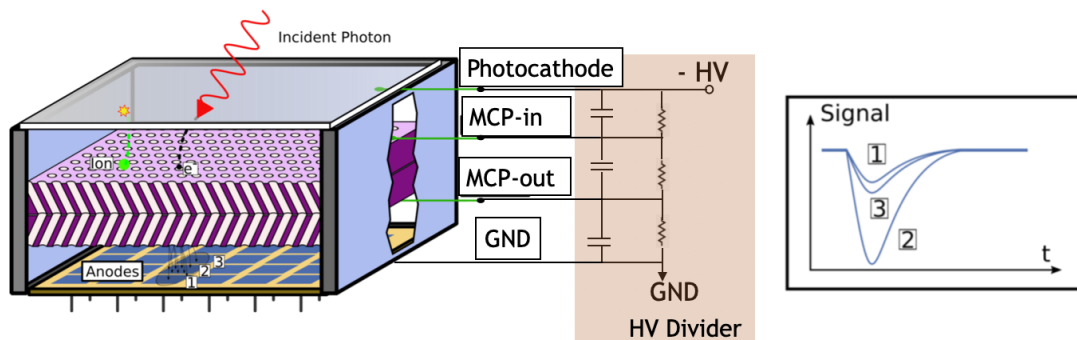


Figure 4.10.: The working principle of the MCP-PMT is sketched in the left figure. Right side refers to the HV-divider that provides the required voltage gradient between photocathode, MCP-in, MCP-out and ground. The electron multiplication is visualized for adjacent micro-channels. As a result the output signal reaches the MCP pins. The right plot shows the signal amplitudes of three neighboring pins due to the charge sharing [Rie17].

There are some internal and external factors which determine the performance of the MCP-PMT. The shape of the pore structures is one of the determining factors of the MCP-PMT performance. In Figure 4.11, two different geometries of the pin structures are visualized. The left drawing shows the electron multiplication on through one straight

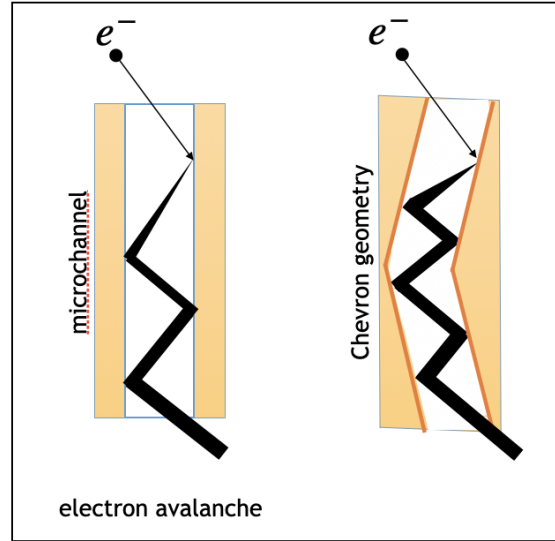


Figure 4.11.: Left: A straight structure of the MCP-PMT pores with an incoming electron is shown. Right: The Chevron geometry of the pore structure is visualized.

microchannel. The production of the MCP-PMT with straight design is very rare nowadays since there are more preferable options. In the right, the Chevron geometry is used for designing the EDD sensors. A tilted angle approx. $\approx 10^\circ$ in opposite directions from the center of the pin. The tilting geometry reduces the ion backflow to the photocathode which extends the lifetime of the MCP-PMT. With the tilting geometry, the hit probability of photoelectron to the microchannel wall is increased. This will also affect the amount of interactions of the electrons with the wall and leads to 10^6 internal gain. In addition to these two effects, the first strike of incoming photoelectrons on the pins is well oriented.

One of the internal factors is the detection efficiency which can be defined by the probability of detecting a single photon on the photocathode

$$\varepsilon_P = \frac{N_{\gamma-det}}{N_{\gamma-in}} \quad (4.8)$$

where the $N_{\gamma-det}$ refers to detected photons and $N_{\gamma-in}$ refers to number of incoming photons. The detection efficiency can also be defined by the multiplication of quantum and collection efficiency

$$\varepsilon_P = \varepsilon_q \cdot \varepsilon_c. \quad (4.9)$$

ε_c is a collection efficiency which is determined by the number of holes and the active area of the MCP-PMT

$$\varepsilon_P = \frac{N_\gamma \pi r^2}{A}. \quad (4.10)$$

The collection efficiency can be increased by changing the shape of micro-channels. This can lead to time shifts of the output signal due to the travel time of additional electrons

4. The Disc DIRC Detector

[Sch17]. On the other hand, it is quite important to use MCP-PMTs for reaching the 10 years of PANDA operational time without a significant loss in performance and quantum efficiency. This can be achieved by reducing the accumulation of ion backflow onto the photocathode by applying several techniques. One of the applied technique is based on covering pores of the MCP-PMT with an atomic layer deposition (ALD) which meets the EDD requirements [B⁺20].

External factors such as the magnetic field or the radiation level also affect the performance of MCP-PMT. The photo-electron avalanche may be shared between the neighboring pins as shown before. This leads to a time shift that can be corrected by applying time offset correction. Depending on the direction of the magnetic field, the cloud of the electrons can be focused onto one pin. This leads to a suppression of the charge sharing effect. These effects will be studied in the future by using the lab facilities for radiation studies and the magnet box which will be discussed in chapter 5. Currently, the ALD coating technique reduces the ageing effect from irradiation.

4.7. Readout System

The readout system is crucial to determine the performance of the detector. It is covering the stages starting from the analog signals to the DAQ system of PANDA. Both slow control and fast front-end electronics contribute to the management and use of this system. For the detector setup, a slow control system provides a supervisory layer to start, stop or change the settings for an experiment. It is quite essential to keep the data quality at high level by controlling the DAQ system under critical circumstances that require immediate intervention by a user via the supervisory layer.

4.7.1. Overview of the Front-end Electronics

Different geometrical designs of the optical system had been studied and explained in different sources [C⁺11, Föh09, KAO⁺96]. Since the thesis focuses on the readout system of the EDD, the evolution of the readout system will be discussed.

In the first picture of Figure 4.12, the readout system for the test beam experiment in 2015 is shown. The readout system of the EDD prototype was based on TRBv3 and PaDiWA boards which was different than the design in 2016 test beam setup in the second picture [Sch17, Etz17]. During the test beam in 2016, TOFPET system was used as a readout system which is close to the current design. Third drawing of Figure 4.12, 108 ROMs were suggested to equip into the final design of the EDD [Mer14] in 2015. Each ROM was planned to plug into one MCP-PMTs which would be directly connected to the intelligent FEE with two rigid boards via flex ribbon cable. This design was never realized since many changes had been applied after 2015 starting from decreasing the number of the ASICs. Many electronic elements were also changed due to the environmental constraints. Further details related to the electronics will be explained in following sections.

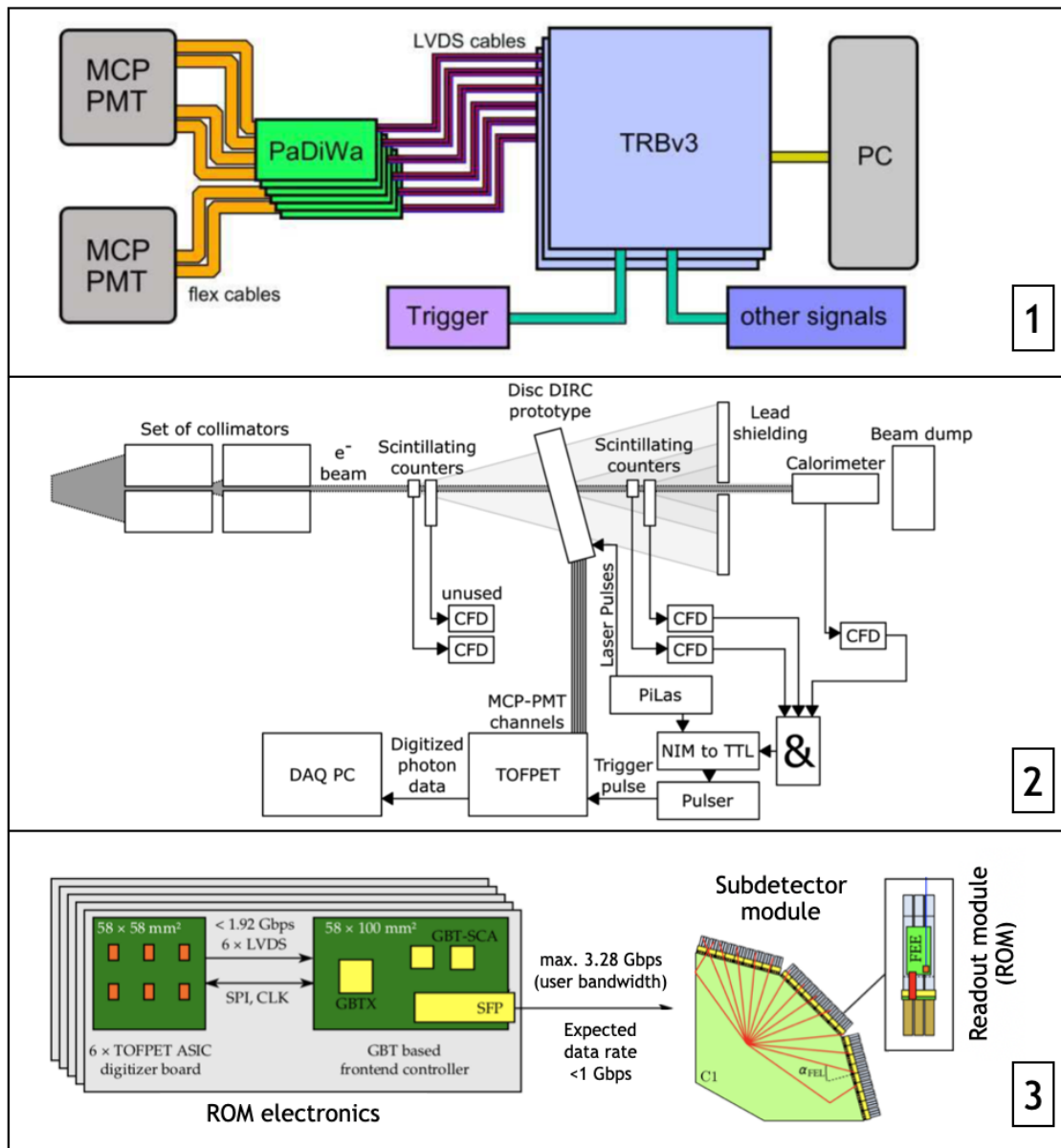


Figure 4.12.: 1: The readout system in 2015 test beam experiment based on TRBv3 with PaDiWa boards [Etz17]. 2: TOFPET readout system was used in 2016 test beam experiments [Sch17]. 3: TOFPET based final readout system was suggested in 2015 [Mer14].

4. The Disc DIRC Detector

4.7.2. Frontend Electronics

The goal for a fast FEE is detecting single photons with a resolution better than 100 ps. The sensor has a multi-anode structure of 384 pins (HAMAMATSU) and/or of 300 pins (PHOTONIS). 300 channels of HAMAMATSU will be used for single photon detection. The EDD is expected to consist of 28.800 anodes in total and the expected hit rate is about 100 kHz per channel, i.e. 30 MHz per ROM. In the high luminosity mode, the expected hit is around $7.2 \cdot 10^8$ per event for each quadrant. In total, $29 \cdot 10^8$ hits per event are expected for the complete EDD. That means the data rate for channel numbers, time stamps, and intensities will be around 11 Gbit/s. In order to digitize analog signals, a fast electronics system, which consists of FPGAs and ASICs, has to be used. The digitized data will be sent to the PANDA data concentrator. In parallel the PANDA clock will be delivered via a bi-directional optical cable. In order to provide communication between the readout system and the SODANET of the PANDA DAQ system [PANDA17a], a compatible type of FPGA has to be used. SODANET is a communication protocol planned to be used for triggerless readout of all PANDA subsystems.

The forward endcap in TS is very a compact region as mentioned before and the EDD will be positioned in a compact space in a magnetic field. Due to that reason, there are some additional requirements that the readout system and the sensor must provide. The readout system has to be compact due to spatial constraints, sustainable enough to work in the magnetic field, and be a radiation-resistant to operate for many years. Considering all constraints and requirements, it was decided to utilize the PETsys TOFPET2 readout system.

In order to achieve a successful readout structure for the final EDD, the readout system was successfully tested and improved. These steps led to great improvements that will be discussed in the following sections.

4.7.3. The TOFPET2 Readout

The PETsys electronics company [pet20] designed the TOFPET2 system that aims at measuring time-of-flight information of photons in positron-emission tomography (PET) applications. It is mainly based on utilizing SiPMs as photosensors. This requires a detection of the positive polarity output signals with an excellent time resolution. The goal of the readout system in the EDD detector is to detect single photons. To achieve this, the MCP-PMTs are used as photosensors with the TOFPET2 system which requires some modifications due to the MCP-PMT signal characteristics. During this section the specifications and components of the TOFPET2 system will be explained as well as the modifications and the custom designs.

The TOFPET2 system is mainly based on a combined performance of ASICs, FPGA, and the DAQ board. The TOFPET2 ASICs digitize up to 64 analog channels, thereby, integrating a DAQ synchronization signal. This signal is provided from the DAQ-board to a so-called fan-out-box. The fan-out-box can distribute the clock signals to the ASICs via μ HDMI cable. The FPGA is implemented on a front-end board D version 2 (FEB/D-v2) which is capable of working with 16 ASICs in parallel. Two TOFPET2 ASICs are

integrated on a front-end module (FEM) which is separated from the FPGA board. In Figure 4.13, one can see such a FEM128 with a face-to-face position of two ASICs attached as T-connector to analog input board on one side and to the digital outputting on the other side. Analog signals reach to the I-board of FEM128 via Samtec cable[sam21] with 32 signal lines. These cables are well-shielded to prevent electronic interference [Rie17]. Eight lines of the cable are reserved for the power lines for SiPMs which are not in use for the MCP-PMT scenario. Four identical Samtec cables can be connected to the I-board. Analog sensor signals are sent to FEB/D-v2 after being digitized by ASICs. A FEB/D-v2 can be connected to eight FEM128s from the S-board via Samtec cables. The digitized signals are transmitted from the FEB/D-v2 board to the fan-out-box and from the fan-out-box to the DAQ board. In Figure 4.13, the FEB/D-v2 connected to the FEM128 with a Samtec cable. The D-board and the FEM with the cable connections can also be seen at the right.

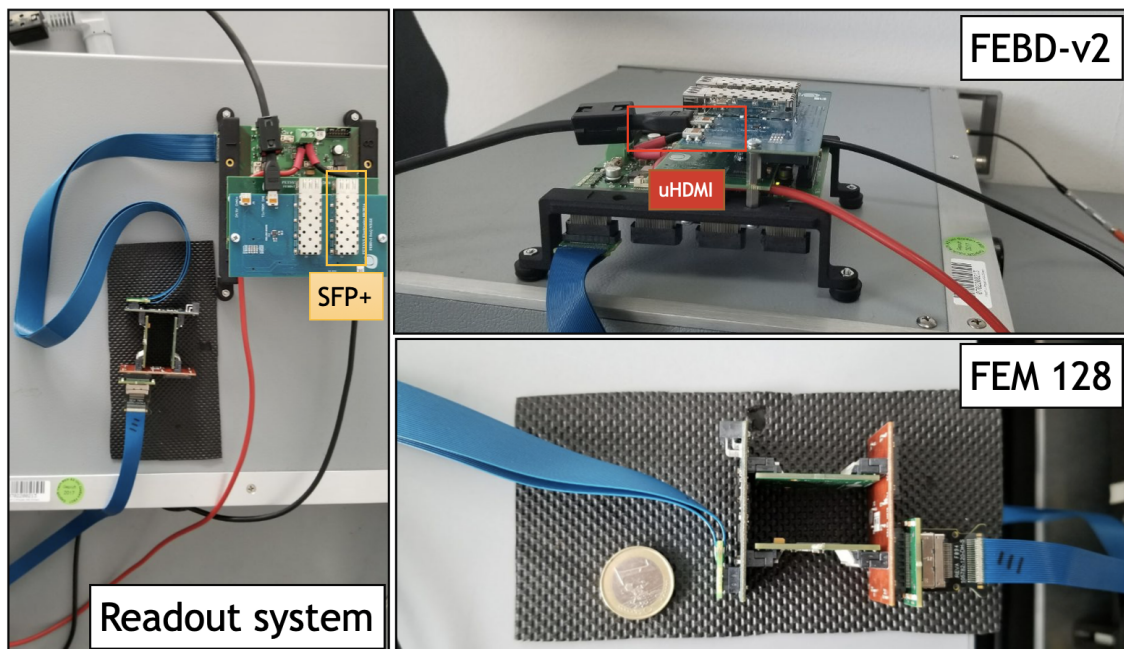


Figure 4.13.: TOFPET2 system with FEM128 and FEBD-v2 board.

Eight ports of FEB/D-v2 correspond to 1024 ASIC channels in total. The FEB/D-v2 has to be powered with 12 V DC at 4 A via one signal (red) and one ground (black) cable as connected in Figure 4.13. The DC-DC converters in FEB/D-v2 board distribute the voltage by dividing it to other electronic components such as the ASICs. The list of required voltages and currents for the components can be seen in table 4.1. The required voltage is less than 6 V and 2 A current for the components.

The layout of the D-board is based one motherboard and two mezzanine boards on top of each other. The middle mezzanine, BIAS16P is designed for the SiPMs needs. The DAQ board mezzanine is a data output mezzanine which sends data frames to the DAQ

4. The Disc DIRC Detector

Voltage	Current	Multiplicity	Total Current
FEM: ASIC & Clock Buffers & ADC			
1.35	0.6	6	3.6
2.5	0.1	6	0.6
FEB/D: FPGA & Clock Buffers & SFP & etc			
1.35	1.8	1	1.8
1.8	0.6	1	0.6
2.5	0.5	1	0.5
3.3	0.4	1	0.4
5	0.01	1	0.01

Table 4.1.: Required voltages and currents for the TOFPET2 electronic components.

board.

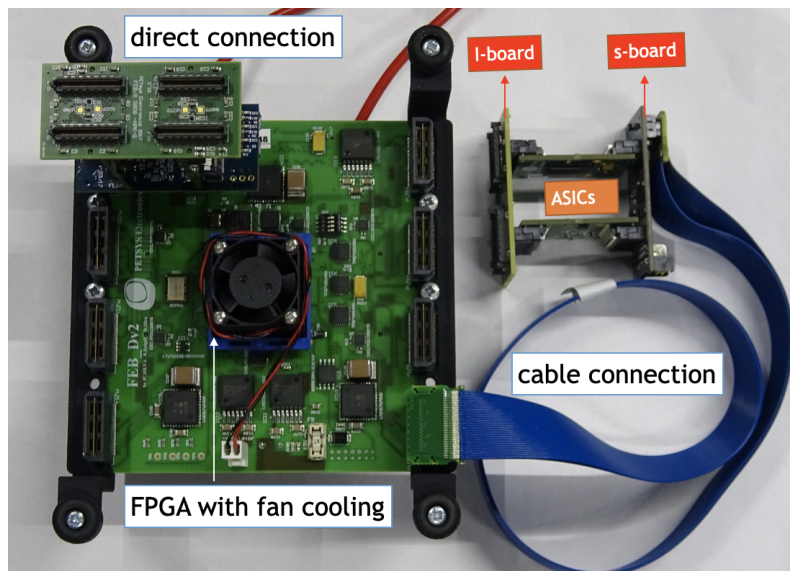


Figure 4.14.: The bottom side of the mother board is connected to the FEM directly or via cable.

The motherboard consists of a Xilinx Kintex 7 FPGA, JTAG connector, FEM ports, mezzanine connector, LEDs, fuses and temperature sensors. The bottom side of the motherboard can be seen in Figure 4.14. The heat from the FPGA is dissipated by using a fan with a power supply. The JTAG connector is used for programming purposes such as debugging and/or flashing the FPGA. The FEM port provides slow control lines, power lines and signal lines for each ASIC. The slow control lines reach the temperature sensors of each FEM and signal lines fetch the digitized data from the ASICs. The FEMs can be connected to the ports directly or via a flat Samtec cable (see figure 4.14). Eight fuses protect each power lines in the board. The LEDs have been inactivated for the purposes

of the dark mode system in an experimental area.

Since the TOFPET2 system is designed for SiPMs, the BUS 16P mezzanine board mainly consist of voltage adjustment and control channels for SiPMs. There are also two blocks of DC-DC converters for providing a required voltage to activate the SiPMs via 8 channels from D-board to FEM module. This voltage can be controlled and set to zero by using the software.

The DAQ mezzanine board is the data output mezzanine board that can be seen in Figure 4.13 with two optical high speed link SFP+ connections, two μ HDMI connectors; one is for a daisy chain. Several FEB/D-v2 boards can be daisy-chained to the maximum event rate which is 10^8 events/s. This feature will not be used for the EDD readout system. The other μ HDMI connector is reserved for data transmission and for delivering the clock & synchronization signal from the DAQ system via a μ HDMI-to-HDMI cable. The system clock frequency is 200 MHz. One of the SFP+ cages can also be used for data transmission by utilizing a fiber optic cable.

The TOFPET2 ASICs are using a CMOS technology at 110 nm integration scale. Calibration can be applied for each separate ASIC channel, and different threshold settings can be applied for event selection. The data can be recorded in Time-over-Threshold (ToT) or QDC (Charge-to-Digital Converter) mode depending on the desired setup. The maximum data rate is 3.2 Gb/s for an ASIC. The TOFPET2 ASICs also require a cooling system either with a liquid or by using a fan.

4.7.4. The readout system of the final EDD for Phase-2

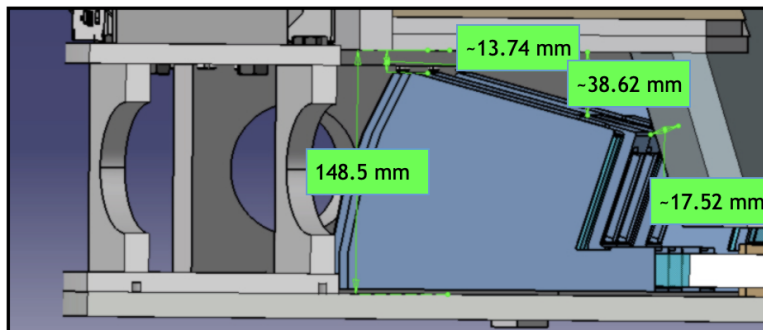


Figure 4.15.: Space constraints in one of the limited regions.

One of the crucial structure is designing a readout system that would fit in a limited space which is reserved for the final EDD. The available space for one of the limited regions can be seen in Figure 4.15. For the readout system, the cables and the cooling structure, a maximum of 34 mm and a minimum of 9 mm space is available, including 4 mm safety margins from neighbouring detectors. From the backside of the ROM case, a holding structure is already limiting the space, since the bar length cannot be changed due to the EMC insulation in a radial direction. Considering these constraints, a PCB must be designed in a way that could fit into space with all components and with a

4. The Disc DIRC Detector

dedicated cooling system. The modifications/changes have to be done according to the requirements below:

- The existing TOFPET2 system contains a middle mezzanine board that has components only for SiPMs. For the readout design of final EDD with externally powered MCP-PMTs, these components can be excluded.
- The geometry of existing FEB/D-v2 and FEM128 can be combined in one compact PCB to fit into the limited space.
- The current DC-DC converters are not working in a magnetic field of 1 T. They need to be replaced by another type which are magnetic field resistant.
- The materials must be radiation hard.
- The electronic components should be compatible with the PANDA DAQ system.

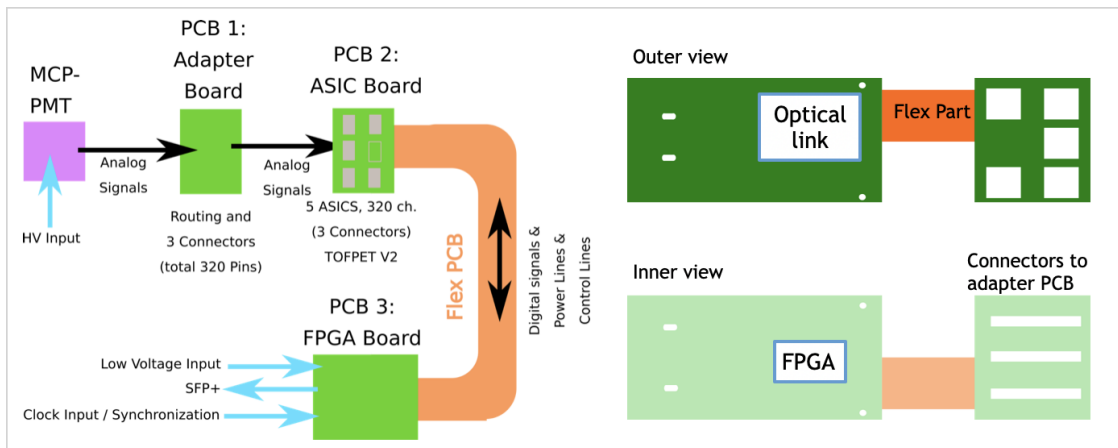


Figure 4.16.: Left: The sketch of the signal flow for custom design PCB, starting from the MCP-PMT signals to FPGA board. Right: The sketch of the custom design PCB with inner view focus towards the ROM surface.

As a first step, the geometry of the existing TOFPET2 electronics are modified by combining FEM128 and FEB/D-v2 into a custom design PCB, thereby removing SiPM related components. Considering the ROM shape and sensor position, two rigid PCB parts are connected with one flex part at one of their short edges. The suggested PCB design with the logic behind is shown in Figure 4.16 in the flow chart on the left and the PCB design on the right. The flow is starting from the left side of the sketch. The MCP-PMT is powered with high voltage (HV) between 2 kV and 3 kV. The analog signals are routed by an adaptor board to PCB2 which is called ASIC board. The adaptor board provides a connection between the sensor anodes and ASIC connectors. The adaptor has to be designed according to the anode geometry of the MCP-PMT sensor. Five ASICs digitize

the signals with 200 MHz clock frequency. An option of six ASICs has been rejected because of spatial constraints, decreasing the number of ASICs to five leads to losing 64 channels. This doesn't affect the system if the sensor choice would be a PHOTONIS with 100×3 anodes. If the sensor choice would be HAMAMATSU with 128×6 anodes, 84 channels would not be covered. This should not effect efficiency substantially. After the digitization, the signals will be sent to the FPGA board by using the flex PCB. In parallel, a flex PCB will transmit the power lines for ASICs and control lines for temperature sensors. The FPGA board (PCB 3) will be powered by low voltage (LV) cables, send the data buffers to the DAQ system via optical SFP+ connector and get clock input from the central DAQ system. In the right drawing in Figure 4.16, the outer and inner view of the desired PCB design is shown.

Optimization of the ROM Design

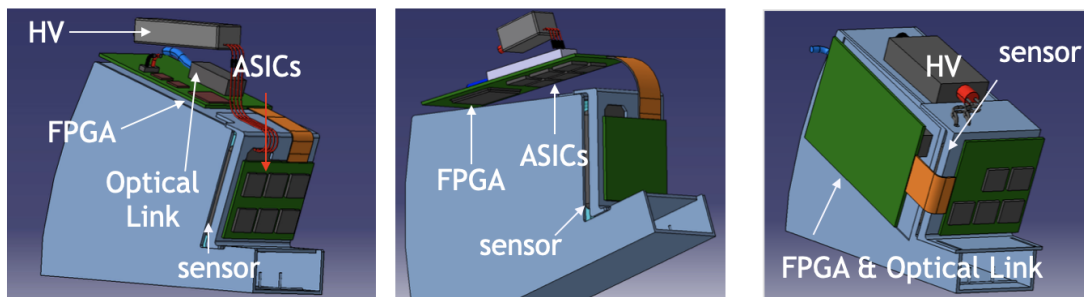


Figure 4.17.: Three different design for the limited regions.

In order to reach the best solution concerning to the spatial constraints, three different ROM versions have been studied by using CATIA designs (see Figure 4.17). Both designs have two rigid parts with one flex part in-between. Moreover, the rigid-flex design is directly connected to an adaptor board without any cables. In order to detect all sensor anodes, five ASICs for PHOTONIS sensors 100×3 or six ASICs for HAMAMATSU sensor 128×6 should be used. These three designs show differences regarding the positioning of the components such as FPGA, and ASICs. Since they require a dedicated cooling system, their position defines the geometry of a cooling system in addition.

First design

For the first design on the left in Figure 4.17, six ASICs are positioned on the board which is connected to the analog signals via an adaptor board. The analog signals are digitized and then sent to the second rigid board via a flex-PCB. The flex PCB is orange-colored, carrying digital signal lines to the FPGA-board. The optical link and FPGA are placed on the second rigid PCB. This design requires a cooling system for two different separated rigid parts. Due to the spatial constraints, different cooling pipes with liquid inside may

4. *The Disc DIRC Detector*

not fit the reserved space. The heat pipes contacted to a surface which is cooled down by cooling pipes can be considered since it provides a safer environment around electronics.

Second design

In the middle drawing, six ASICs, an FPGA and an optical link put in the same board but on different surfaces. That means a cooling design for only one part. However, a minimum of 300 analog signals are routed to second rigid part via flex PCB. This is not preferable since analog signals can be affected irreversibly due to different problems such as a cross talk, reflection, antenna effect or etc. Due to that reason, immediate digitization is more advantageous rather than sending 300 analog signals via flex-board. In addition, the cooling power for such compact area may require a higher performance compared to the first design.

Third design

The third design in the right figure is suggested considering the constraints in z-directions. In total, five ASICs are decided to use instead of six ASICs since five ASICs can cover all channels of PHOTONIS but for HAMAMATSU scenario, 64 channels will be missing. This will lead to some loss of analog signals but will not affect the detector efficiency according to the rough estimations. The FPGA and the optical link are hidden on the other side of the second rigid part. The alignment of the board is different from the first two boards. This design can be done with only 3×6 ROMs per quadrant. The efficiency for different number of ROMs can be seen in Figure 4.8. The first option and third option can be considered for the final design of the EDD depending on the available space. In the following chapter, the first design with five ASICs will be discussed for the GCS experiment and project phase-1 of PANDA experiment.

4.8. Custom PCB design for the final readout system

A rigid-flex PCB has been developed by PETsys electronics company by applying some modifications to the existing TOFPET2 structure due to the environmental factors such as magnetic field in addition to the spatial ones. A couple of spatial requirements for the EDD led to the design of a compact readout board to be attached to each FEL housing. 3D drawings of the design for both sides can be seen in Figure 4.18 together with their electronic components. The upper figure shows the top outer side of the PCB. The largest part of the PCB is a rigid part with 80 mm length and 60 mm width. In the top side of the PCB, five ASICs are implemented on the smaller rigid part. The ASICs have 64 channels each, and two ASICs correspond to one connector on the inner side of the PCB. These three connectors are designed for the Photonis adaptor boards [Rie17]. For the Hamamatsu sensor, a bridge adaptor will be designed in-between the Hamamatsu adaptor board and the PCB connectors. Analog signals will only travel short distances between the anodes of the sensors and the ASICs. This helps decreasing the probability

4.8. Custom PCB design for the final readout system

of distorting the analog signals. These signals will be digitized by the ASICs. The digitized signals are then transmitted to the second rigid part. The second rigid part consists mainly of a VTRX+ connector [JT] for sending the data to the DAQ system, FPGA, JTAG and μ HDMI. On the inner side of the PCB, an FPGA can be seen as one of the biggest components. The firmware of the FPGA can be flashed by using the JTAG connector. The JTAG connector can be used for debugging purposes as well. It is already known that standard SFP+ connector is not working in a strong magnetic field which results in a replacement of the SFP+ connector to VTRX+. The VTRX+ connector is an optical bi-directional link between the FEE board and the DAQ system. The VTRX+ connector is also resistant to a high radiation level. The clock & synchronization signal will be provided by a μ HDMI cable which will get the information from the fan-out-box. All these components require dedicated voltages that will be provided by DC-DC converters. The existing TOFPET2 readout system includes DC-DC converters which cannot work in a magnetic field. Due to that reason, FEASTMP [CER] modules are implemented as DC-DC converters to power the PCB with 2.5 V and 1.35 V. The FEASTMP module is a radiation hard (200 Mrad(Si) total ionizing dose) DC DC converter that can work in a magnetic field of 40,000 Gauss. In the TOFPET2 system, the FPGA is cooled with a fan which is not implemented for the custom design PCB. The FPGA and ASICs will be cooled down from the inner side of the PCB with liquid cooling instead of air cooling. The temperature of the modules should be kept around 18°C. The cooling system will be explained with details in the following chapter. There are some modifications applied to the existing TOFPET2 system to provide a readout system for permanent runs. These modifications can be summarized as follows:

- SFP+ connection was changed to the VTRX+ connection which is radiation hard and it can work under the magnetic field.
- μ HDMI will be used for getting clock & synchronization signal during the test experiments in GCS.
- The DC-DC converters are changed to FEASTMP modules.
- FPGA, ASICs and FEAST modules require a liquid cooling for the final design.

4.8.1. Custom PCB test

The PCB is planned to be delivered in the first half of 2021. It will be used to measure Cherenkov photons in GCS after initial function checks. The reliability, readout rate and sensitivity in the magnetic field of the PCB can be tested with a laser and optional magnetic field. The laser can lighten the surface of photocathode or scan the whole surface with the step-size of the anode pixel width of about 0.5 mm. This can be achieved by using precision linear stages in the vertical and horizontal direction. In addition to the axis change of the photocathode, the laser fiber should be able to move forward and backwards by using a third linear stage for focusing purposes. These scans can be repeated

4. The Disc DIRC Detector

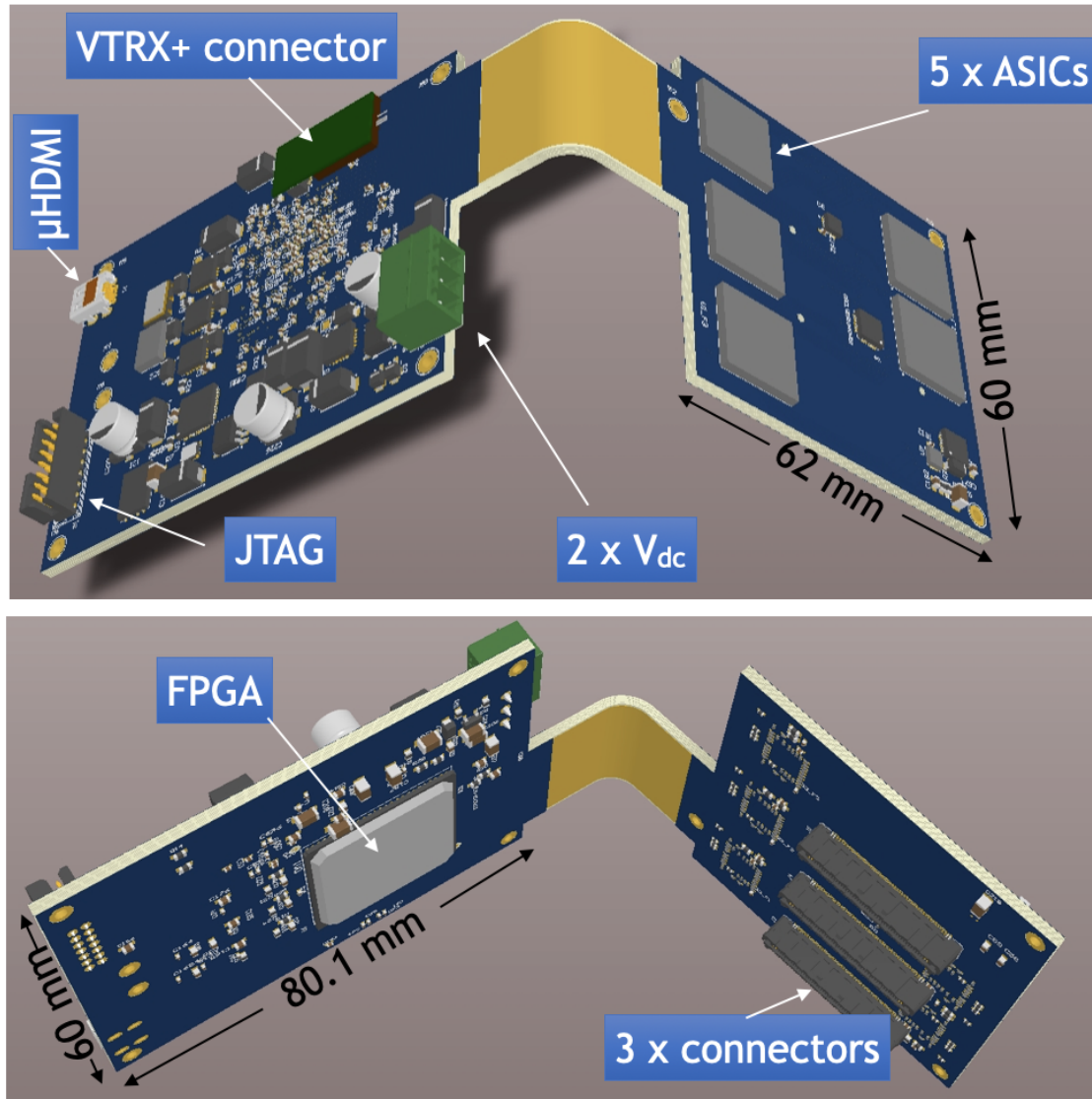


Figure 4.18.: 3D CAD version of the custom design PCB from outer and inner view.

in a magnetic field to study the impact of the magnetic field on the readout system. Considering the necessity of a light-tight system for the scans, dedicated box was decided to be designed to perform the first tests of the custom PCB at Giessen University. A sketch of the magnet box is shown in Figure 4.19. The sketch illustrates to a closed light-tight design with two magnets at two edges and the PCB in the center. There is a rotation table to position the laser holder and the PCB holder. The rotation table provides an angle scan between 0° to 24° in the magnetic field. Data will be sent out of the box via an optical link between the PCB and the DAQ system. The clock and synchronization signal will be provided via μ HDMI. In order to run the sensor with an operational voltage, four HV cables

4.8. Custom PCB design for the final readout system

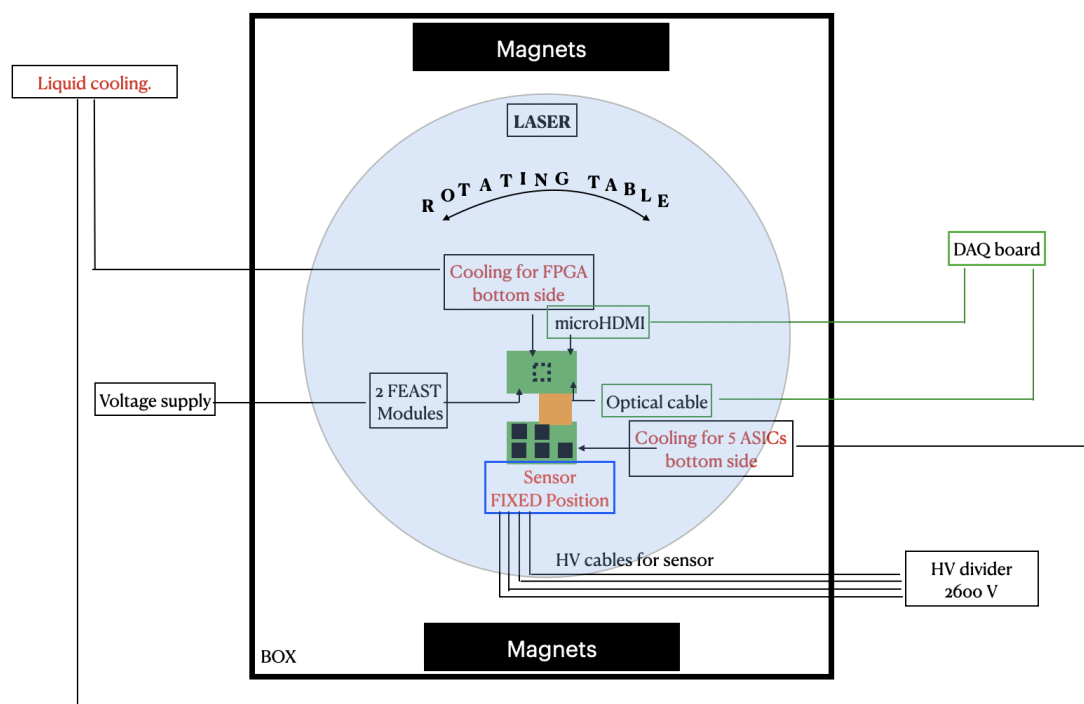


Figure 4.19.: The sketch of the box designed for testing the custom designed PCB.

have to be connected to the box. The voltage applied to the HV divider may be varied between 2 kV to 3 kV depending on the sensor type. In addition to the sensor, the PCB has to be powered with two FEASTMP DC-DC modules. The FEASTMP modules have one input which can vary between 5 V to 12 V and provide an output of 1.5 V or 3.5 V for the PCB. They can be placed inside or outside the box with advantage and disadvantages. If they are put outside, a separate cooling system has to be designed and the magnetic field effects cannot be tested then. On the other hand, they do not occupy space inside the box. If the other scenario is applied, they can be tested in a magnetic field and cooled down together with the PCB using the same cooling system but additional space will be occupied. As it is mentioned before, a dedicated cooling system is an obligation for such a compact electronics system. For the inside of the box, the liquid cooling system will be provided for ASICs, FPGA, FEASTMP modules, etc. The details of the cooling system will be explained in the following sections.

The 3D design of the test box can be seen in Figure 4.20 in four different perspectives. The dimension of the box is $60 (L) \times 65 (H) \times 50 (W) \text{ cm}^3$ which is generously big for different alignments of the custom design PCB. In the first view, the height of the box is supported with extra four legs to provide enough space for the hand wheel. The hand wheel is directly connected to the rotation table. Cable feedthroughs at the right half and feedthroughs for cooling pipes on the left half. There are extra feedthrough holes

4. The Disc DIRC Detector

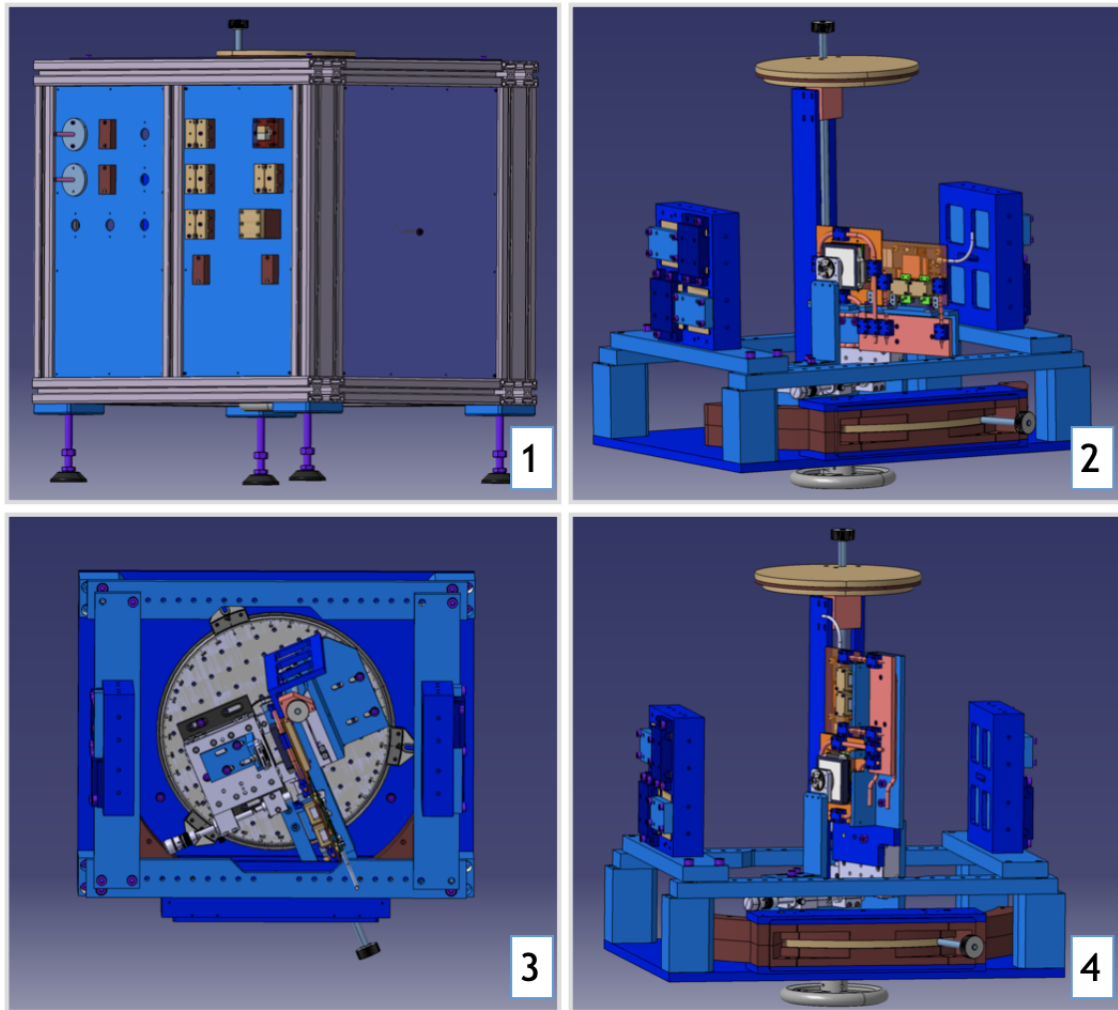


Figure 4.20.: The 3D drawing of the light-tight box for testing purposes of custom design PCB. 1: The isometric view of a closed box. 2: The inside of the box with PCB implemented in a horizontal way. 3: Top view of the box. 4: The box with a vertically positioned PCB.

provided modifications in the future. The laser feedthrough is implemented on the wall of the shorter edge. In order to provide similar environmental conditions as in TS of PANDA, magnets are implemented at two opposite sides of the box, as shown in the second drawing of Figure 4.20. With the help of the Item profiles, the magnets can be moved closer to the PCB and MCP-PMT or moved further away. The PCB is positioned in the middle of the magnets and resting on top of the two linear stages. These two $x - y$ stages are connected to interfering each other. They provide scanning each anode in 2D by an up-down and left-right movement. The top view in the third drawing shows the

4.8. Custom PCB design for the final readout system

rotation table which is the base for all components except the magnets. The laser is able to move forwards-backwards with the help of a linear stage which is also positioned on the rotation table. The rotation table holds three linear stages for a linear position scan and it will be able to turn between 0° to $\pm 25^\circ$ between the magnetic field lines provided by two permanent magnets at the sides. The rotation table is directly connected to the wheel below and the disc plate above. In the third drawing, the disc plate is hidden. According to the design, any position change will affect all components on the PCB. The fourth drawing shows the PCB alignment in a vertical direction. The box allows aligning the PCB in two different positions depending on the channel orientation of an MCP-PMT in the magnetic field.

Complexity is added to the box by the cooling system which has to be designed considering all constraints. Two rigid parts of the PCB have to be cooled down around 18° . The liquid cooling has to be provided in a very safe way without causing leakage. In addition to the rigid parts, the FEASTMP modules have to be cooled. For the EDD, space is much more limited as opposed to the prototype design. The EDD cooling will be designed after testing the prototype.

In Figure 4.21, the cooling system with the corresponding PCB components can be seen. DC driven ventilation systems (fans) are not preferable since they are disturbing the signal by creating electrical noise. Due to that reason, a liquid cooling system with three main components is used: a copper plate which is connected to cooling pipes. The heat pipe is made of copper with a combination of gas and liquid inside. It provides excellent heat conduction. The PCB has 16 hot spots to be cooled down on the inner side. In Figure 4.21, the PCB with the cooling system is shown in 3D. The horizontal pipe represents the tube with circulating cooling liquid inside. It is aligned with a copper plate in a U-shape. In order to reduce risk of any leakage, the U-shaped pipe is the only place where the liquid is flowing. The other shorter pipes are heat pipes that were fixed on the copper plates via blue clamps. The left side is the ASIC PCB with a round shape of the heating pipe. There are three heat pipes with different lengths. The longest heat pipe is bent four times and provides a direct connection on both sides of the ASIC-PCB. On the right side, the visualization of the copper plate is transparent to show the connection of copper plate and PCB. Two heat pipes are implemented at two edges and two FEAST modules are also clamped at the same side of the copper plate. Between the copper plate and the PCB, heat conducting pads are placed to prevent also electrical contact. These pads are elastics and compressible. The PCB will be pressed towards the copper plates, and conducting pads will provide a smooth contact between them.

After testing the PCB in the light-tight box, it will be mounted on the ROM which is one step closer to the phase-1 scenario. Figure 4.22 shows the photocathode of the MCP-PMT surface which will be coupled to the ROM. The arrangement of the cooling system for the tests in magnet box will not fit on the ROM surface. The ROM case has to be re-designed considering the light-tightness and gas-tightness. Besides, the custom-designed PCB with a cooling system has to be stabilized when it is plugged into the ROM. Current scenario in GCS allows to design a ROM case without any spatial constraints. For the phase-1 scenario, a horizontal configuration has to be changed to a vertical rearrange-

4. The Disc DIRC Detector

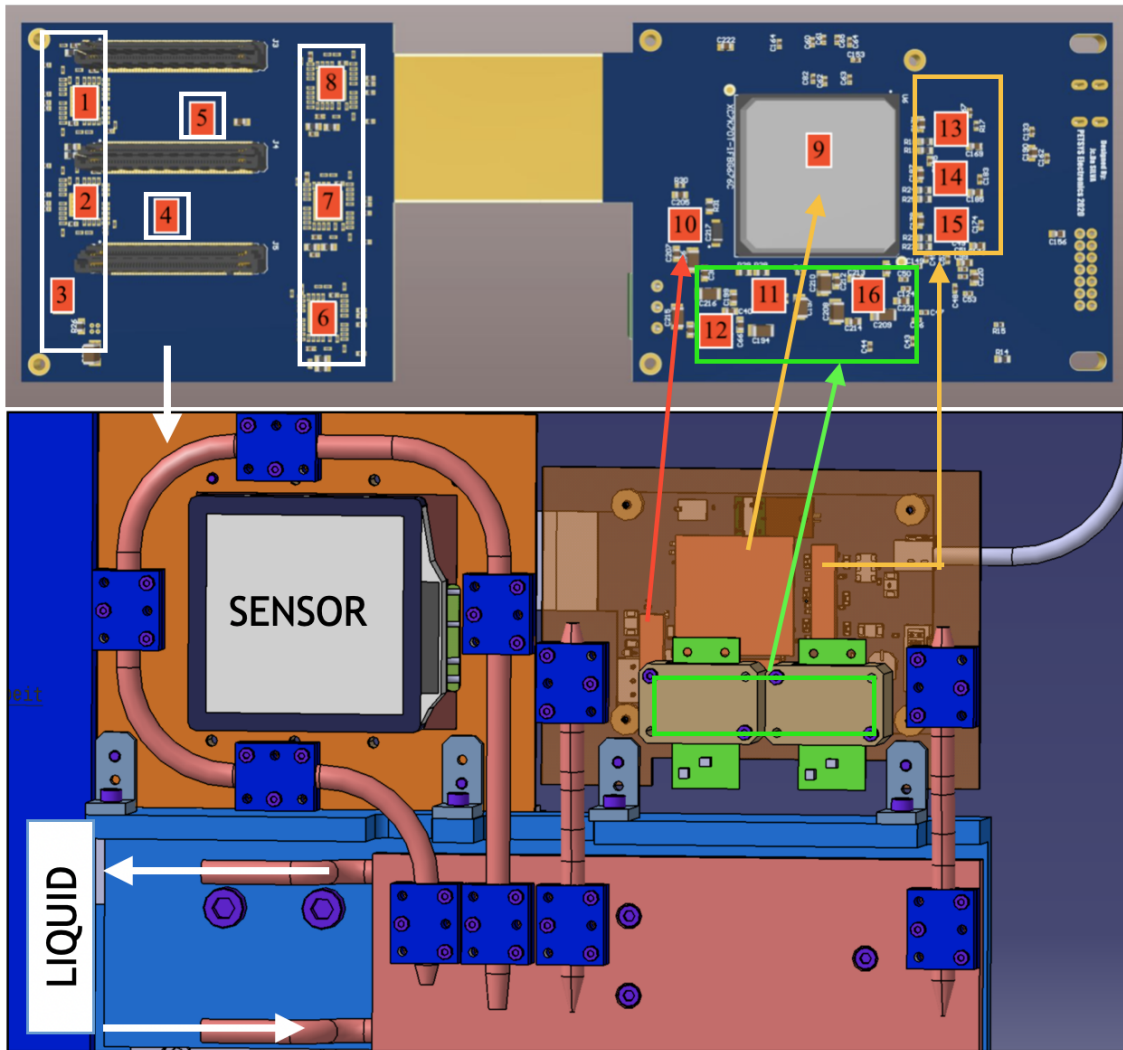


Figure 4.21.: The inner side of the PCB is shown with hot spots pointing to the corresponding cooling items in the bottom 3D drawing designed [Was21].

ment. It can be only done by designing a holding structure to stabilize one quadrant in a vertical position. In Figure 4.22, the designed ROM case with a cooling system is shown for a horizontal configuration. This is a design where light-tightness and gas-tightness are provided. The blue and yellow pipes are the heat pipes which are clamped on the MCP holder (colored as pink). The cooling system will provide the required performance to establish a temperature stabilization for the electronics. To keep optical components dry and clean, gas will be pumped into the middle of the radiator case and will be collected from the outer side of the ROM case. Three different pipe outputs are reserved on the ROM case to decide the best collection performance. The integration between the cus-

4.8. Custom PCB design for the final readout system

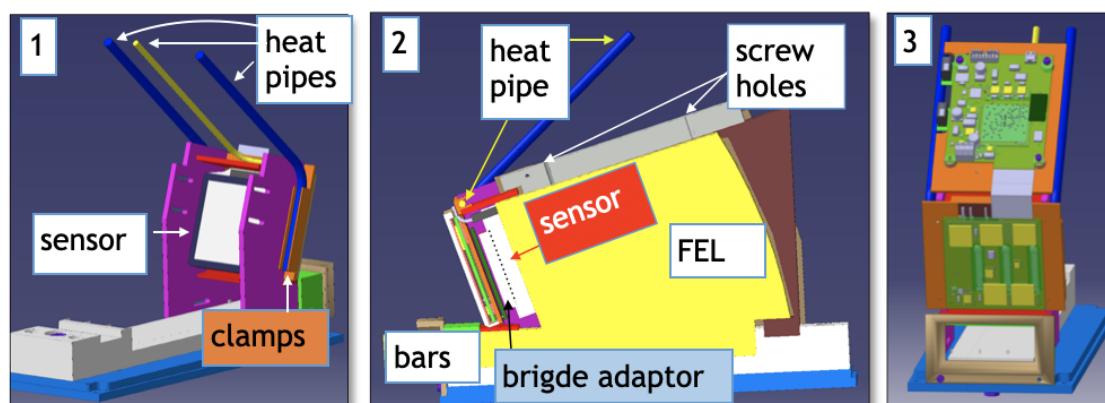


Figure 4.22.: 1: The sensor holder for the ROM case. Two blue heat pipes aligned on the sides, yellow pipe aligned on top. 2: The side view of the ROM case: bars, FELs, adaptor board between the sensor and PCB, heat pipes and two screw holes for stabilization. 3: The front view of the custom design PCB attached to the ROM.

tom design PCB and FEB/D-v2 boards will be done by *mu*HDMI cables connected to the same fan-out-box in parallel. The data stream will be sent to the DAQ board via VTRX+ for custom PCB and via SFP+ connector for the FEB/D-v2 boards. The VTRX+ provides a connector with MT ferrule connectors to connect the MPO via LC connector. Due to that reason, an LC to MPO adaptor is needed in-between. To support the communication, the custom PCB will require flashing the FPGA to change the firmware (developed by PETsys company).

Since two custom design PCB will be delivered, the same number of ROMs will be coupled to the radiator for testing purposes. In addition to two custom design PCBs, the latest version of ASICs and two FEMs will be connected to the third ROM. The sketch of the readout system for phase-1 can be seen in Figure 4.23 with the FEE boards and the DAQ system. The plans are to increase the number of ROMs to 16 for phase-1. The existing DAQ board design with 12 channels of fan-out-box will be used for phase-1 scenario instead of PANDA DAQ and clock & synchronization system. The goal is to study behavior of the custom PCB in a PANDA environment and if any modifications are necessary, apply them for phase-2.

For the phase-2 of PANDA, the FEEs will be used with a dedicated cooling. The EDD will be positioned to the place where the electronics will be exposed to around ≈ 1 T of the solenoid magnetic field. The requirements listed above should be covered perfectly to interface the FEE between the analog signals and the DAQ system of PANDA. The goal is aimed at by adhering to the following intermediate steps. These steps are planned for GCS setup and the preparations for phase-1. In the following chapters, these steps will be detailed. Depending on the results of the tests, the design can be refined for phase-2. The number of FEE-boards depends on the decision of the PANDA collaboration.

4. The Disc DIRC Detector

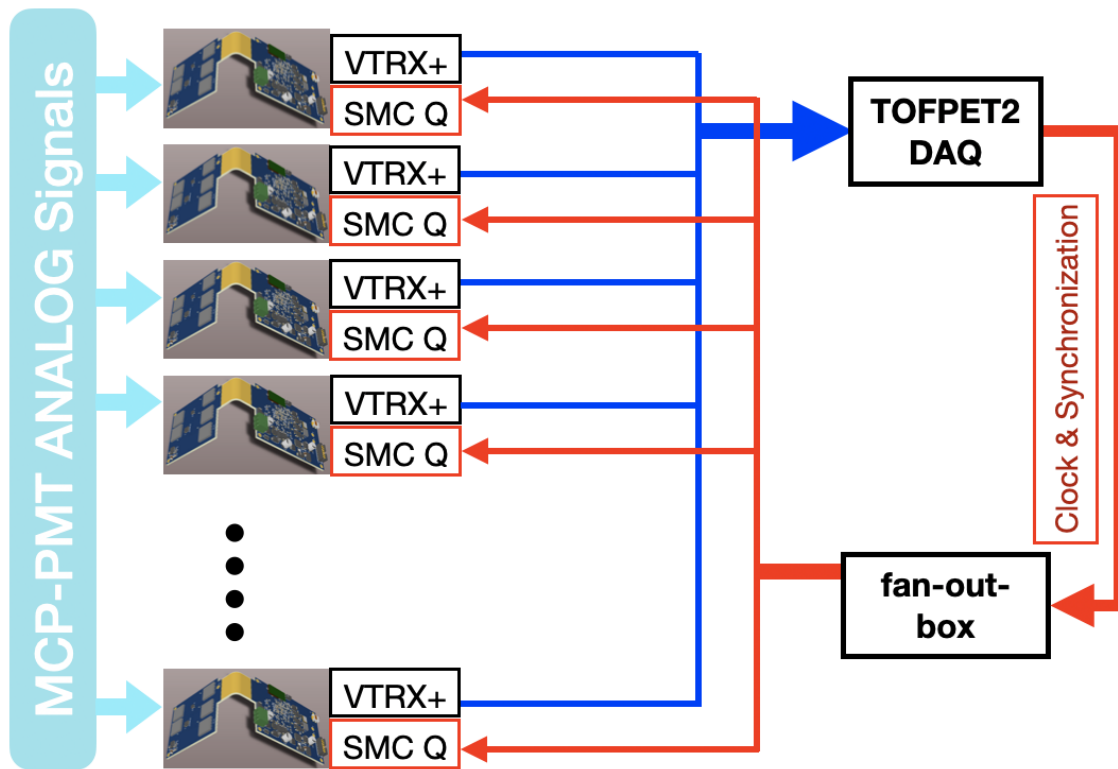
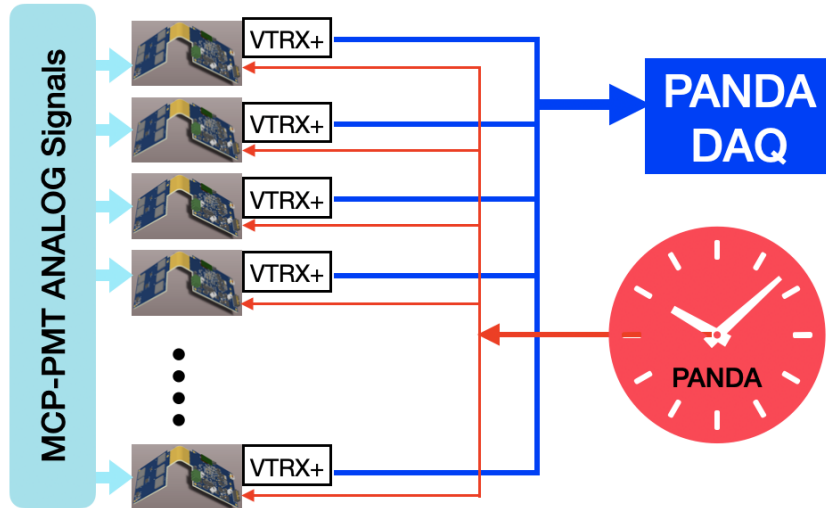


Figure 4.23.: The DAQ system for phase-1 will be the same system that is used for GCS.

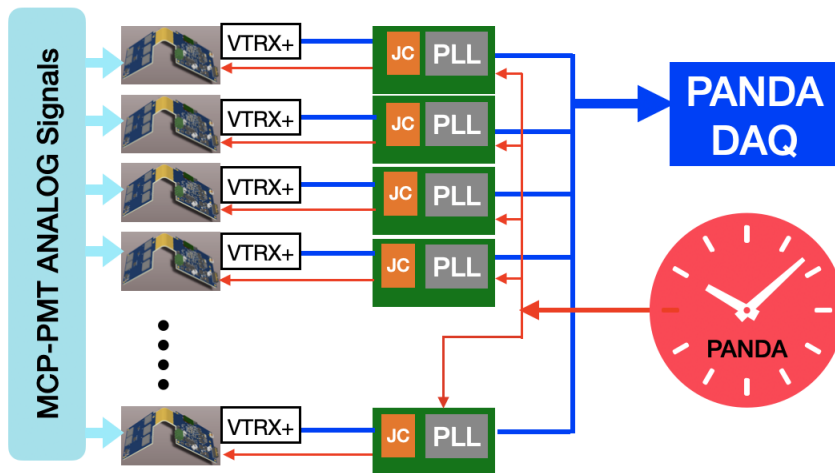
The goal for phase-2 shown in Figure 4.24a is to connect FEE-boards to the DAQ and clock&synchronization system via a bi-directional optical link without any adaptor board inbetween. This type of communication will be checked after testing the custom-design PCB.

In Figure 4.24b, the adaptor board between the so-called intelligent FEE and DAQ system will be used to convert the data format according to the SODANET compatibility and timing format to the custom PCB design. If the timing of the FPGA on custom board is not precise enough, Jitter Cleaner (JC) and PLL methods should be used to provide the communication.

4.8. Custom PCB design for the final readout system



(a) The sketch shows the relation between FEE and DAQ system referring to phase-2 with the assumption of communication without any adaptor board inbetween



(b) The scenario when the adaptor between the intelligent FEE and PANDA DAQ and clock system is necessary.

Figure 4.24.: Two different communication scenarios between the PANDA DAQ system.

5. Giessen Cosmic Station

5.1. Introduction

The GCS allows to check the performance of the EDD prototype with a readout system by using cosmic muons instead of visiting limited test beam facilities at CERN or DESY. Cosmic muons are created by the decay of secondary particles from cosmic rays. Cosmic radiation is coming from different sources such as the sun, solar system, or outer galactic regions, and they consist of high energy protons, nuclei, and other subatomic particles. The energy range of cosmic rays varies from GeV to PeV. When the high-energetic cosmic rays collide with nitrogen or oxygen atoms in the upper earth atmosphere, a shower of secondary particles is triggered. Hadronic showers produce pions and kaons which decay to muons which will be used as a generator for Cherenkov photons in GCS. Neutral pions decay immediately, and charged pions after ($\tau = 26$ ns in their rest frame) to

$$\pi^+ \rightarrow \mu^+ + \nu_\mu \quad (5.1)$$

$$\pi^- \rightarrow \mu^- + \bar{\nu}_\mu \quad (5.2)$$

$$\pi^0 \rightarrow 2\gamma \quad (5.3)$$

Furthermore, kaons decay to muons ($\tau = 12$ ns)

$$K^+ \rightarrow \mu^+ + \nu_\mu \quad (5.4)$$

$$K^- \rightarrow \mu^- + \bar{\nu}_\mu \quad (5.5)$$

In Figure 5.1, the momentum spectrum for cosmic muons are shown for two different angles at sea level. The average lifetime of the muons is $\tau = 2.2\mu\text{s}$ and the expected number of muons per minute per cm^2 is about 1 at sea level [SC00]. When it is calculated for our current quadrant with a surface area of 7792 cm^2 , the expected number of muons are around 130 per second.

In the third drawing of Figure 5.2, all components of the GCS can be seen in detail. The GCS consists of four tracking boxes (see first sketch in Figure 5.2) with 2 layers of scintillating bars with a dimension of $15 \times 10 \times 500\text{ mm}^3$. The aim of grouping two SiPM array boxes is to create a bar grid structure for position determination of muons in 2D. The muon momentum direction will be defined by the second group of tracking boxes which are positioned closer to the radiator. Since the EDD will cover polar angles between 5° and 22° of the PANDA Endcap region, 13° was chosen to displace the second group of the SiPM array box against the first group. Additional $500 \times 500\text{ mm}^2$ trigger

5. Giessen Cosmic Station

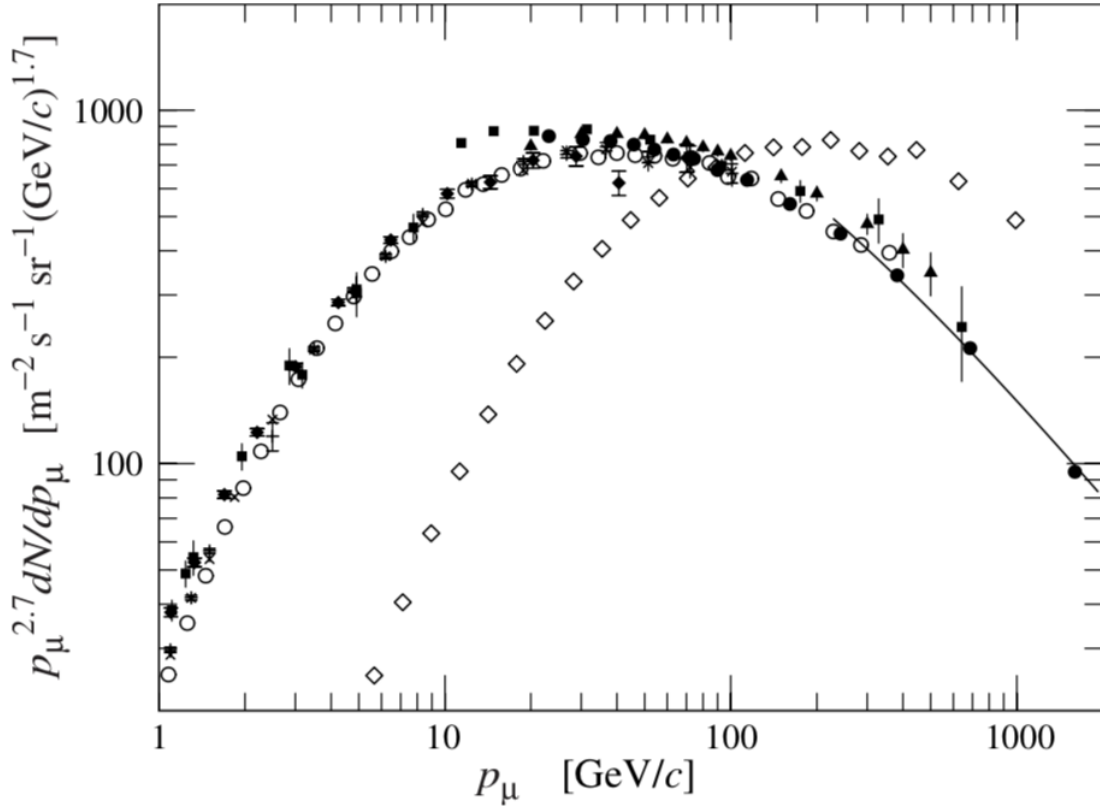


Figure 5.1.: The momentum spectrum of cosmic muons from different experiments when $\theta = 0^\circ$. The shifted distribution to the right is for $\theta = 75^\circ$. The source of the image is [Group16].

scintillator plates with four SiPMs at each corner are positioned above the first tracking box and below the lead absorber. The radiator of the EDD prototype is positioned on the optical table under the fourth tracking box. The lead is positioned above the trigger plate to absorb low energetic muons. The details of the GCS can be found in [BDH⁺20].

In Figure 5.3, the path of a muon is presented with a red arrow. The axis-origin of the coordinate system is determined at the corner of the top trigger plate. The x -axis is pointing towards the page which is perpendicular to the alignment direction of the first SiPM bar matrix. Muons hit the first trigger plate, four tracking boxes, the radiator and the last tracking plate after passing the lead. When the muon traverses the radiator with a speed faster than light in the fused silica, the Cherenkov photons will be emitted. The angle of muons can be reconstructed from the four tracking boxes. The polar angle θ is

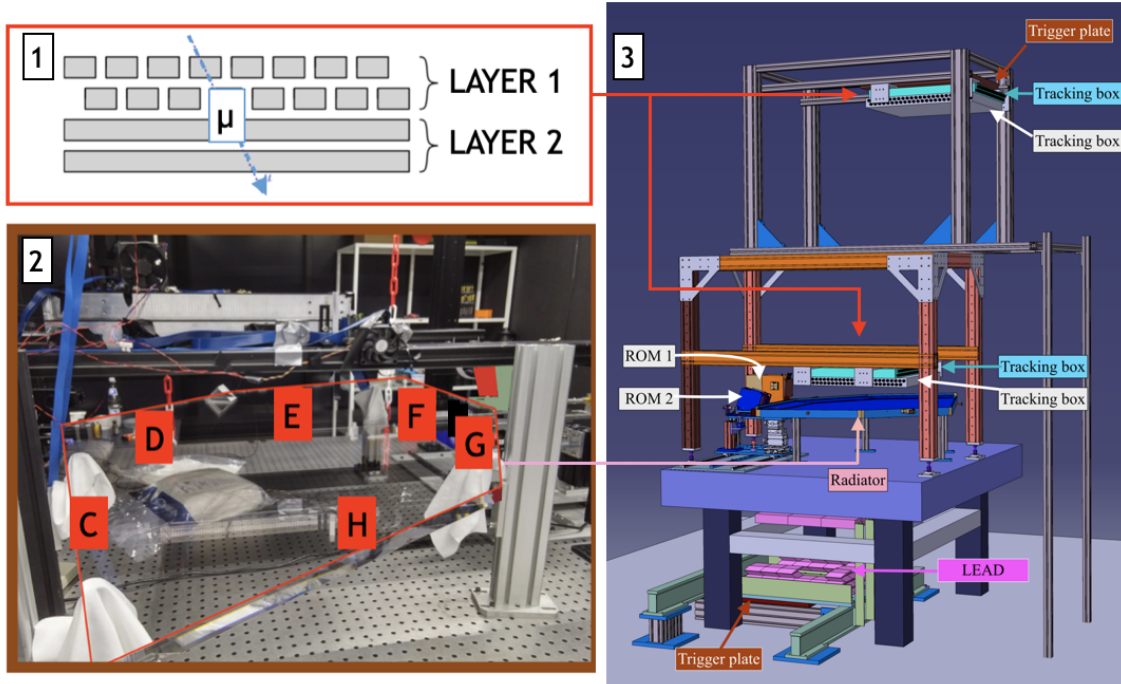


Figure 5.2.: 1: The grid structure of the SiPM layers by aligning them perpendicular each other in two tracking boxes. 2: The full size fused silica radiator plate in the clean-room with the assigned edges. 3: The Giessen Cosmic Station with elements: trigger plates, tracking boxes, radiator and ROMs.

reconstructed according to the axis definition in spherical coordinates:

$$\theta = \text{atan} \frac{\Delta z}{r} = \text{atan} \left(\frac{\Delta z}{\sqrt{(\Delta x)^2 + (\Delta y)^2}} \right). \quad (5.6)$$

The azimuth angle (ϕ) is calculated like this:

$$\phi = \text{atan2}(\Delta y, \Delta x) = \begin{cases} \text{atan} \left(\frac{\Delta y}{\Delta x} \right), & \Delta x > 0 \\ \frac{\pi}{2} \cdot \text{sgn}(y), & \Delta x = 0 \\ \text{atan} \left(\frac{\Delta y}{\Delta x} + \pi \right), & \Delta x < 0 \text{ and } \Delta y \geq 0 \\ \text{atan} \left(\frac{\Delta y}{\Delta x} - \pi \right), & \Delta x < 0 \text{ and } \Delta y < 0 \end{cases} \quad (5.7)$$

Δx is the position difference between the first and the second tracking box in which the particle creates a signal. The same calculation is done for other coordinates to calculate the extrapolated position on the radiator. In order to determine the extrapolated positions

5. Giessen Cosmic Station

on the radiator surface (x_{reco}, y_{reco}) , the linear extrapolation formula is used:

$$x_{reco} = x_{TOP} + \frac{z_{reco} - z_{TOP}}{z_{BOT} - z_{TOP}}(x_{BOT} - x_{TOP}), \quad (5.8)$$

$$y_{reco} = y_{TOP} + \frac{z_{reco} - z_{TOP}}{z_{BOT} - z_{TOP}}(y_{BOT} - y_{TOP}) \quad (5.9)$$

therein BOT denotes the bottom box (position) and TOP denotes the upper box (position).

5.2. Mechanical Components of GCS

Several prototypes of the EDD radiator were developed in different shapes to evaluate the performance of the EDD. The latest prototype was designed in 2016 in a rectangular shape and it was used for the test beam experiments at CERN in 2018. The results of the 2018 test beam will be discussed in chapter 6.

In 2019, a fused silica plate with the dimensions a little bit smaller to the final design of the radiator was produced for test purposes only and delivered by Nikon Company as shown in Figure 5.2 left-bottom. The radiator has some deficiencies and some broken edges along the surfaces of the H and G sides which makes the coupling of the bar impossible. The G side of the radiator is not polished and the shared corner of the H and C is broken. This limits the measurements on the specific sides but does not make measurements on the other sides impossible. According to the plans, a new radiator in high-quality will be obtained till the phase-1 schedule. If this is not the case, then the unpolished side could be polished. The coupling on the sides with little scratches can be improved by using optical grease.

In the GCS 3D scheme presented as the third drawing in Figure 5.2, two ROM-cases were coupled to the F-side of the radiator with (ROM 1) and without (ROM 2) light-tight case. The GCS experiments will have the radiator in a horizontal alignment as shown in Figure 5.2. The radiator has a weight of 50 kg and sharp edges that can be broken easily. Screws are carrying the radiator to provide a safer descend. The ITEM profiles with soft-plastic screws under the optical cleaning tissues are carrying the plate. To start the experiments in a light-tight safe area, the light-tight cases for the optical components were designed since it is quite important to reach a aimed final design for the final EDD as well. The light-tight boxes for the light-sensitive materials such as the radiator and the ROM have been modelled for the GCS experiments in a horizontal alignment. The requirements were determined by considering the experimental factors:

- The GCS-box design should allow to test any side and any position of the radiator surfaces. Due to that reason, a sliding window is used instead of a fixed ROM-position. However, the fixed optimum positions are determined for bar coupling on the broken sides of the radiator.
- The distances between the radiator and the top and bottom case cover plates should be 1 mm which allows testing the gas flow in-between.

5.2. Mechanical Components of GCS

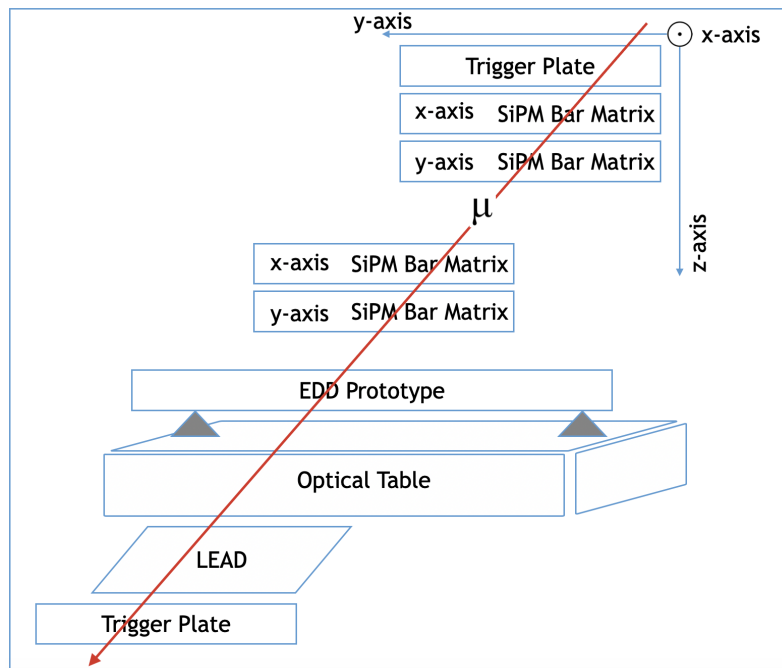


Figure 5.3.: A sketch of the GCS.

- The case should have laser and gas feedthroughs on the D-side which is planned at the same position for the final design as well.
- The alignment of the radiator should be controlled and changed with the help of plastic soft screws to provide a proper plate alignment.
- The ROM boxes can be designed at any scale since there are no mechanical constraints.

The boxes were designed [Was21] and produced at the mechanical workshop of the physics institute in JLU. In Figure 5.4, the 3D drawings of the radiator box from the side view (1), in isometric view (2) of the radiator with ROM box and the ROM box in isometric view (3) can be seen. In the first screenshot of Figure 5.4, the side view of the radiator case and the ROM case is shown. The radiator is shown in grey in the first drawing between two blue cases. The bars and the focusing elements in yellow inside the ROM box are coupled to the radiator. The large screws below the radiator case allow changing the position of the radiator in a vertical direction in a very safe way on the table. That means the soft plastic screws will carry the radiator at the beginning for the mounting procedure. Afterwards, the screws will be driven slowly towards the optical table and the radiator will get closer to the surface of the bottom case. Two extra screws on the edges E and C will provide a finer horizontal alignment. The G-side of the radiator has been completely closed because of its unpolished surface. For the H-surface and F-surface, the sliding window with one opening can be used to define the proper position for the ROM.

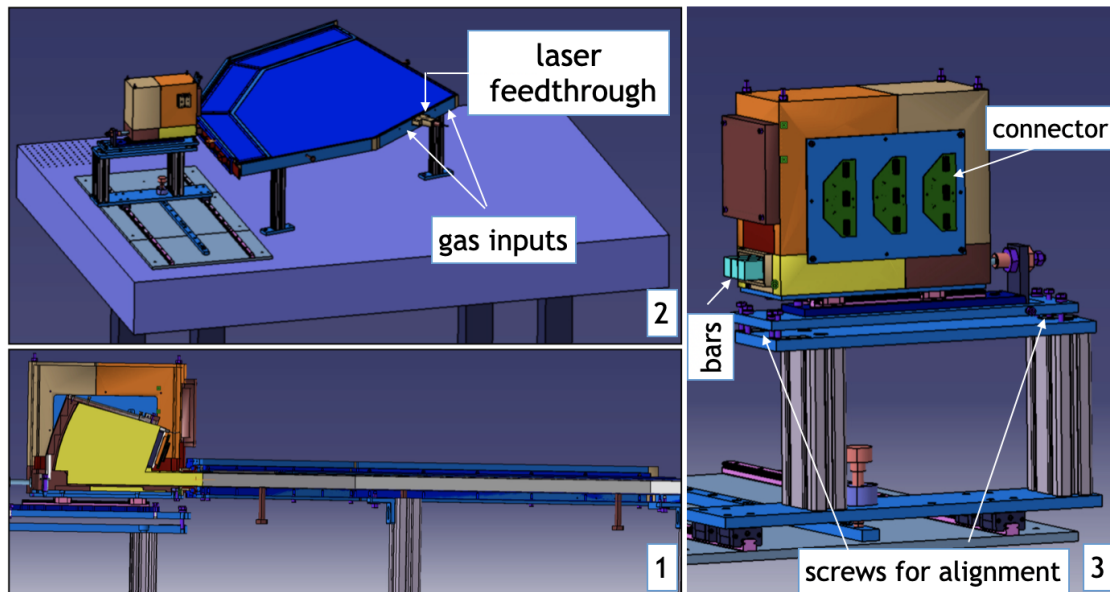


Figure 5.4.: The design of the light-tight cases for the radiator plate and ROMs from the side view [1] and the isometric view [2]. The isometric view of the ROM case [3] [Was21].

To combine the movement of the sliding window with the ROM case, a sliding platform for the ROM case was designed. Since the sliding window is not gas-tight, side plates with fixed openings can be produced after the determination of the final ROM positions. Currently, only three ROMs are available which never cause a spatial constraint for the design of the ROM boxes. They can be designed in a bigger shape compared to the final constructions as a first step. In the second CAD drawing of Figure 5.4, the feedthroughs for one laser input and two gas system inputs can be seen. The top lid of the radiator case has three window openings for checking the alignment of the ROM bars after closing it. In the third drawing in Figure 5.4, the ROM box can be seen from an isometric perspective. The ROM box is positioned on item profiles with sliding rails. With the help of sliding rails, the bars can be coupled to any position of the radiator side surface. The sliding rails can be fixed in a certain position with the help of a screw in the middle of the stage. The alignment of the bars will be arranged and stabilized with the screws shown in the third drawing of Figure 5.4. They provide a finer vertical and horizontal alignment. The right side of the radiator box is reserved for the connectors of the readout system between MCP-PMT and the ASICs. Depending on the sensor type, this part can be changed for the proper connection. The brown part of the front side has an offset value from the surface with the assumption of bending the custom design PCB. The backside of the ROM box contains a strong spring to push the ROM case towards the radiator side in order to achieve a high quality of optical coupling.

The light-tight boxes were successfully produced as shown in Figure 5.5. The upper

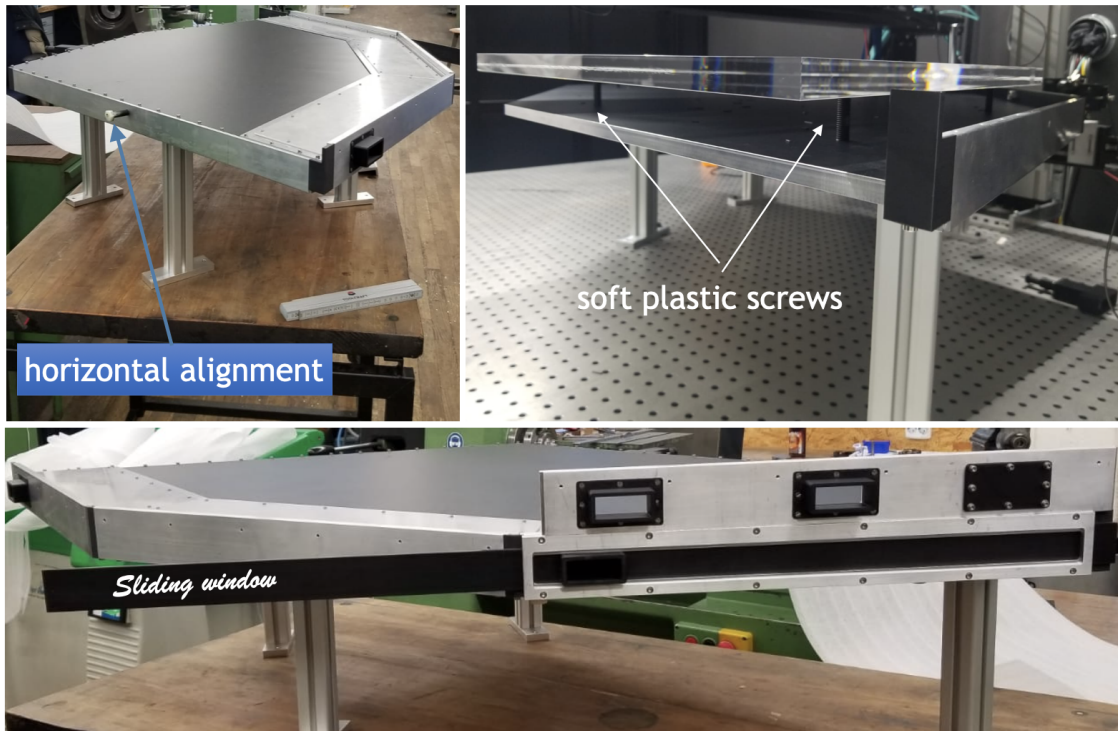


Figure 5.5.: Three different photos of the radiator case. The upper left one shows the plastic screw for finer horizontal alignment. The upper right photo shows the radiator placed on the soft plastic screws. Lower photo shows the sliding window, and fixed position of the side plate for an example.

left photo shows the closed structure. The plastic screw is positioned at the C-surface for aligning the radiator horizontally. The upper right photo shows the radiator positioned on the screws in the cleanroom. The sliding window can be seen in the bottom photo with one opening. The plate with three fixed positions is also shown as an example. The unused window can be closed light-tight as shown for the third opening.

5.2.1. GCS construction

The readout system for the 2018 prototype is explained in chapter 6. In this chapter, the readout system of the existing GCS and the custom design PCB for phase-1 will be discussed.

In order to provide one EDD quadrant for phase-1 of the \bar{P} ANDA project, it was planned to start commissioning it in a horizontal alignment with one ROM in the beginning. After the performance tests of the prototype, the orientation will be changed vertically. As a first step, the five-sided quadrant is integrated with a light-tight case into the GCS setup. The runs were planned to start with one ROM and planned to be upgraded to a higher number of ROMs after confirming the performance at every step.

5. Giessen Cosmic Station

Before connecting the anodes of MCP-PMT to the recent production batch of the ASICs, the performance tests are planned with both positive and negative polarities provided from a pulser signal.

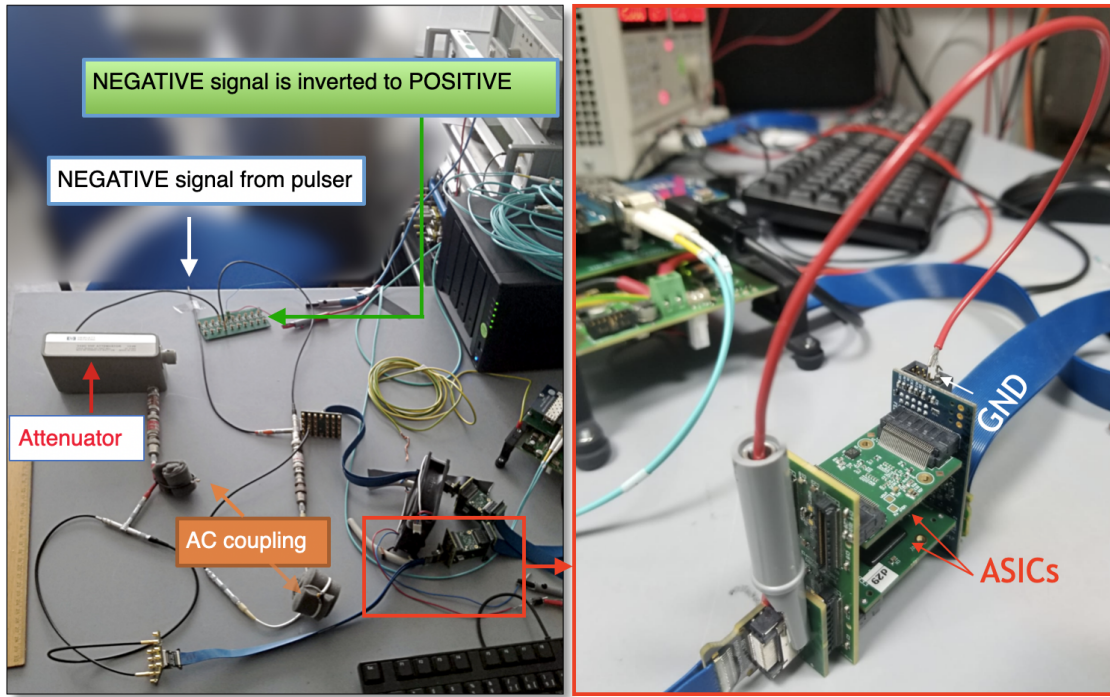


Figure 5.6.: Left: The test setup of the recent production of the ASICs. The negative signals from the pulser are provided Right: One FEM128 board with two ASICs facing to each other. The red cable shows the ground connection between the cable and FEM128 board.

On the left side in Figure 5.6, the test setup of the ASICs is shown with two different input signal polarities. The pulser provides a negatively polarized signal that is split into two signal cables. One signal source is shown in Figure 5.7 compared with the MCP-PMT anode signal. The pulser signal is shaped like an MCP-PMT signal with an amplitude 60 mV and less than 5 ns pulse width. The second signal source is inverted to a positive signal. The signals are AC coupled to the ASICs. By setting the global parameter of the ASIC depending on the input polarity, the input voltage offset is $V_{IN} = 800$ mV for positive and $V_{IN} = 400$ mV for negative signal. The performance of the ASICs with mixed polarity signals was confirmed by evaluating the data processing corresponding to different pulser signal frequencies. During the tests, some background noise were detected with an amplitude ≈ 40 mV. In order to get rid of possible ground loops, the grounds of all devices were connected to one common ground which was not enough to eliminate the ground loop between the ASICs and the signal input. The right photo in Figure 5.6 shows the ground equalization of the ASICs and input signal by added red cable. The

input cable from the left side of the ASICs carries 32 signal lines with 8 power lines for the SiPMs. It does not carry any ground connection to the ASIC which causes a ground problem between the FEM128 board and the cable. This could be solved by the added cable in Figure 5.6.

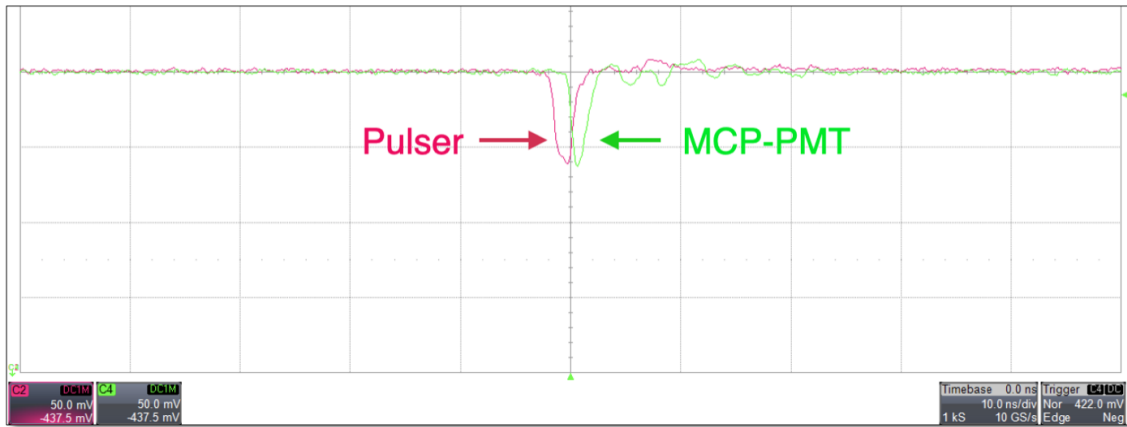


Figure 5.7.: The MCP-PMT signal (green) and pulser signal (purple).

After confirming the performance of the ASICs, they were connected to the MCP-PMT anodes. In the first photo of Figure 5.8, the coupling between the bars and the side of the radiator is shown inside the red circle. Since the ROM case is open, the blue coaxial cables of Samtec connected to the MCP-PMT anodes are also visible. There are line-shaped plastic material with 1 mm thickness between the radiator and the case. Before a complete descend of the radiator, soft plastic chips with 1 mm thickness were distributed homogeneously on the surface to provide 1 mm distance from the radiator. There is a possibility of having an undesirable slight bend of the case lid towards to radiator. In case of any contact between the radiator and the lid, the reflection inside the radiator may change and cause a different polarization. This can be prevented using the same dot-shaped plastic materials by distributing them on the surface of the radiator. Therefore, any possible undesirable situation can be prevented by a homogeneous distribution of the plastic materials. This way, additional space is needed for two different reasons, one is the gas flow to clean the optical surface and the other is to distribute the pressure.

The second photo in Figure 5.8 shows the complete setup including the light-tight cases. Two yellow circles highlight the fans as an initial step of the cooling system. The working temperature of the electronics should be stabilized around 18°C. Moreover, the fans were able to provide to cool the ASICs down to almost room temperature (22°C). In order to stabilize the temperature of the ASICs around 18°C and avoiding high-frequency noise due to the fans, the fans were replaced by liquid cooling. The liquid is a mixture of 80 % of distilled water and 20 % of ethanol in the volume of a Huber chiller device. The device is used for distributing the liquid around 8°C and collecting liquid back around 23°C maximum. In the third photo, the first FEM128 board with the cooling pipes is shown. The temperature reaches 16°C which is located at 4 m distance from the Huber

5. Giessen Cosmic Station

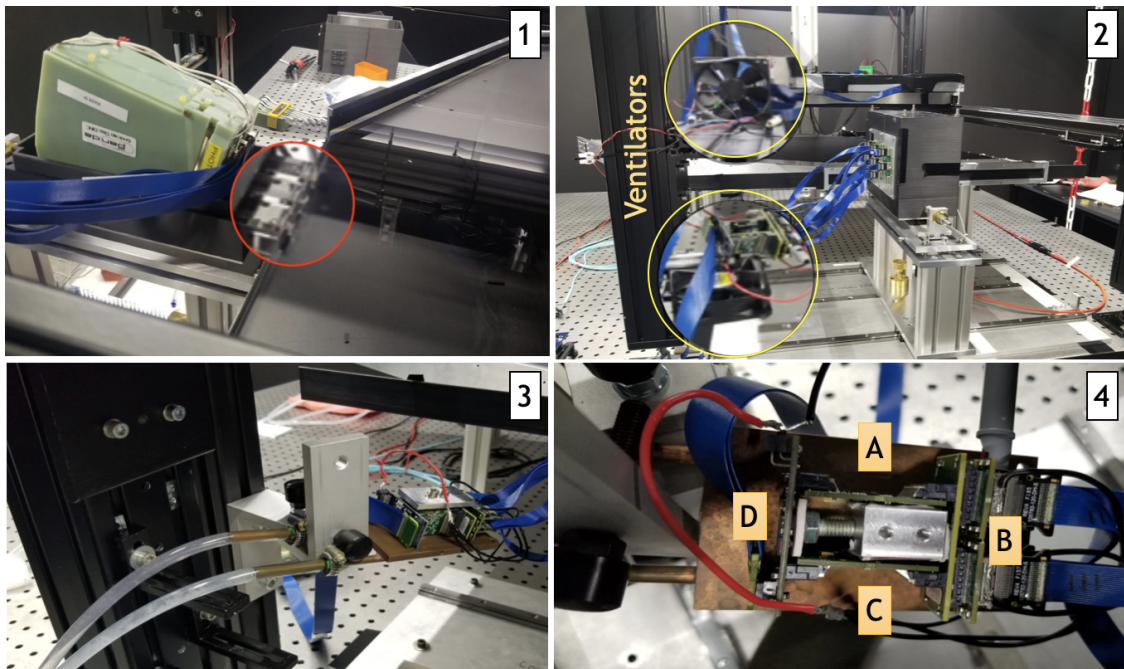


Figure 5.8.: 1: One ROM is coupled to the edge of the radiator. The red circle shows the coupling between the bars and the radiator. The soft materials provide a distance between the bottom lid and the radiator. 2: The perspective is from the back side of the radiator. Blue Samtec cables from the side of the radiator case carries analog signal from the MCP-PMT pins and reach FEMs. The FEMs are cooled with fans. The red cable from the right side provides high-voltage (2250 V) for the sensor. 3: The cooling system was changed to liquid-based system. This element is 4 m far away from the Huber cooling device. Liquid enters the copper plate from the right copper pipe, travels through the U-shaped copper pipe soldered to the copper plate, and leaves from the left side. 4: The top view of the plate. The sides of A,B,C, and D have a thermal pad to provide a thermal connection.

device. The pipes of the cooling system are attached to U-shaped pipe of the copper plate. The fourth photo shows the top view of the cooled surfaces. The copper plate has an additional part in the middle which touches the surface of the ASICs. The surfaces named A, B, C and D are touching the thermal pad with thermal conductivity of 8 W/mK . The thermal pad provides great heat conductivity with durability in the long term of measurement. The red cable and black cables are the grounding cables between the analog signals and the readout system. The analog signals are connected to the B-side of the FEM128 module. The cable from the D-side is connected to the FPGA-board (FEBD-v2). The cooling system was reliable enough to cool down the whole system permanently.

5.3. GCS readout system

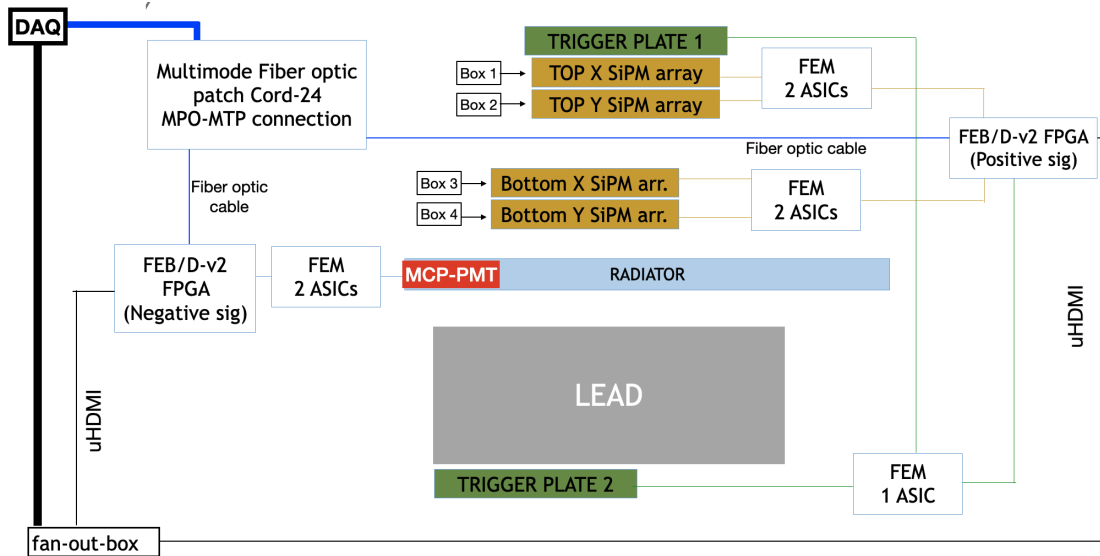


Figure 5.9.: The readout scheme of the GCS.

The readout system of the GCS works with a mixed-signal polarization. In Figure 5.9, the existing readout scheme of the GCS can be seen. There are four tracking boxes and two trigger plates that provide a positive signal polarity to the second FEBD-v2 board. The MCP-PMT signals are connected to the first FEBD-v2 board with two ASICs. In total 9 ASICs are used and each ASIC is assigned to the required polarity by modifying the code of the DAQ system. Depending on the assigned mission of the ASIC, each channel has an input voltage offset $V_{IN} = 800 \text{ mV}$ for positive and $V_{IN} = 400 \text{ mV}$ for negative signal polarity separately. The tracking boxes and the trigger plates are placed in a 3 m distance relative to each other. Due to that reason, longer cables are used to connect all of them into one FEBD-v2 board. This was done with a hardware change to provide enough power for transmitting the signals via longer cables.

The FEBD-v2 boards utilize two different connection types for data transmission and synchronization. The synchronization of the FEBD-v2 boards is operated via μ HDMI cable connected to a fan-out box. The fan-out-box has 12 HDMI outputs that get the synchronization signal from the DAQ board inside the PCB. The data transmission from the FEB/D-v2 boards to the DAQ board is accomplished via optical cables from SFP+ cages. The optical cable connection contains an MPO to MTP connector. Depending on the connection port of the fiber optic cable, the system automatically determines the order of the FEB/D-v2 board. In order to provide data transmission with an optical cable, the firmware of the FPGA was flashed via a JTAG connector. The existing board with ferromagnetic parts such as DC-DC converters or SFP+ cage connectors can be used since there is no magnetic field. These parts have to be changed for the final EDD.

Two FEB/D-v2 boards were prepared to acquire data synchronously. Before the data

5. Giessen Cosmic Station

acquisition, the threshold, time-over-threshold (ToT), and the integration (QDC) (charge-to-) calibrations were performed. Then, the proper thresholds were set for each ASIC channel.

5.4. Results of the GCS Data Analysis

The goal of integrating the radiator into the GCS was to check the performance of the EDD prototype and the connected readout system in combination with the signals from an MCP-PMT and the SiPMs. The data acquisition has been started in the last quarter of 2020 with PHOTONIS XP85132-S-MD3 which was used for the test beam experiments. At the beginning of 2021, the MCP-PMT was replaced with PHOTONIS ES440. After the hardware change, the readout system was re-calibrated and the threshold values were set according to the new setup. Every hardware change requires a new calibration. Even without hardware change, it is crucial to check the data rate for the channels constantly. Because the detected number of events is getting larger for some channels for unknown reasons. Depending on the outcome of the runs, the new thresholds settings with or without calibration are decisive. Furthermore, a re-calibration together with a check of threshold settings was performed from time to time.

The data output of the TOFPET2 is in a raw data format which is available as in different data formats. It was chosen as a ROOT file format which creates a hierarchical structure of a ROOT-tree with *leaves* containing information of the time, channel, ToT or QDC. The script for converting the raw data into a root format has been modified (see chapter 6) to obtain fully time-ordered records.

The collected data from PHOTONIS ES440 was analyzed using a self-written C++ analysis code in the ROOT framework. The logic of the analysis code is based on creating event loops. Every event is defined as a group of many hits when the time difference between consecutive hits are less than 100 ns. There is always a minimum of 100 ns time difference between events. Time slot of 100 ns was chosen on a purpose considering the reasonable delay between the signals due to the length of the cables or digitization. Then, event groups were analyzed independently by applying common selection criteria to reconstruct Cherenkov angles of muons. The criteria are based on getting a signal from every tracking plane to reconstruct the average position of the muons and to count the hits in MCP-PMT. The position information is used to calculate the extrapolated position of muons in the radiator. Using the hit position and the orientation of the radiator, the Cherenkov angle of the muons is reconstructed.

5.4.1. Performance of the SiPM Boxes

The reliability of the tracking boxes were tested by checking the constant behaviour of data rate. As a first step, the distributions of specific polar angle and azimuth angle are plotted. They are used to determine the position of the muons which hit the bar in the tracking box. The bar number is converted into the position of the chosen coordinate

system. According to the axis definition, the exact position of muon hits on the radiator can be extrapolated according to the formulas (5.8) and (5.9).

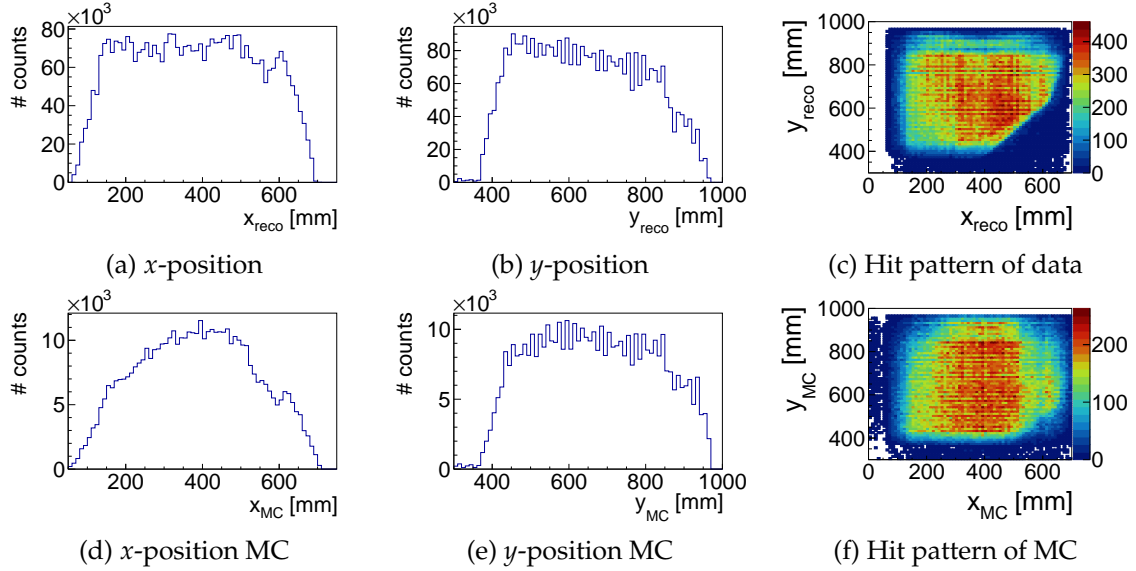


Figure 5.10.: Upper plots: The reconstructed positions of the muon hits on the radiator from the collected data. Bottom plots: The reconstructed position of the muons from generated GEANT4-MC results. The hits are plotted if there is a coincidence with at least one Cherenkov hit.

The position of muon hits on the radiator is reconstructed with a maximum of two and a minimum of one hit in each SiPM box. There are two layers in every SiPM box that is the reason of limiting two hits in each SiPM box. Figure 5.10a and Figure 5.10b show the distribution of the muons in x and y position independent from an MCP-PMT hit from data. Figure 5.10d and 5.10e show position distribution of MC. The extrapolated position on the radiator is plotted only if there are also MCP-PMT hits. The results for measured data and MC are compared to check the performance of the tracking boxes. The upper plots in Figure 5.10 show the reconstructed data, the bottom plots show the MC results. The distribution of x -position is expected to have in a horizontal shape which is not the case for values $x > 550$ mm in Figure 5.10a and Figure 5.10d neither data nor MC and data. In Figure 5.10b and Figure 5.10e, the distribution counts slightly drop for increasing y values. This is expected since the bottom group of boxes are shifted in 13° compared to the upper group of boxes. This shift results in less contribution of increasing y values. Furthermore, a drastic drop is visible for the position at $y = 850$ mm. The reason for such drops in one-dimensional distributions for $y = 850$ mm and $x = 550$ mm are the exclusion of specific bars from specific SiPM boxes which will be discussed in details. Two dimensional plot in Figure 5.10c and Figure 5.10f show the hit frequency on the radiator which conditioned on MCP-PMT hits. There are some spots have a higher hit rate and the diagonal plate border is recognizable for data and MC. The border represents

5. Giessen Cosmic Station

the D-side of the radiator. The sharp contrast in data is visible only hits in the radiator. However, the contrast for MC is not as clear as for the data. Some things are not fully understood in MC and this feature of the MC is under investigation.

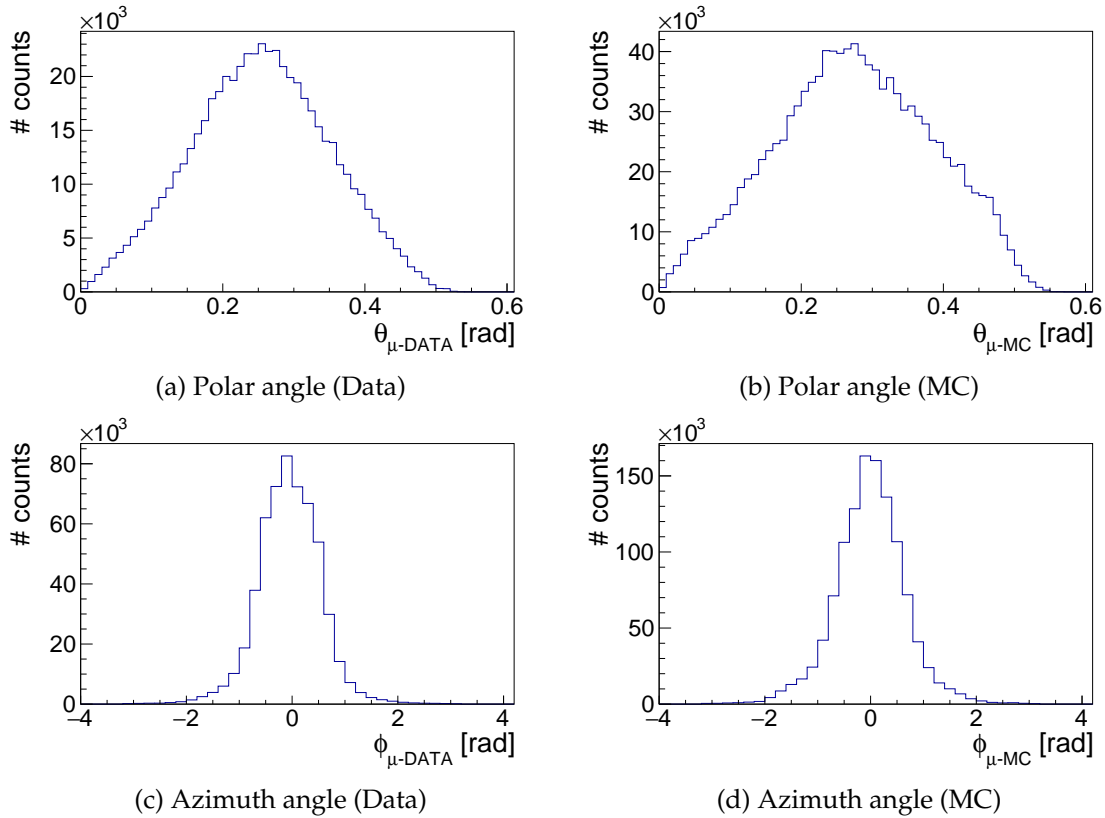


Figure 5.11.: The polar and azimuth angle distribution of data and MC for four fold coincidence from tracking boxes.

In Figure 5.11, the distribution of the reconstructed angles with MC comparisons are shown. The azimuth and polar angle are calculated according to the formula (5.7) and (5.6), respectively. The required Δx and Δy were calculated by differentiating the position information of the hit-assigned bar numbers in different boxes. The Δz is the position difference of the vertical axis between the bars. The count statistics are conditioned on MCP-PMT channel hits. This means that a muon with one angle may induce several channel hits of the MCP-PMT. In Figure 5.11a, the expected polar angle θ of muons is centered around 0.22 rad since the bottom group of the SiPM bar matrix is displaced 13° against to the upper group. The MC distribution of θ angle is shown in Figure 5.11b. The distribution between MC and data shows a small difference. The azimuth angle φ of muons is expected to be distributed around 0 rad which is confirmed by the distribution of reconstructed angles. The reconstructed angle distributions confirm the expectation. Moreover, the MC and reconstructed data from GCS show an excellent agreement.

5.4.2. The Performance of Radiator

In an ideal system, the hits in the tracking boxes are expected to reach before the hits from the radiator. However, the cable lengths or any delay caused by the readout system may change the ordering of the detected signal. In order to check the correlation between the MCP-PMT and the closest tracking box, related time difference plots are shown in Figure 5.12. Figure 5.12a shows the time difference between the closest tracking box and the MCP-PMT for each channel. The color-axis represents the coincidence in the distribution. The plot is highly dominated by repeating vertical patterns. The projection of noise in x -axis is shown in Figure 5.12b (right). To find the reason of noise, the plots of the reconstructed position are plotted for each MCP-PMT channel. The goal is to track back the hit position on the radiator to investigate if the contribution is coming from the whole surface or from a specific position.

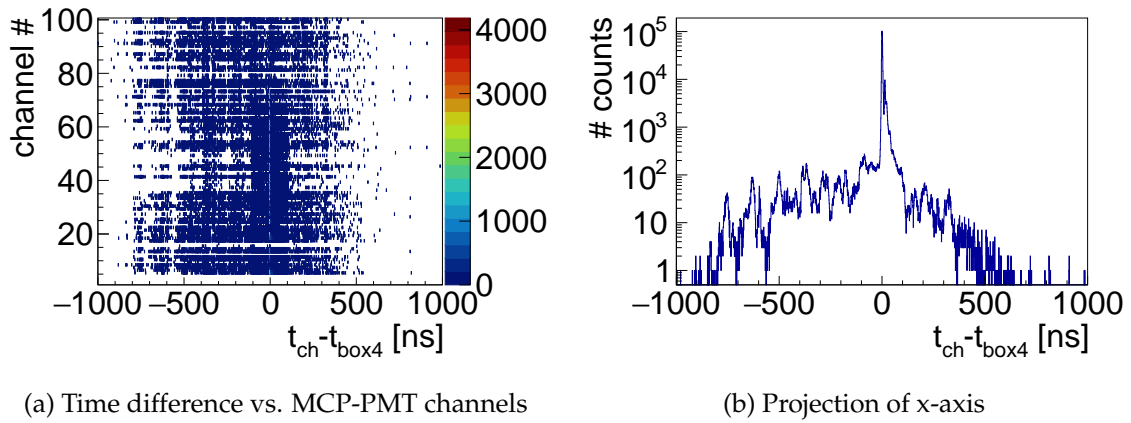
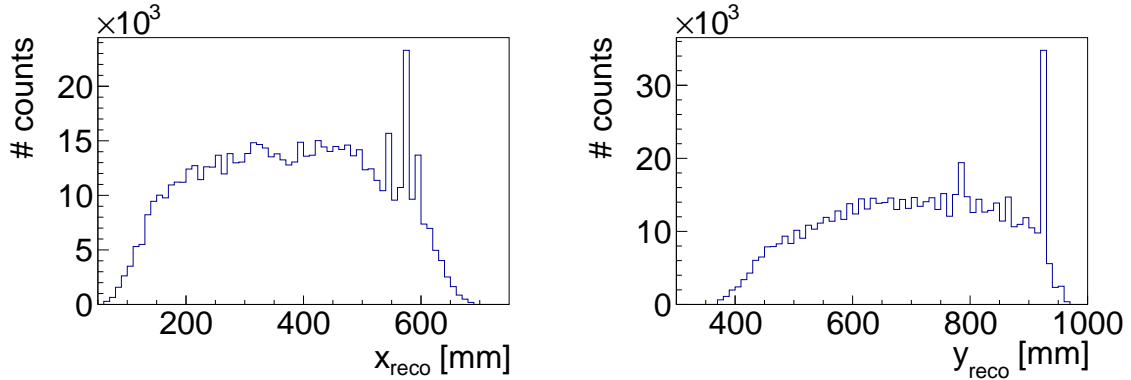


Figure 5.12.: Time difference between MCP-PMT channels and closest tracking box-4. The right plot shows the projection of x -axis of the left plot. There is noise in the shape of the vertical repeating patterns.

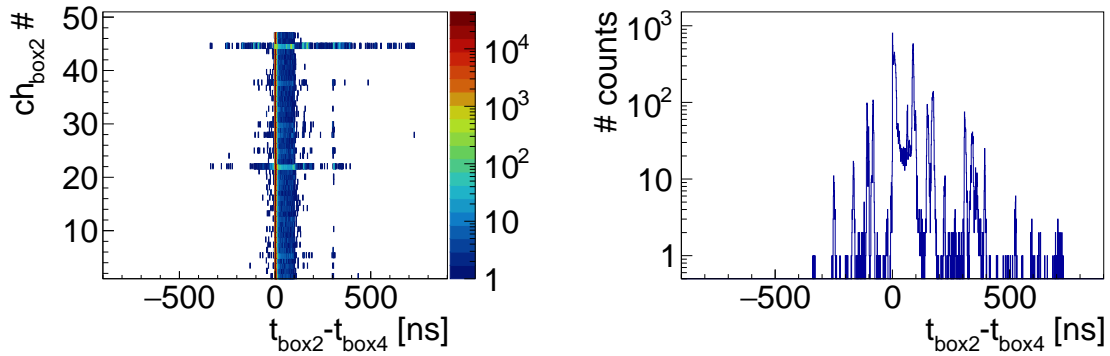
In Figure 5.13, the reconstructed hit positions on the radiator are shown under the condition of any correlation with MCP-PMT hit. The positions $x > 500$ mm in Figure 5.13a and $y > 900$ mm dominate the distribution. The performance of the tracking boxes was evaluated independently from the MCP-PMT. However, the minor influence of defective bars may not be visible in the plots of angle reconstructions. Due to that reason, the time difference between the bars is shown in Figure 5.14 independent from the MCP-PMT hits. The region of best coincidence is shown by a red vertical line. However, two bars show a continuous time difference between -300 ns and 900 ns (see Figure 5.14a). To have a better understanding of timing for the channel 45, a projection is shown in Figure 5.14b. This indicates that the timing for channel 45 is not working properly. That requires a hardware and a software check to understand the reason. There are a few bars in every tracking boxes are detected with similar behaviour. Their time difference plots can be found in the appendix A.

5. Giessen Cosmic Station



(a) Reconstructed x -position of the muon hits for all MCP-PMT channels. (b) Reconstructed y -position of the muon hits for all MCP-PMT channels.

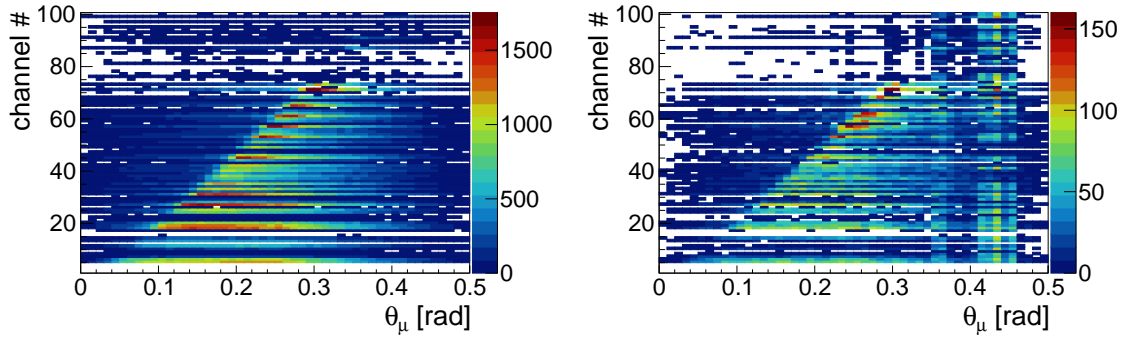
Figure 5.13.: Hit count distributions for x and y showing positions with excessive activities.



(a) Time difference between the box two and channel four for channel numbers in box two. (b) The time difference of fourth box and channel 45 in box two.

Figure 5.14.: Time difference between the two boxes independent from MCP-PMT hits. Two bars in box two timing create noise which is shown in right plot as a projection of channel 45 from the left plot.

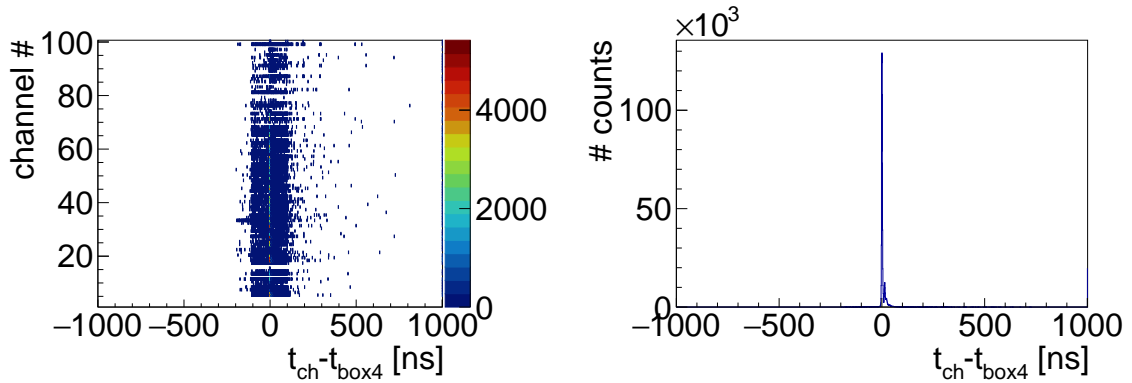
To check the system capability of detecting Cherenkov light, the characteristic Cherenkov photon patterns are plotted as a function of the muon polar angle and their hit positions on the radiator. After reconstructing the polar angles using the SiPM matrix array, two characteristics of Cherenkov photon patterns are compared with all bars implemented and excluding the bars with timing failure. In Figure 5.15, Cherenkov photons are reconstructed as a function of the calculated polar angle and MCP-PMT channels. The MCP-PMT channels are further mapped to the ASIC channels. Some channels could not be calibrated properly and appear as white lines. There are many possible reasons that



(a) Data analysis by excluding the bars with timing-failure. (b) Data analysis is available by using all tracking bars.

Figure 5.15.: Cherenkov photons were reconstructed as a function of the polar angle θ and channels of MCP-PMT.

could explain this behavior, such as improper connections of MCP-PMT pins, permanent defect inside MCP-PMT or a leakage current from MCP-PMT voltage through the ASIC pins etc. In Figure 5.15a, the pattern is reconstructed by excluding the specific bars. In Figure 5.15b, the same pattern was reconstructed including all bars. There are some vertical patterns that dominate the distribution for specific polar angles.



(a) Time difference between MCP-PMT channels and tracking box-4 vs corresponding MCP-PMT channel. (b) Time difference between MCP-PMT channels and tracking box-4. The y -axis represents counts.

Figure 5.16.: These plots were created in the same way of Figure 5.12 with all bars implemented. The difference is that the bars with bad timing behaviour were excluded for these plots which caused the repeating patterns.

The analysis of data is done by excluding the problematic bars. As a result, the plot in Figure 5.12 is shown without the repeating patterns in Figure 5.16. The x -projection of

5. Giessen Cosmic Station

the plot is visible in Figure 5.16b.

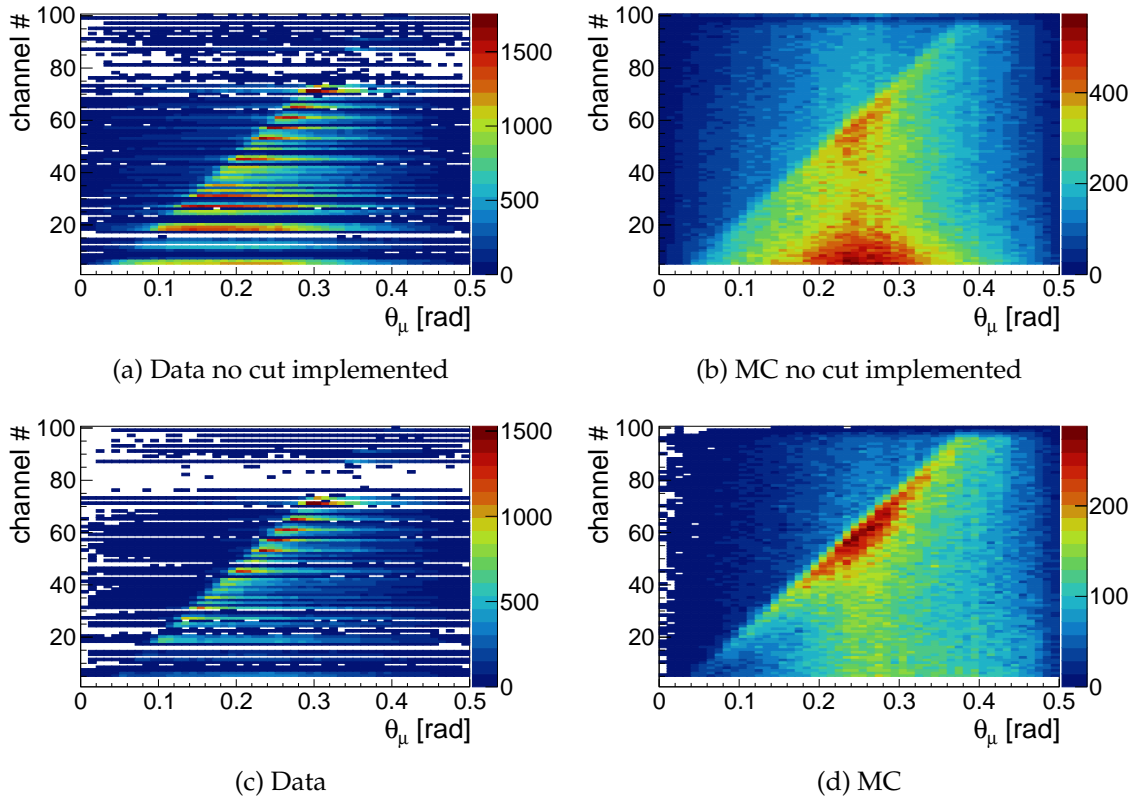


Figure 5.17.: Characteristic Cherenkov photon patterns as a function of polar angle. For upper two plots, no cuts on data and MC were implemented. For the bottom plots, the cuts on azimuth angle and time were implemented $|t_{ch} - t_{box4}| < 5 \text{ ns}$, $|\phi| < 0.5 \text{ rad}$.

After excluding the specific bars in every box, the diagonal pattern of the Cherenkov photons was reconstructed as a function of polar angle θ_μ and MCP-PMT channels in Figure 5.17. With an increasing polar angle, the hit pattern shifts to other MCP-PMT channels. The plots in Figure 5.17a and MC in Figure 5.17b are compared without applying any angle and time cuts. The measured data shows a comparably clean diagonal pattern. Some channels of the MCP-PMT have larger amount of hits compared the rest as shown by color-axis. The MC results are obtained by applying the same analysis steps. There is a bump around 0.2 rad to 0.3 rad for channel numbers from 0 to 20 in the MC and for channel number between 20 and 30 in data. These bumps disappear when additional angle and timing cuts are implemented as shown in Figure 5.17d and Figure 5.17c. The time difference between the tracking box-4 and the MCP-PMT channels were less than 5 ns and the angle $|\phi|$ is less than 0.5 rad for the plots. By applying cuts on ϕ and the time difference, the presented horizontal pattern disappears in data. For MC, the reflec-

tion disappears and very clean diagonal pattern is detectable. The reason for having the region with the highest amount of coincidences between 0.2 rad and 0.3 rad is that the angle of the second group of tracking boxes are shifted to get a predetermined angle which equals 13° . Further diagonal plots can be found in appendix A in Figure A.3.

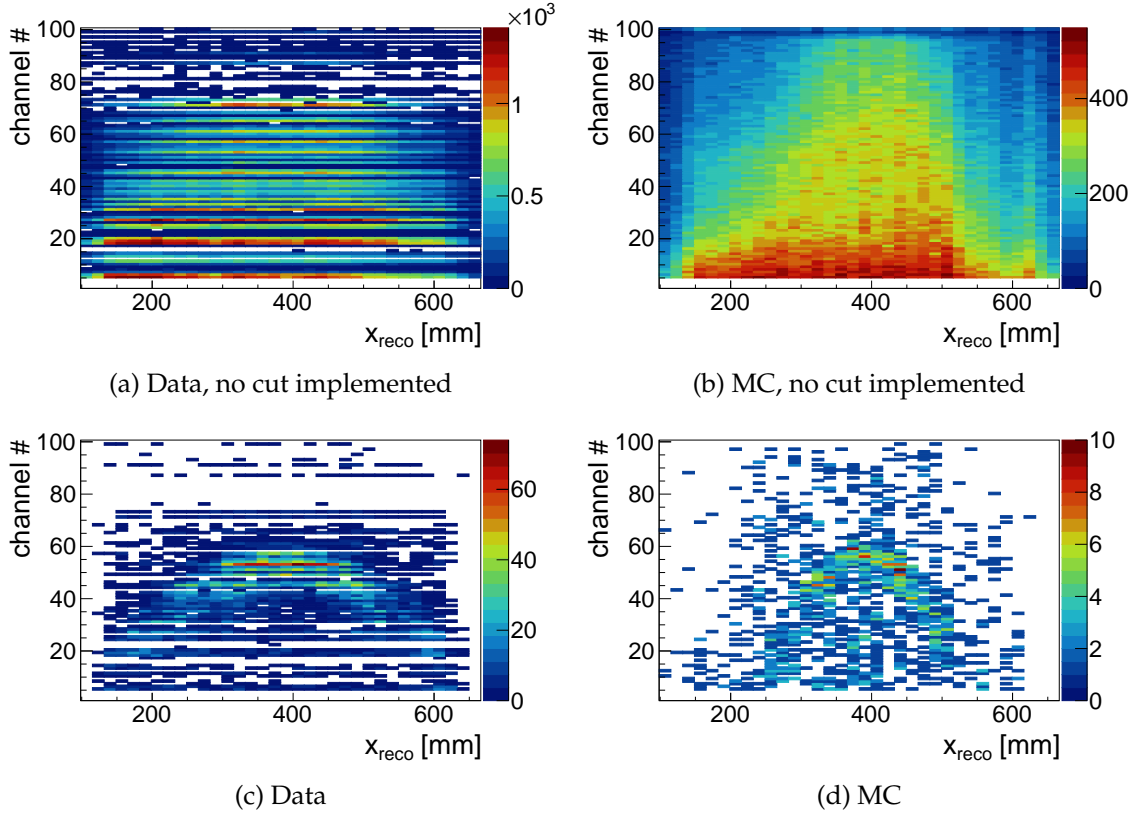


Figure 5.18.: Preliminary results of Cherenkov smiles for data (left) and MC (right). Upper plots without any cut and bottom ones show pattern with the cuts $|t_{ch} - t_{box4}| < 5 \text{ ns}$, $|\phi| < 0.4 \text{ rad}$, $12^\circ < \theta < 14^\circ$ applied.

The other characteristic pattern is the projection of Cherenkov photons on the sensor as a function of the reconstructed x position. Figure 5.18 shows the pattern with the cuts $|t_{ch} - t_{box4}| < 5 \text{ ns}$, $|\phi| < 0.4 \text{ rad}$, $12^\circ < \theta < 14^\circ$. To obtain a more a thinner "Cherenkov smile", the low energetic muons should be selected by using the bottom trigger plate which is positioned under the lead absorber. Due to the unusually small number of statistics in data with unreliable signals from bottom trigger plate, the energy cut could not be implemented in this study. Only MC results with energy cut will be shown.

Figure 5.18 shows comparison between data and MC. When no cut is implemented, the upper plots were obtained without any non obvious concave shape. To reduce the background for obtaining a clearer signal, the specific cuts were implemented such as selecting the most coincidence region which is between 0.2 rad and 0.3 rad corresponding

5. Giessen Cosmic Station

the polar angle distribution is around 13° ($12^\circ < \theta < 14^\circ$). In addition to the angle cut, timing and azimuth angle cuts were implemented ($|t_{ch} - t_{box4}| < 5$ ns, $|\phi| < 0.4$ rad,). After all selection criteria was implemented, the reconstructed hit position on the radiator was chosen as 750 mm $< y_{reco} < 850$ mm for data and 850 mm $< y_{reco} < 950$ mm for MC regarding the higher amount of coincidence. After all cuts, the region with the highest amount of coincidences is obtained between 300 mm $< x_{reco} < 500$ mm. Due to the small number of hits and not applying any energy selection, the Cherenkov smile is hardly visible. Other plots of the Cherenkov smile for different azimuth angle selection criteria can be found in Figure A.2 in appendix A.

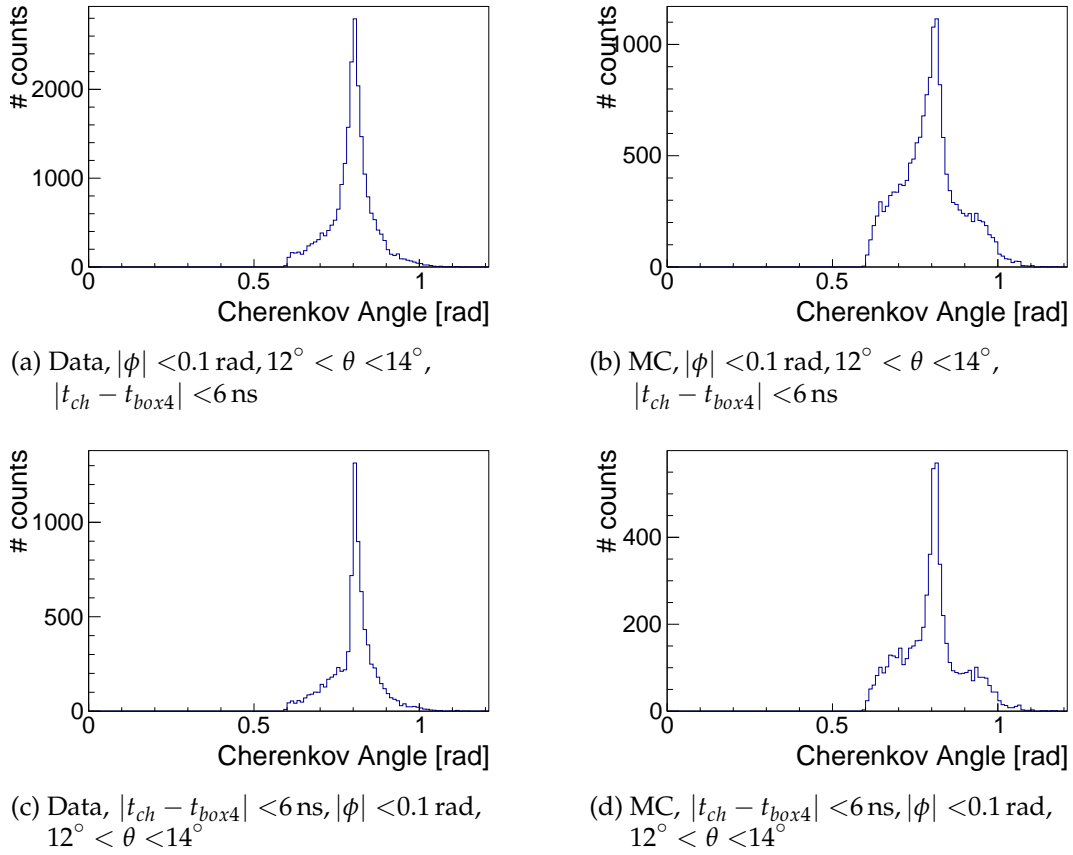


Figure 5.19.: Preliminary results of reconstructed Cherenkov angles for data (left) and MC (right). Upper plots without any cut and bottom ones show pattern with the cuts applied.

The Cherenkov angle is reconstructed for MC and data by using formula (4.6). The distributions are shown in Figure 5.19. For data the Cherenkov angle peak around 0.8 rad with an anti-symmetric background was obtained in Figure 5.19a and Figure 5.19c. These results were expected as a result of not applying the energy cuts. The MC results in Figure

5.19b and Figure 5.19d were obtained by applying the same cuts. As a result, a larger amount of an anti-symmetric background with a wider peak was obtained. Since it is not available for data, the energy cut was applied only for MC in Figure 5.20 as a last step of the analysis.

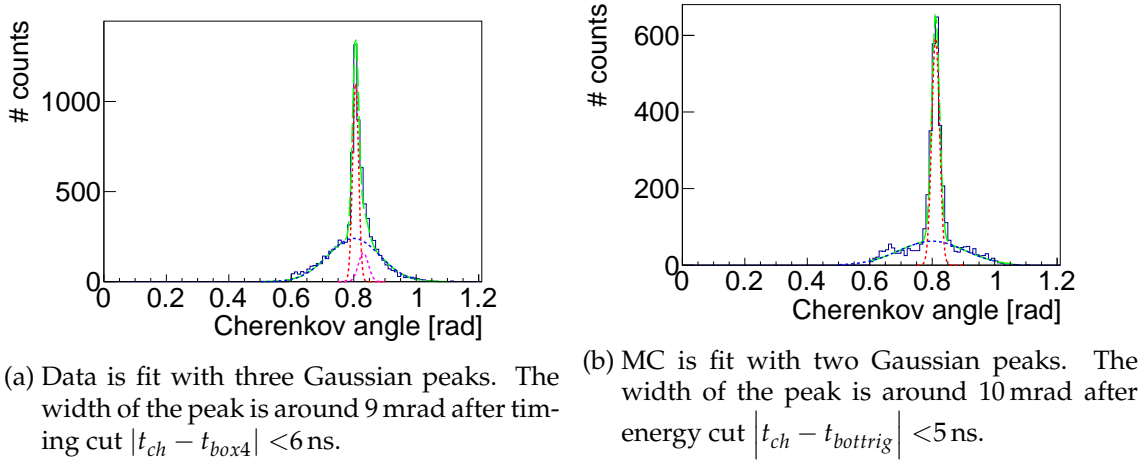


Figure 5.20.: Cherenkov angles were fit for MC and data, after the applied cuts. Angle cuts were applied for both: $|\phi| < 0.1$ rad, $12^\circ < \theta < 14^\circ$ Left: Cherenkov angle distribution, Right: with two Gaussian fitting.

In Figure 5.20, the energy cut was applied to select the muons with energy higher than 600 MeV. As a result of this cut, the Cherenkov angle distribution was obtained around 0.8 rad with 12 mrad single photon resolution.

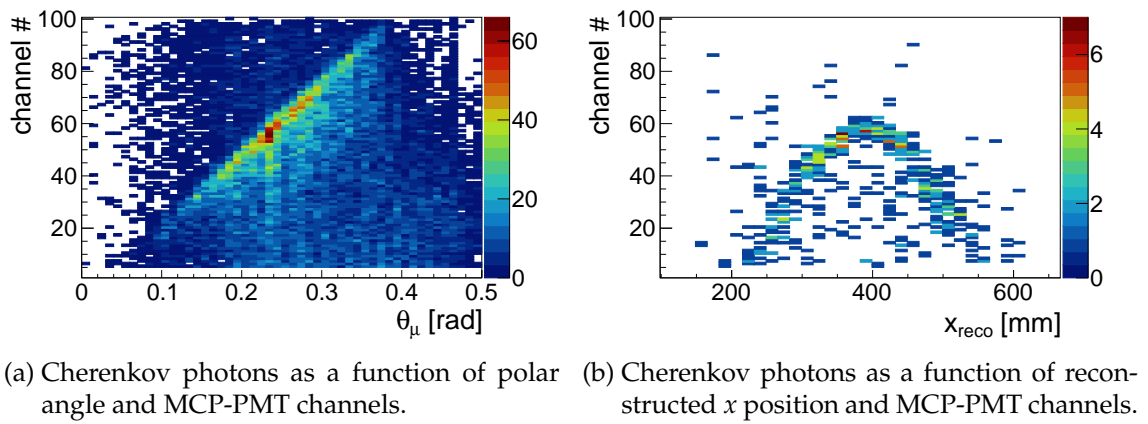


Figure 5.21.: MC results with energy cut and angle cuts were applied $|\phi| < 0.1$ rad, $12^\circ < \theta < 14^\circ$.

In Figure 5.21, MC analysis was redone with an energy cut in addition to the position,

5. Giessen Cosmic Station

polar and azimuth angle cuts. The results are clearly better compared to the ones without energy cut. Due to experimental problems with the bottom trigger signal and low statistics, the results of data are only available without energy cuts currently.

Further histograms of the diagonal pattern and the Cherenkov smile with an applied energy cut are shown in appendix A.

6. CERN Beam Time Experiments

6.1. Introduction

In this chapter, the beam time experiments will be discussed with technical details and successful results from 2018 CERN T9 area.

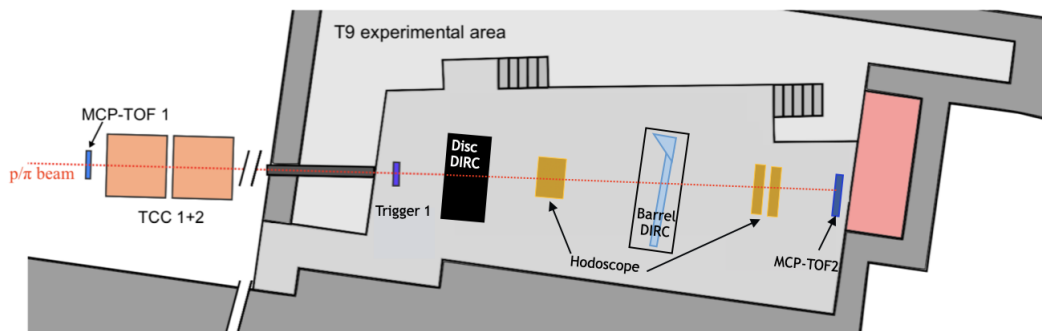


Figure 6.1.: CERN PS/T9 beam time facility. The mixed π/p beam enters from the left.

The prototype of the EDD was tested in the Proton Synchrotron (PS) T9 (Fig. 6.1) beam line area in August 2018 at CERN. The primary particles are sent to the T8 area whereas T9, T10 and T11 areas recover the secondary particles after protons hitting the target. The T9 beam line is designed to deliver primary and secondary particles with momentum between 1 GeV/c and 24 GeV/c. Different heads of the target lead to different components of the beam. During the test experiments, the π/p beam with the momentum range from 2 GeV/c to 15 GeV/c available. The 2018 EDD prototype was tested simultaneously with a Barrel DIRC [PANDA17b] prototype, thereby using the information from two MCP-TOF stations [Uhl15] which were provided by the team from University of Erlangen-Nuremberg.

The goal of the beam time experiment was to measure the performance of the current prototype with a momentum scan from 7 GeV/c to 10 GeV/c for a mixed π/p beam. The results were compared to Monte-Carlo simulations. The Monte-Carlo simulations were done within a GEANT 4 Framework [A⁺03] by including smearing effects, photon loss, and quantum efficiency of the sensors's photocathode as a function of wavelength. Some

6. CERN Beam Time Experiments

specific features of the electronics such as charge sharing, dead channels, cross-talk and dark count rate were not implemented [Sch17]. But still, similar results are expected to be obtained between the simulations and the data.

In the T9 area, the π/p beam passed the MCP-TOF1 station before entering the experimental area. It first hit trigger 1 station and traversed the EDD prototype afterwards. Cherenkov photons were created in the fused silica and internally propagated through the bars with or/and without any reflection on the rim of the radiation. An example of the photon trajectories can be seen in Figure 6.2 as blue lines.

6.2. Testbeam Results

6.2.1. Prototype Components

The size of the radiator with $500 \times 500 \text{ mm}^2$ and 20 mm thickness is smaller than the final radiator for handling and cost saving reasons. It is made of fused silica and coupled with the optical elements by using optical grease. For the final EDD, the aim is to glue the bars to the radiator edge to stabilize the optimum position. For the beam time measurements, the coupling with grease is the best option instead of gluing since the ROMs might require the re-positioning or re-coupling flexibly during the beam time.

The sketch of the prototype can be seen in Figure 6.2 with five readout modules (ROM). For cost reasons, only three ROMs were instrumented as colored with yellow in the sketch 6.2. The dimensions and the positions of the elements can be seen on the sketch and from the table 6.1. The origin of the coordinate system is positioned at the bottom-right corner of the sketch. The x-axis is aligned horizontally and the y-axis vertically. According to the upstream view, the beam direction points towards to the reader (in -z direction). The laser (PiLAS) was diffused from the left side of the prototype as a reference signal to allow for elimination of time differences between the electronic elements connected via different cable lengths. The red framed A-point shows the position of the beam while changing the angle of the radiator with respect to the beam direction. It is located at the same height as ROM3, i.e. the α_{FEL} angle can be assumed to be around zero. The angle was changed from 4° to 22° to cover the polar angle range that is aimed for the final design of the EDD in the PANDA detector. The red dots represent the beam positions for the vertical scan. Charged particles are expected to traverse the prototype, thereby producing Cherenkov photons. These photons enter the bars at different α_{FEL} angles which results hits at different pixels. There are expected hit patterns (i.e. *Cherenkov smile*) depending on the position of the beam which indicate the presence of Cherenkov photons. These patterns will be explained and showed in detail in the following sections. The position scans were done by using an adjustable table which was designed for the beam test purposes. The adjustable table has a platform that can be moved remotely in vertical and horizontal direction. In addition to the 2-dimensional movements, the angle of the prototype was changed by placing a rotary table on the platform of the adjustable table.

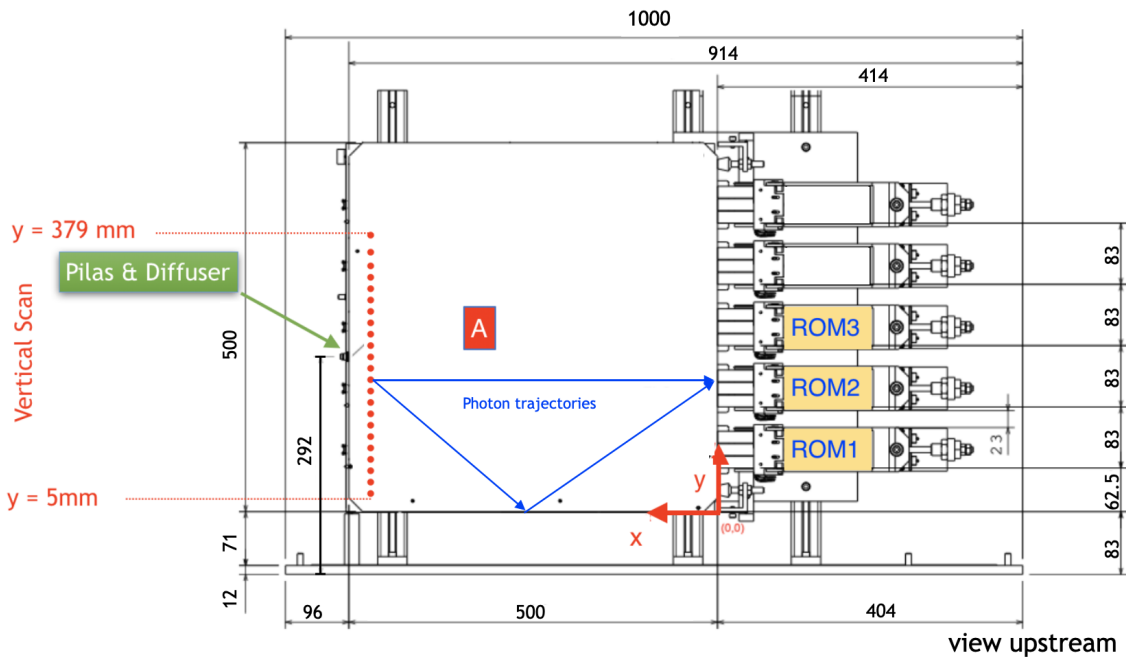


Figure 6.2.: Upstream view of the Disc DIRC prototype with geometric dimensions in mm. The beam position is indicated by red dots for the scan, and red A represents the fixed beam position while the angle of the prototype is changed with respect to the beam direction.

6.2.2. Preparation of the Optical Elements

Each ROM case consists of three bars, three focusing elements and one MCP-PMT with either 128×6 (Hamamatsu) or 100×3 (Photonis) segmented anode structure. In the first photo (1) in Figure 6.3, the optical elements inside the case can be seen. They are stabilized by using the plastic screws on the top part of the case. In the top middle photo (2) of the Figure 6.3, the coupling liquid dropped on the surfaces and the rectangular shaped glass is put on the liquid. The glass borders can be seen in third photo in Figure 6.3. The same steps were followed between MCP-PMT surface and the filter. Optical grease matching the refractive index of fused silica coupling was used between the cathode surface for the MCP-PMT and the filter in Figure 6.3. In order to get rid of the bubbles in the grease, the filter was moved with small circular motions during the attachment procedure. In the middle bottom photo (5), the filter with the MCP-PMT can be seen in Figure 6.3. The ready-to-couple ROM with the sliding units can be seen in the last photo in Figure 6.3.

The fused silica radiator was cleaned with the special latex tissues by using isopropanol before coupling the ROMs (first photo in Figure 6.4). The optical grease is put on the surface of the bar (second photo on Figure 6.4) and then pushed towards to the radiator side

6. CERN Beam Time Experiments

ROM	FEL	x [mm]	y [mm]
ROM1 - Photonis XP85132-S-MD3	FEL 9	0	60.21
	FEL 8	0	77.21
	FEL 7	0	94.21
ROM2 - Hamamatsu YH0245	FEL 6	0	143.50
	FEL 5	0	160.50
	FEL 4	0	177.50
ROM3 - Photonis XP85132-Q-MD3-HA SN 748P001	FEL 3	0	226.89
	FEL 2	0	243.89
	FEL 1	0	260.89

Table 6.1.: The position of the ROMs and the FELs during the test beam experiment at CERN.

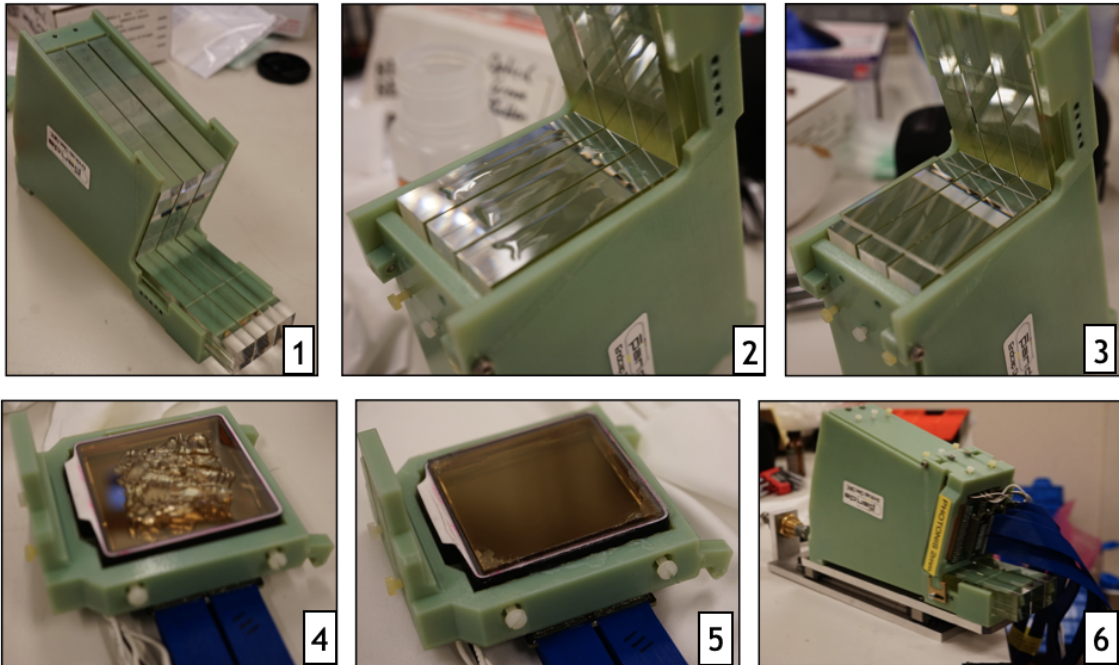


Figure 6.3.: ROM preparation steps.

(third photo in Figure 6.4) with the help of the springs at the back side of the ROM case. The three ROMs were coupled by following the same steps. The quality of the coupling between the radiator side and the bars was checked before closing the two sides of the radiator with black material (fifth photo in Figure 6.4). Afterwards, the light-tight box was closed to prevent external photon entry. The sixth photo in Figure 6.4, closed light-tight box with the electronics can be seen. Three different MCP-PMT were used, Photonis

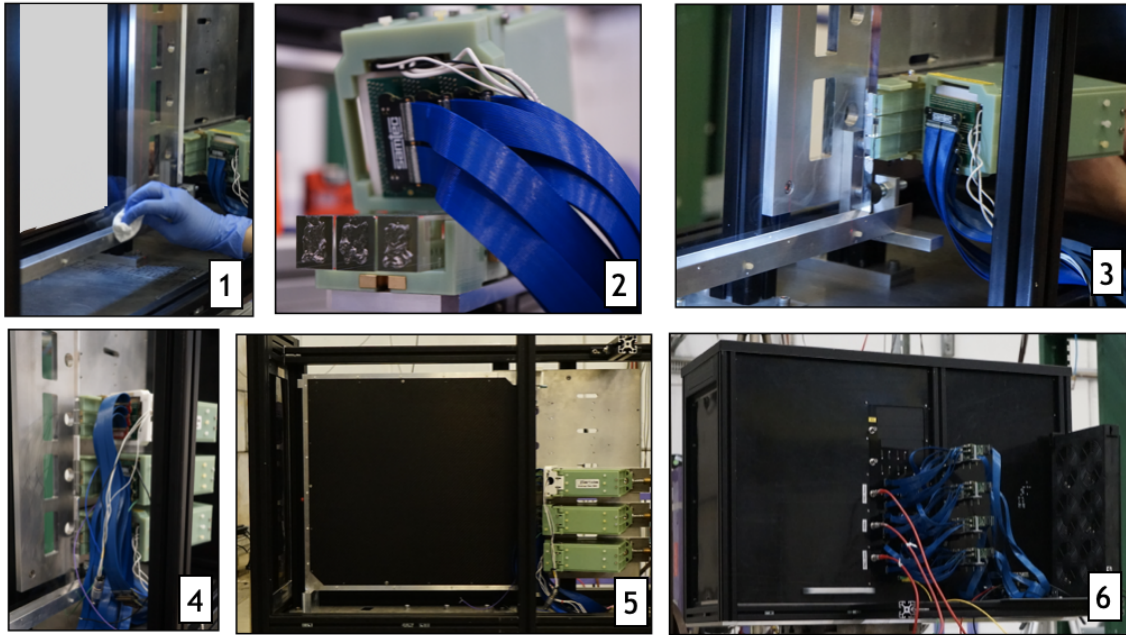


Figure 6.4.: The steps of cleaning the radiator and coupling the ROMs.

XP85132-S-MD3 in ROM1, Photonis XP85132-Q-MD3-HA SN 748P001 in ROM3 with 100 pixel in each three rows and Hamamatsu YH0245 in ROM2 with 128 pixels in each six rows.

The anodes of the sensor was connected to the shielded coaxial Samtec cables [sam21] that carries digital signals to the readout system. The readout system was based on TOF-PET2 ASICs which is designed by PETsys company [pet20]. For the beam time, two front-end boards (FEB/D-v2) were used for two positive and negative signal polarization with 19 ASICs. 16 ASICs were connected to the first FEB/D-v2 board to detect the Cherenkov photon hits from the MCP-PMT, two ASICs were connected to tracking boxes for estimating the beam width, the last ASIC was connected to the laser signal and two MCP-TOF stations as triggers. By using the time-of-flight information, particle separation was achieved successfully for the momentum lower then 8 GeV/c. The tracking boxes are identical to the ones used in the GCS as described in chapter 5. Each tracking box includes 48 SiPM bars and each bar is positioned with a shift between the neighbors on a plane that is parallel to the beam direction. In order to track the beam spot, the bars in tracking boxes were aligned perpendicular to the each other and to the beam direction. By labelling the beam direction in negative z , the boxes have the SiPM bars aligned along x -axis and y -axis.

6. CERN Beam Time Experiments

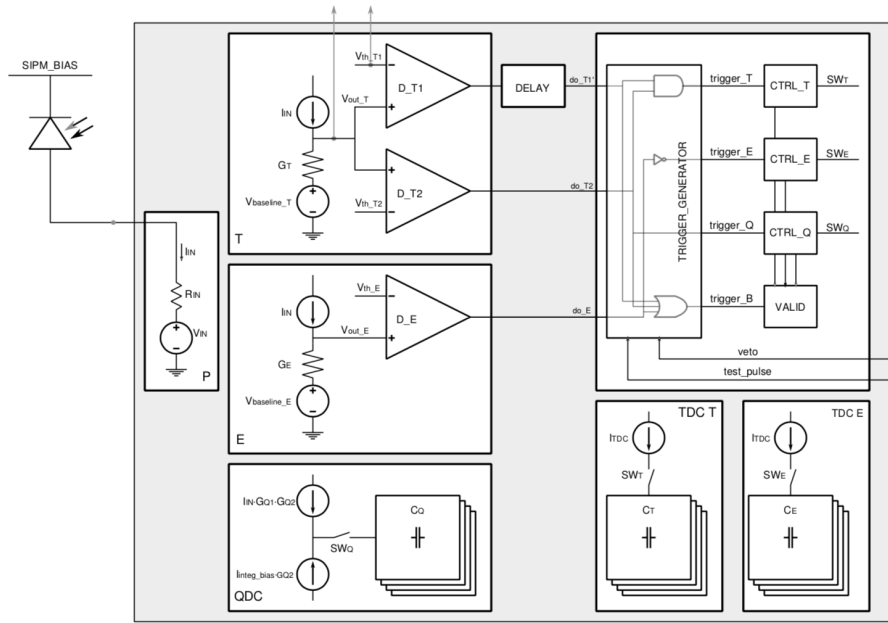


Figure 6.5.: Simplified diagram of the channel readout architecture [BFF⁺19].

6.2.3. Data Acquisition

Data acquisition was accomplished in 18 days and around 2 TB size of data was recorded for the offline analysis. The calibration and the threshold scan of the each channel were performed to find the optimum values for the settings. In order to understand the logic of rejecting or accepting a hit as an event in each channel, the simplified sketch of the architecture can be seen in Figure 6.5.

For data acquisition, the TOFPET2 readout system was used. It is designed for the SiPMs which provides a positive signal polarity. In our prototype setup, the ASICs were used to detect a mix of negative and positive signal polarities. The positive signals from the MCP-TOF stations and the hodoscopes are detected the combination of the negative signals from the three MCP-PMT sensors. According to the diagram in Figure 6.5, the low impedance R_{IN} is connected to the sensor output signal I_N which is fed into three different stages, T, E, and Q. The branches T and E include a transimpedance amplifiers to convert I_N into a voltage $V_{out,T}$ which will be feed into the discriminators together with the thresholds T_1 , T_2 or T_E . After that, the output is transmitted into the logic gates for a proper event selection. The branch Q is for the QDC operation which measure the total charge stored in the capacitor C_Q . The threshold values were increased to make *hot* channels less active. The opposite operation was applied for *cold* channels. For an uncertain reason, some channels remained dead and could not be calibrated for the entire beam time.

After optimum threshold settings were found, the baseline and dark count scans were performed. In Figure 6.6, the connectors in a red frame and the connections between the

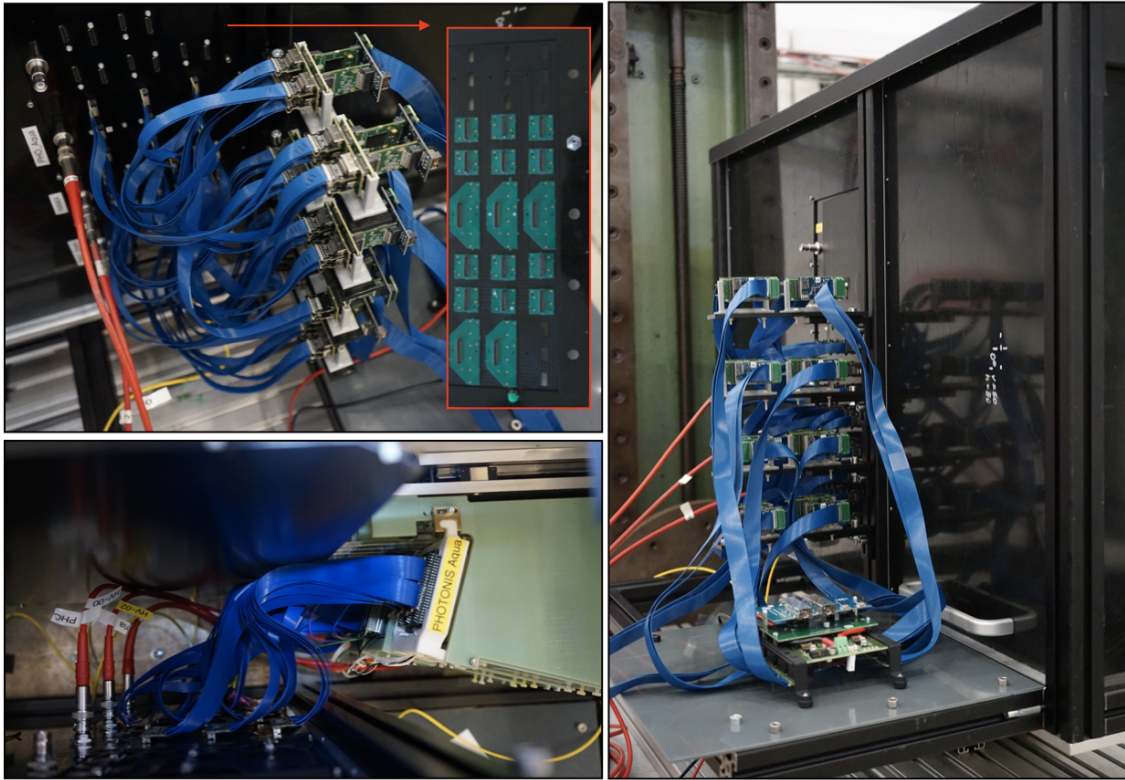


Figure 6.6.: The readout system of the EDD 2018 prototype.

MCP-PMTs on the wall of the box can be seen in the upper left photo. The lower left photo shows the red high voltage cables and the top view of ROMs with blue samtec cables. These cables carry the analog signals from the MCP-PMT anodes to the ASICs on the FEMs. In the right photo, 8 FEMs with 16 ASICs are connected to the FEB-D/v2 board via Samtec flat cables which carry digitized signals. In the readout system with 19 ASICs and two D-boards synchronized by getting the system clock (200 MHz) from the DAQ board. The connections were provided via a μ HDMI to HDMI cable between the DAQ system and the D-boards. The D-boards have a Molex connector where a μ HDMI head was connected and conveying the signal to the fan-out-box with a HDMI ending. The fan-out-box was connected to DAQ board in DAQ PC with PCIe bus. The μ HDMI transmits the signals from D-board to DAQ board while transmitting the clock information in the opposite direction.

The output of the measurements are in raw data format (.rawf) which does not have a correct timing information. Due to that reason, the post processing for each channel in the ASIC is performed by using a calibration function which is implemented into the code depending on the desired output format i.e. text or root-tree [BR97]. Moreover, from the way TOFPET FPGAs are processing data it is known that the signals from D/boards

6. CERN Beam Time Experiments

can come partially unsorted in time. In order to correct for partial temporal disorder the heap sort algorithm is utilized on the TOFPET data stream. A heap with 5000 entries is used as an intermediate data container to account for a maximum of 5000 events between unordered time stamps. This turned out to be a sufficient buffer size for getting a completely time-ordered output stream.

The event sorting algorithm makes use of the heap data container available in C++ and it consists of three main steps:

1. The first 5000 incoming time stamps are used to create the heap tree according to the standard sift procedure to obtain time-ordered branches with event entries.
2. A new event leads to dropping the earliest event from the heap and inserting the new event according to its time stamp position into the heap, again using the sift procedure.
3. Step 2 is repeated until the whole data stream is processed.

The time-sorted TOFPET ASIC channels were mapped to MCP-PMT pixels.

6.2.4. Offline Analysis

A flowchart of the offline analysis can be seen in Figure 6.7. To prevent huge file sizes for each parameter scan, all runs were partitioned into 30 minutes fragments. To group the files into proper input, they were chained with TChain algorithm (root specific algorithms have been used). The offline data analysis selects time ordered events from the chained tree by looping over the entries. The time difference between the MCP-TOF stations was the crucial condition to make the particle selection. If an entry is occurring within the time slot of the MCP-TOF stations, the correction is applied to the selected entry. The time information of the selected hit was differentiated from the MCP-TOF1 to find the region with the highest coincidence. Events which did not occur in that specific time slot were excluded as a background. Then a sophisticated geometrical reconstruction algorithm was applied to calculate the Cherenkov angle by tracking back from the pixel of the MCP-PMT to angle information.

The flow chart for the MC event selection in Figure 6.7 at the right is similar to the logic of the offline analysis. The incoming event is mapped to the corresponding pixel and selected with the angle cut. As a result, it is saved as a selected event. The MC simulations are used to assess if the prototype meets the requirements of the final PANDA EDD design.

Although the analysis was done for each row of the MCP-PMTs, the results are presented only for one MCP-PMT with proper data statistics.

Calibration

After the test beam experiments, two different calibrations were applied before analyzing the data. The first correction was applied to eliminate the time delay. The delay between

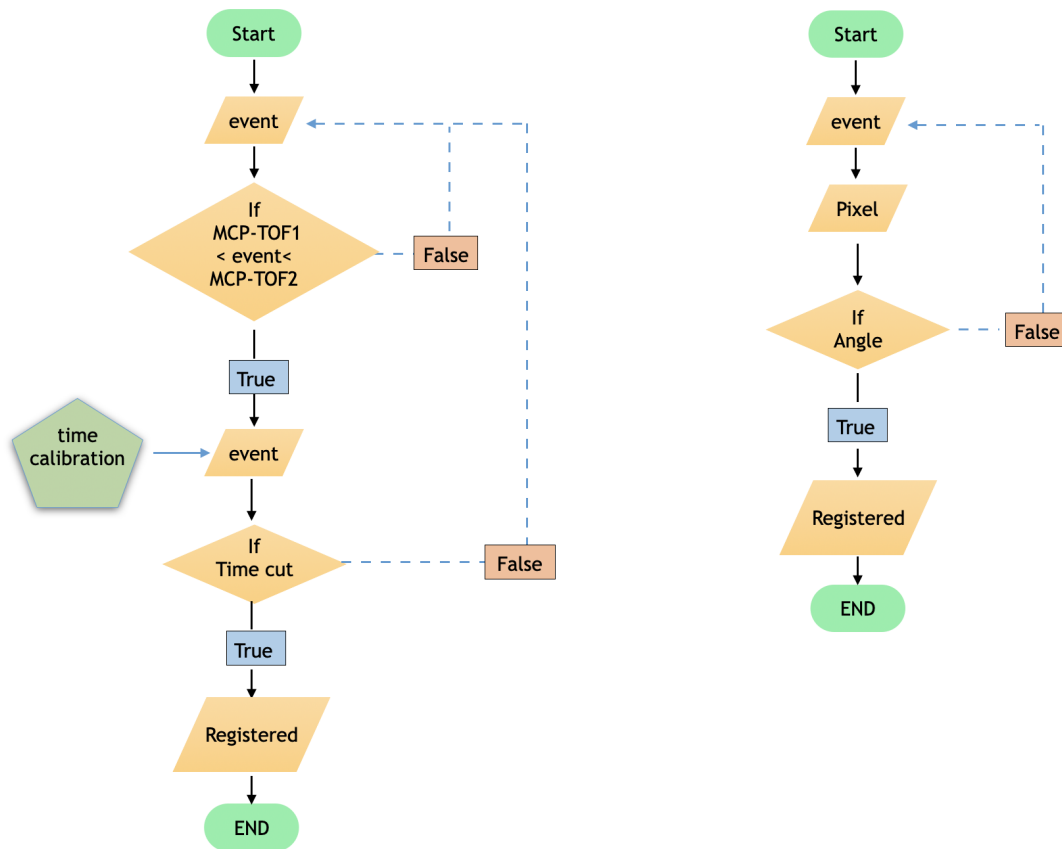


Figure 6.7.: The flowchart of the analysis code for the beam time data (left) and MC (right).

the electronics were determined with the laser reference signal. Proper time offsets were added to the corresponding channels before further analysis.

Since the FELs convert Cherenkov photon angle information to position information on the MCP-PMT photocathode surface, the calibration was done according to the exact position of the FELs. The FELs in the prototype and the simulations studies use the same position information. However, the slight differences between the simulations and the real data occurs and causes the miscalculations of the Cherenkov angle. The details of the correction are given in the following section.

Time Offset Calibration

Different cable lengths and the delay in the electronic elements resulted in specific time offsets during the measurements. In order to detect the shifts between the signals, the time offset calibration was done by using a laser signal as a reference. Since each ASIC

6. CERN Beam Time Experiments

has 64 channels, one and half ASIC covered the pins of an MCP-PMT row which leads to utilizing two different ASICs with potentially different timings either in one FEM or two different FEMs.

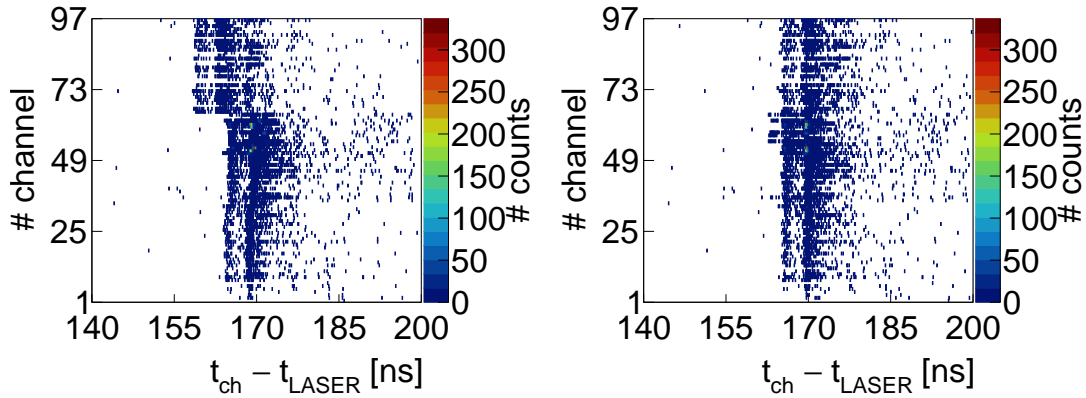


Figure 6.8.: Left: Channel hits as a function of the time difference between the laser signal and the time of the signal, before the correction. Right: Channel hits as a function of time difference between laser signal and signal time, after the correction.

In Figure 6.8, the left plot shows the time difference between the channels and the right plot shows the corrected time difference. The first 64 channels were connected to one ASIC, the rest of the channels were connected to the other ASIC in one FEM. The x -axis shows the time difference between the reference laser signal and channels. The y -axis is one row of the MCP-PMT channels and the color-axis shows the hits in the channels. After adding the time offset, signals were properly aligned in the right plot in Figure 6.8.

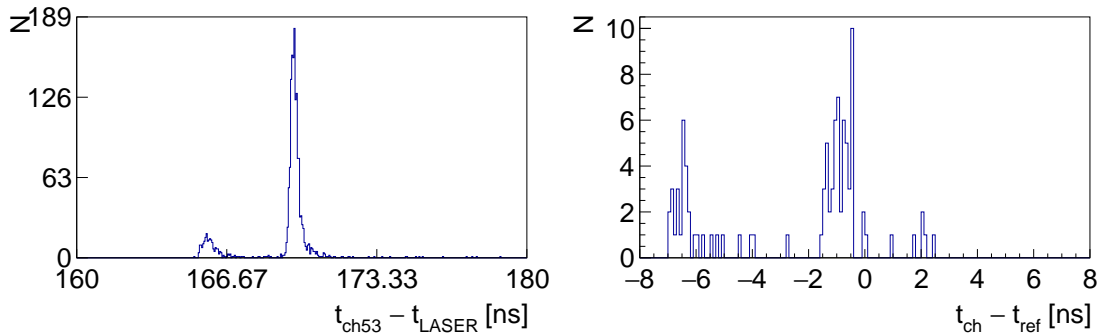


Figure 6.9.: Left: The time difference between the reference channel and the laser. Right: The delay between the reference channel and the other channels.

In order to make a time correction, the channel with the best acquisition statistics was chosen as a reference channel to be used for further analysis. The left plot in Figure

6.9, the time difference between the reference channel (Ch 53 in this case) and the laser was calculated. The x -axis shows the time difference and y -axis shows the number of counts. The peak time location was chosen as a reference time for the rest of the channels. Afterwards, the time difference between the rest of channels and reference channel was calculated (right plot in Figure 6.9). The time difference is about 8 ns and was added to affected channels to eliminate the shift in Figure 6.8.

Optical Calibration

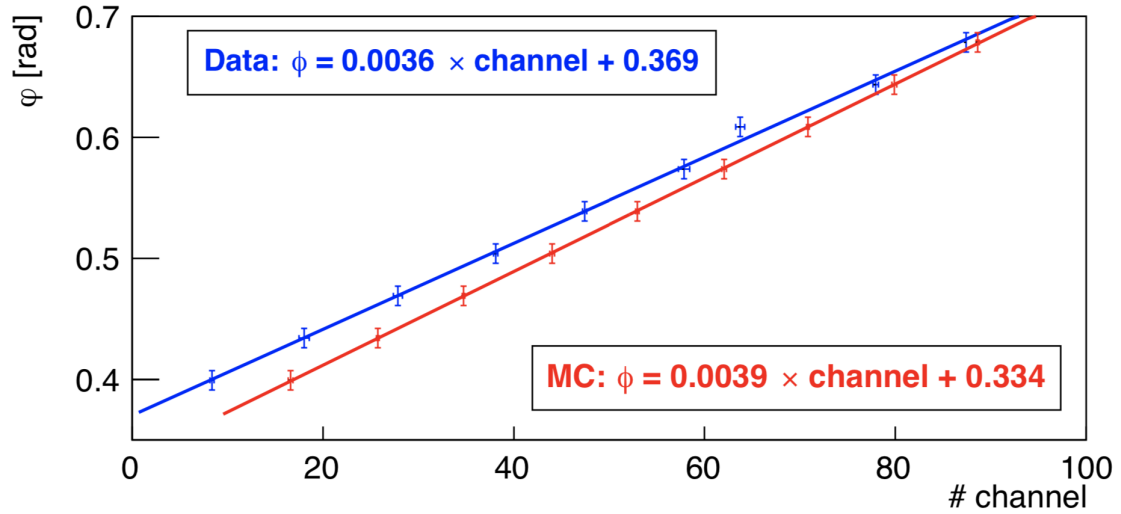


Figure 6.10.: The ϕ angle distribution as a function of MCP-PMT channels for data and MC.

The sensor position influences the reconstruction of the Cherenkov angle which is converted to the pixel information. The position calibration was done according to the bar that the photon enters with zero α_{FEL} angle. ϕ' is the photon angle measured by the sensor, ϕ is the azimuth angle depending on the photon entry angle and FEL position. When α_{FEL} is zero, the relation between ϕ' and ϕ becomes

$$\tan \phi' = \tan \phi \quad (6.1)$$

and the Cherenkov angle can be calculated with the

$$\theta_c = 90^\circ - \theta_p - \phi \quad (6.2)$$

where θ_p is particle (beam) angle.

Since the beam angle and theoretical value of the Cherenkov angle of the pion are known, ϕ is available. Moreover, the relation between ϕ' and ϕ . The angle ϕ is plotted

6. CERN Beam Time Experiments

Scan Type	x [mm]	y [mm]	θ_p [degree]	P_{beam} [GeV/c]	Step Size	Figure
Vertical	422	22 mm - 379 mm	18°	7 GeV/c	17 mm	6.19, 6.20
	422	5 mm - 379 mm	10°	10 GeV/c	17 mm	6.14, 6.15
Momentum	420	39	18°	5 GeV/c-10 GeV/c	1 GeV/c	6.29
Angle	252	422	2° - 22°	7 GeV/c	2°	6.22, 6.23
	85.21	420	2° - 22°	6 GeV/c	2°	6.28

Table 6.2.: The scans at different positions and/or different momenta.

as a function of channel number of the MCP-PMT which has a 0.5 mm pitch. Figure 6.10 shows the relation between φ (in radian) and channel number for data and MC separately. The points show the data and the fit with continuous straight lines that gives the m and b in the formula of

$$\phi'(z) = mz + b. \quad (6.3)$$

The values are calculated and applied to the data analysis to reconstruct the Cherenkov angle.

6.2.5. Position and Momentum Scans

In this section the position and momentum scans will be explained. The motivation is to confirm the performance of the radiator at different momenta and positions. Depending on the different position scans, there are different corresponding expected hit patterns of the Cherenkov photons as explained before. These patterns will be explained at different momentum. The details of the parameter scan can be seen in Table 6.2. In Figure 6.2, the beam position for the vertical and angle scan was shown with red dots and red framed A respectively. The vertical scan was done for 22 different points with 17 mm step size, considering the bar size of 16 mm and additionally 1 mm distance in between the bars. Some of the Cherenkov photons may leave the radiator while the rest may reach the FEL with or without reflections from the side of the radiator (blue trajectory lines in the sketch.)

Before giving the details of the parameter scans, the time difference between two MCP-TOF stations will be discussed depending on the momentum. In Figure 6.11, there are two peaks visible in the left upper plot at 3 GeV/c momentum. The small peak shows the protons hits in the MCP-TOF stations and the second peak shows the pion hits. The proton peak appears at a later time compared to the one of pions. Depending on the momentum increase, the time differences between MCP-TOF stations for pions and protons coincide. Due to the resolution of the readout electronics, peak separation is not visible for momenta above 8 GeV/c.

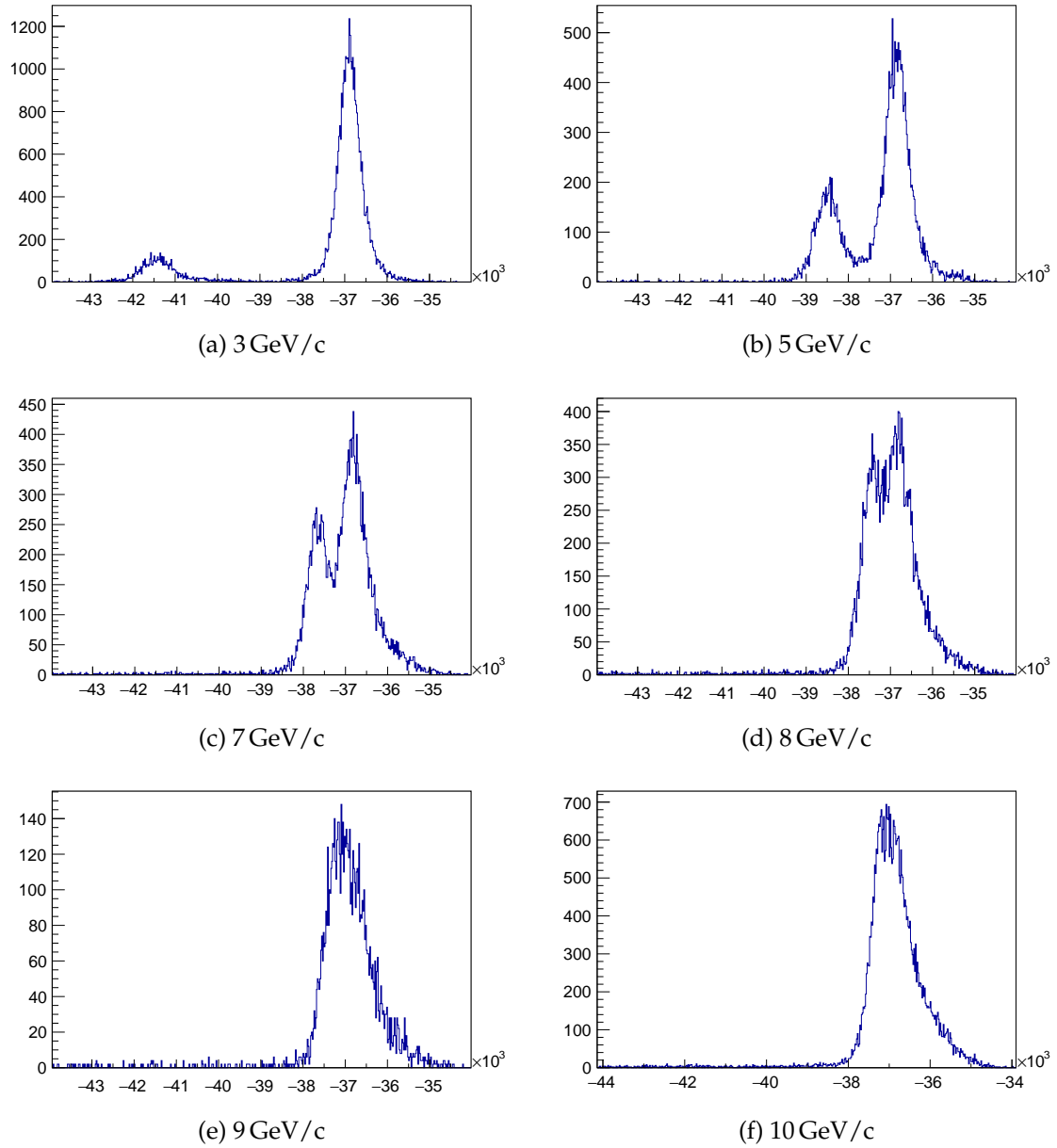


Figure 6.11.: The x -axis shows time difference in [ps] between MCP-TOF stations, y -axis shows number of events, starting from left upper to the right bottom, 3 GeV/c to 10 GeV/c respectively.

The 10 GeV/c Scan

It is crucial to test the prototype performance at higher momenta since the PANDA detector has two operational mode which the higher momentum is one of them. Due to

6. CERN Beam Time Experiments

the time difference characteristics of the TOF stations, the particle separation was not achievable as explained in the previous section. Furthermore, the hit patterns as a result of the data analysis are provided for pions and protons together. The vertical scan at 10 GeV/c momentum was completed with 10° angle of incidence (AoI). The prototype was moved in vertical direction to make the beam hit on the radiator surface starting from 5 mm to 379 mm. The logic for the analysis is based on using the MCP-TOF stations as triggers, and to save all hits on the MCP-PMT anode pins for the time between these triggers. The MCP-PMT pins are corresponding to the ASIC channels of the TOFPET2. The data is saved depending on the event selection criteria with the proper thresholds of the TOFPET2 ASICs.

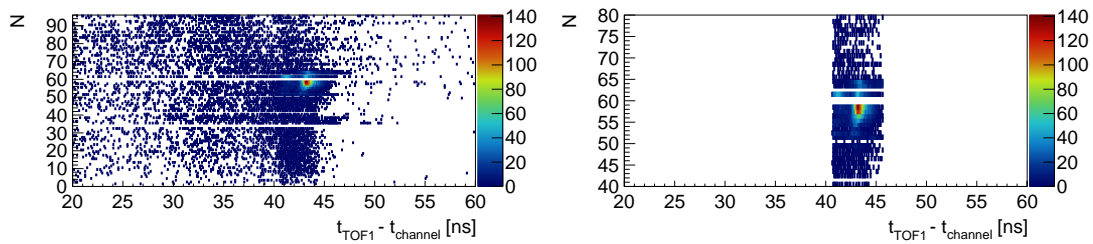


Figure 6.12.: The time difference between TOF1 and sensor channels at 10 GeV/c momenta at $y = 243$ mm, $x = 422$ mm

Figure 6.12 shows the time difference between the trigger and the MCP-PMT channels. The maximum number of hits is accumulated around channel number 60 with 5 ns time window. In order to exclude the background, a time cut was applied and resulted in Figure 6.12 at the right plot. The white lines represent dead channels which did not respond during the experiments.

The Cherenkov angle was reconstructed in Figure 6.13 after a time cut by using a sophisticated geometrical algorithm. The distribution of the Cherenkov angle for four different vertical positions as shown in Figure 6.13. From left upper to the right bottom plots, the vertical position changes from $y = 5$ mm, $y = 56$ mm, $y = 209$ mm, and $y = 379$ mm respectively. The distribution of reconstructed angles for lower vertical positions shows a different behaviour from the other two bottom plots. In Figure 6.13, the background at $y < 209$ mm dominates the signal and cause a larger width, Single Photon Resolution (SPR) of the peak. It is expected to have a better distribution where the beam hits at the same height of the readout system positions ($y = 252$ mm).

The accumulated Cherenkov photons can be seen as a function of the MCP-PMT channels and vertical position in Figure 6.14. The entries were normalized with the hits from trigger events where the trigger events were calculated from the integral of the time difference between the MCP-TOF stations for the corresponding momentum. The maximum coincidence region between 180 mm to 379 mm was intended to calculate the Cherenkov angle to exclude the strange behaviour for smaller y -positions in data. The nominal Cherenkov angle is around 0.82 rad for 10 GeV/c and it is independent of the beam position for data and MC. However, due to the large values α_{FEL} , the smearing

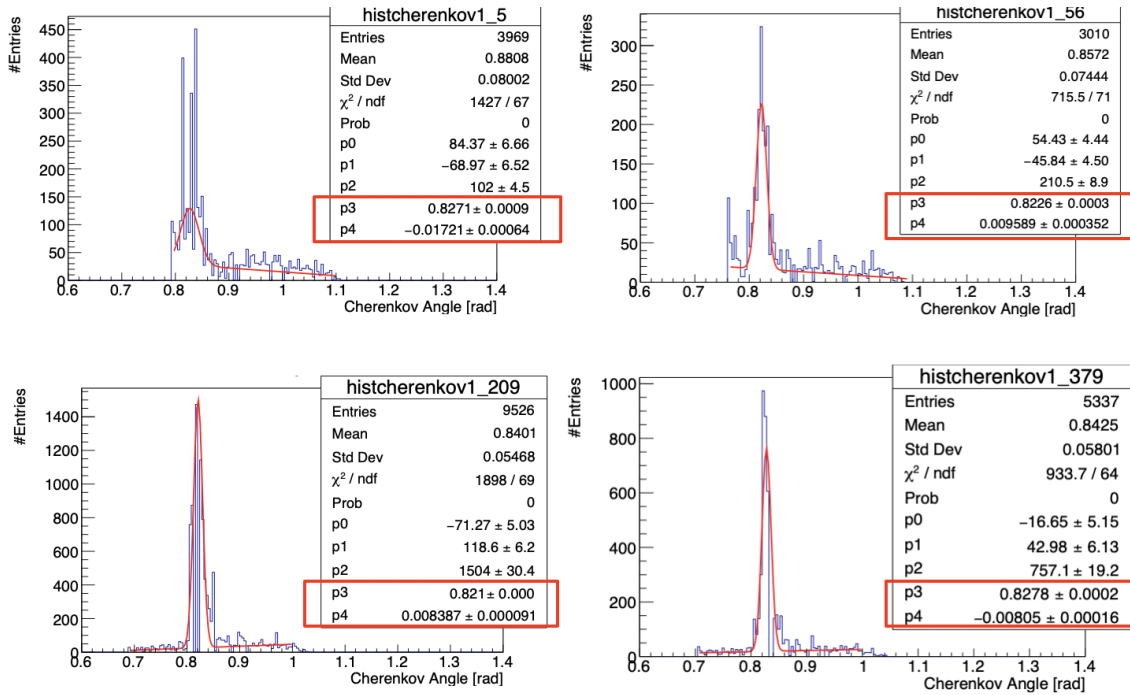


Figure 6.13.: The distribution of reconstructed Cherenkov angles at different vertical positions at 10 GeV/c momentum.

effect dominates the distribution and results different calculated Cherenkov angle. This can be seen for the position $y = 379$ mm where the α_{FEL} is the biggest for data and MC. In Figure 6.15 the reconstructed Cherenkov angle compared with MC results can be seen for this region. Data and MC is comparable since MC is simulated regarding the same conditions during test beam such as position of the ROMs, hit position of beam, etc. When the beam position is reaching the same height of the readout module at $y = 252$ mm, the results get better. The reconstructed data shows a good agreement with MC. The right plot in Figure 6.15 shows the compared SPR for MC and data. The data results are larger than MC due to problems with the readout system and statistical error bars get visible for the plots. During the data taking, it was realized that in contrast to their technical specifications, the 2018 version of the ASICs were not compatible with the negative polarity of MCP-PMT signals. Due to that reason, the threshold and the calibration settings could not be set to an optimum. PETsys confirmed oscillations in negative polarity mode in their later diagnosis. This resulted in fluctuations of the noise level and deteriorated the result by reducing the readout efficiencies. These obstacles were not experienced for the production batch of TOFPET1 ASICs which gave good results in 2016 DESY test beam experiment [Sch17].

In order to determine the performance of the prototype at 10 GeV/c, the number of Cherenkov photon hits per trigger is calculated and compared with MC results in Figure

6. CERN Beam Time Experiments

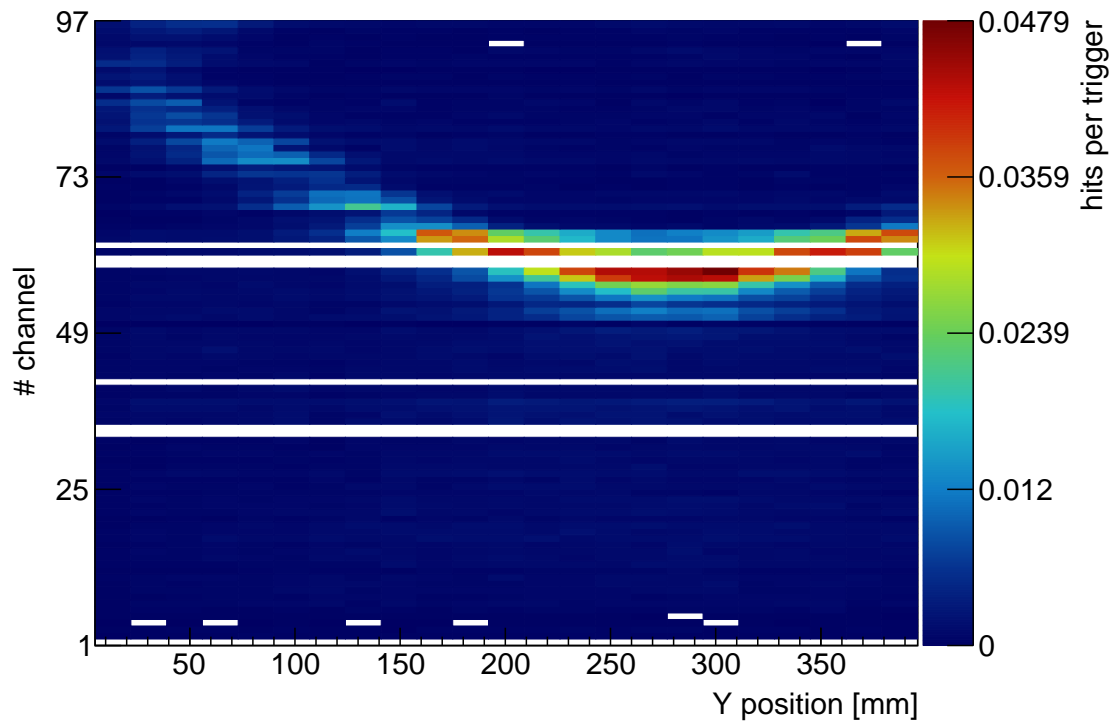


Figure 6.14.: Cherenkov photons as a function of channel distribution and vertical axis at 10 GeV/c.

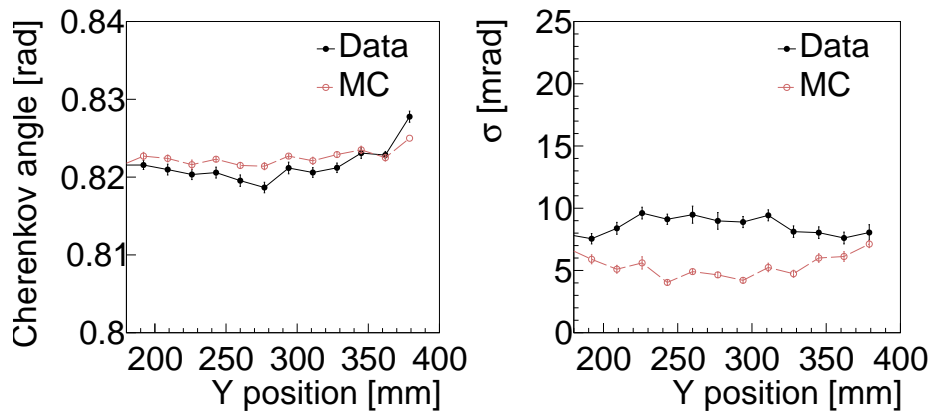


Figure 6.15.: Single photon resolution and Cherenkov angle distribution at 10 GeV/c.

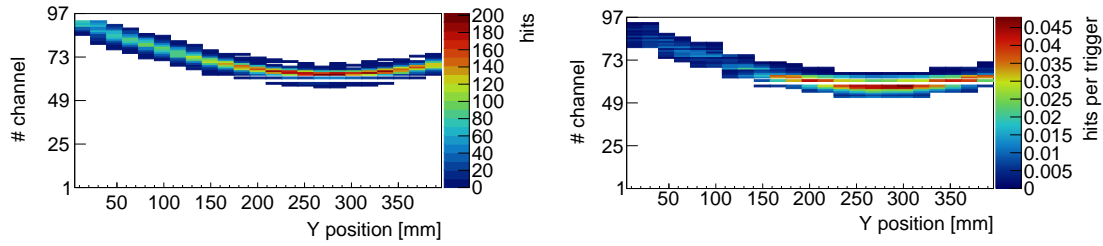


Figure 6.16.: The Cherenkov smile for MC (left) and data (right) after excluding background.

6.16. The background is cleaned as much as possible with a time and pixel cut, in order to choose Cherenkov photons exclusively. The presence of the dead channels is effecting the efficiency of data analysis. To make a successful comparison between MC simulation and measured data, the same number of dead channels is further implemented at the same position into MC. The output of the MC code is shown in Figure 6.16. The color-axis in the left plot shows the total hits differently from the color-axis in the right plot. The MC code is different from the code which is written for reconstruction of data as explained in previous section. For the right plot the hits are calculated per trigger at the beginning. The hits were divided per trigger at the end of the code and plotted in Figure 6.17. The compared number of hits in Figure 6.17 for data and MC can be seen. The increment from 0 mm to 200 mm is slightly visible for the data. The reason of not having a very smooth line is the dominating noise background which was caused by the aforementioned readout problems. The more beam hits closer to the readout system, the better efficiency obtained. Due to this reason, better efficiency results are obtained for the maximum coincidence region. For bigger than 300 mm, the missing channels dominate the system and drop the number of hits to some degree. The scenario is similar regarding the missing channels in MC simulation. The efficiency is more stable than data except for the positions where the dead channels are dominating the results. The efficiency results of MC is two times higher then the data results. This is expected as a result of incompatibilities of the ASICs with negative signal polarity.

As a result of the vertical scan at 10 GeV/c, the prototype performance is reasonable and comparable with MC in spite of the readout problems.

The 7 GeV/c Scan

As a next step, the vertical and angle scans are realized at 7 GeV/c. The motivation was to obtain Cherenkov photon hits for different angles and positions for different particle species separately. It also provides the identification performance of the detector prototype. Pions and protons are identified by using the time-of-flight information of the MCP-TOF stations as an external discriminator. In Figure 6.18, the time difference between the MCP-TOF stations at 7 GeV/c momentum can be seen for both particle species separately. In an ideal system, two clearly separated peaks are expected to be seen. Due

6. CERN Beam Time Experiments

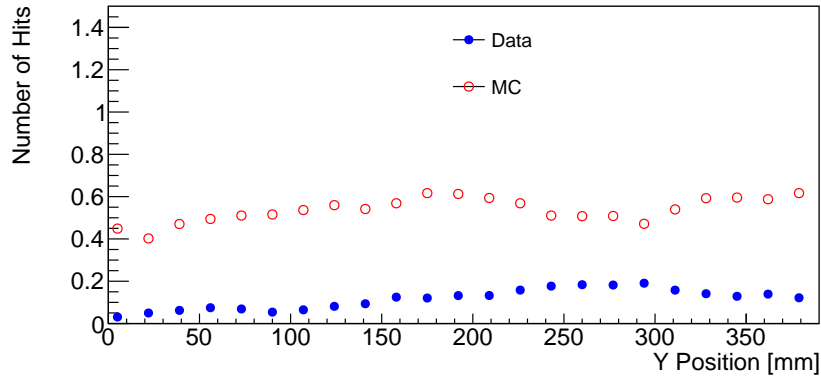


Figure 6.17.: The number of photon hits per trigger for MC simulation and measured data.

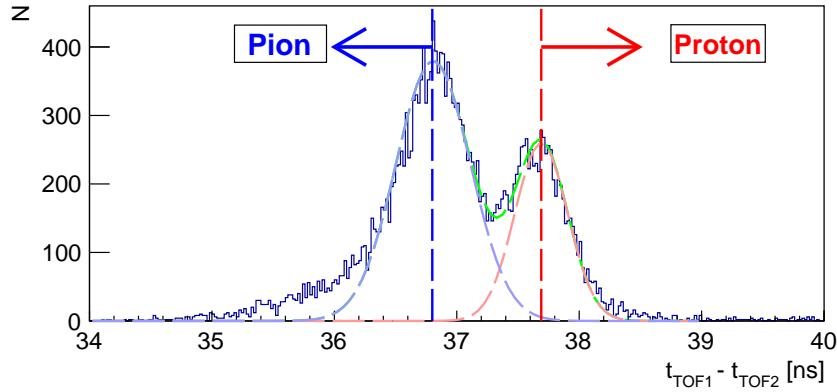


Figure 6.18.: The time difference between two MCP-TOF counters at 7 GeV/c momentum was used for particle identification.

to the finite resolution of the prototype readout system, the separation is not ideal and some overlapping area is in Figure 6.18. According to this figure, the misidentification is calculated as about 2% and the separation power was 3 s.d. at 7 GeV/c which is the required performance to reach for the prototype. In order to make a separation between pions and protons, two separate time cuts were applied starting from the peak positions to the sides depending on the aimed particle in Figure 6.18. The area under the curve with an applied time cut gives the trigger hits.

The time cut for an external particle separation provides the possibility of choosing pions or protons separately. In addition to that, an extra time cut is necessary to increase the data quality by reducing the background effects. The same reconstruction algorithm is used for the Cherenkov angle reconstruction as a function of y position and pixel at 7 GeV/c for pions and protons separately. The horizontal position is 430 mm and the

vertical position is changing from 22 mm to 379 mm with 17 mm step-size and the best coincidence region is obtained around 260 mm. The Cherenkov smile can be seen for particles separately in Figure 6.19. Due to the aforementioned reasons, the background deteriorates the signal when the beam hits a different position relative to the readout system. The Cherenkov angle is reconstructed for the best coincidence region in Figure 6.19.

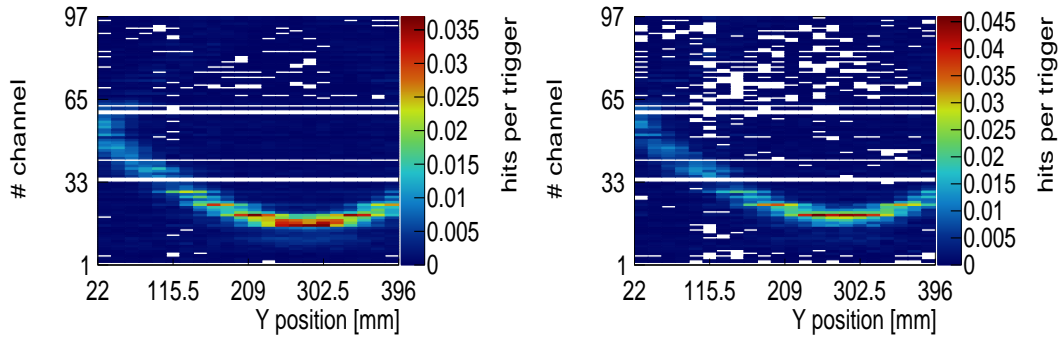


Figure 6.19.: Cherenkov photons create a pattern for pions (left) and protons (right) as a function of the pixel and vertical position.

For the maximum coincidence region, the Cherenkov angle and the SPR are compared with MC results. The left plot in Figure 6.20 shows the Cherenkov angle for pions and protons. The dashed lines show the MC compared with data (continues lines). The blue (red) color represents the pion (proton). The SPR plot in Figure 6.20 shows a better agreement around 260 mm (close to the readout system) compared the rest of the positions. The error bars are coming from the statistical errors.

As a second parameter run at 7 GeV/c, the angle scan is performed at a position of $y = 252$ mm and $x = 422$ mm. The prototype is rotated with the help of a rotating platform from 4° to 22° . In Figure 6.21, the prototype position from the side (left) and the top view with respect to beam angle can be seen. The particles are selected externally for pions and protons separately. Figure 6.22 shows Cherenkov photons for pions (left) and protons (right). By varying the prototype angle, photons hit different pixel on MCP-PMT sensors. Depending on the angle, the diagonal shape is obtained for different angles. The z-axis represents the hits per trigger. The reconstructed Cherenkov angle for pions and proton are compared with the MC results left plot in Figure 6.23. The pion is marked with blue color, the proton is specified with red. The reconstructed Cherenkov angle is shown with continues line whereas the MC is shown with a dashed line. The reconstructed angle for pions fluctuates between 0.82 mrad to 0.83 mrad which MC behaves similar. If the angle is higher than 15° , the acceptable small gap between MC and data occurs. Where the AOI is 8° , the error bar is bigger for the pions data compared to the rest. The error bars only consist of statistical errors since the background is dominating the signal available. For the proton data, the behaviour is akin to the MC results. The SPR for pions and proton is shown in right plot in the same figure. MC results are much more stable

6. CERN Beam Time Experiments

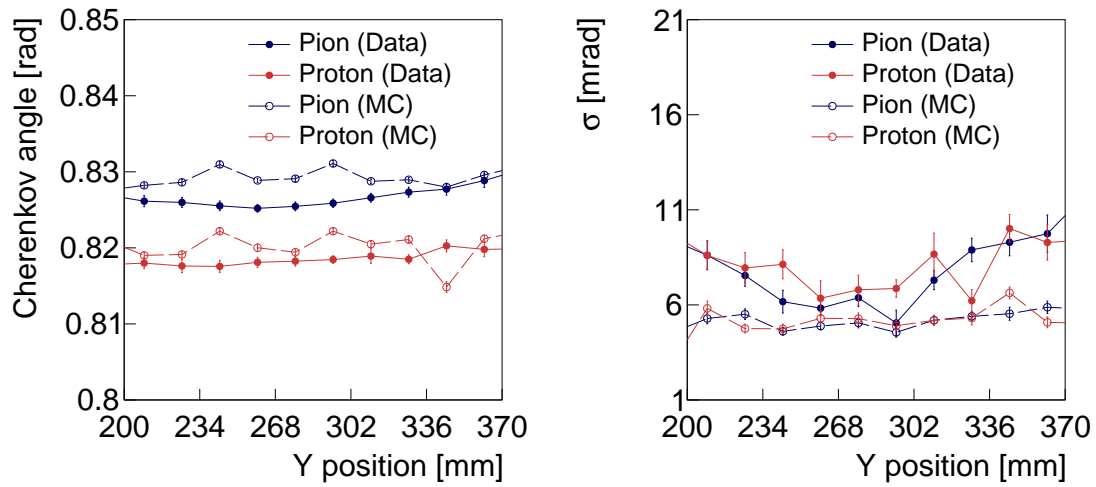


Figure 6.20.: Left: Cherenkov angle reconstruction for different vertical positions. Right: SPR for different vertical positions.

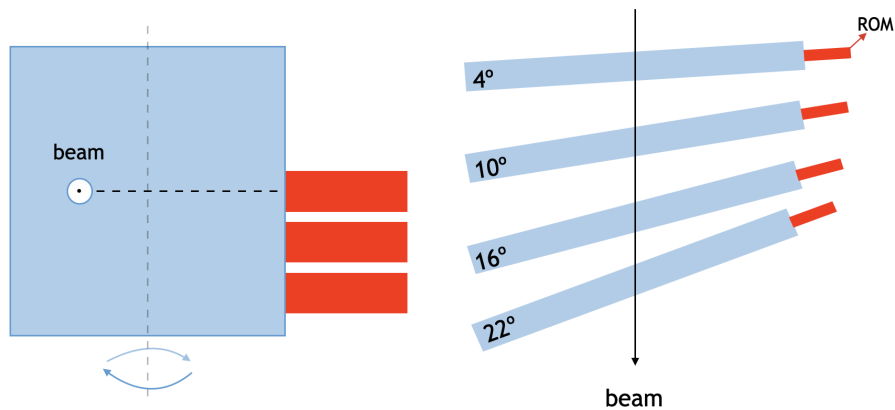


Figure 6.21.: The angle of the radiator position with respect to beam axis.

compared to the data. They are around 6 mrad with small fluctuations. For data results, the maximum SPR was obtained around 11 mrad. It can be said that data and MC shows better agreement at 7 GeV/c compared to the 10 GeV/c momentum.

In Figure 6.24, the channel distribution for pions and proton is shown for the angle and vertical scan. The plots were obtained by fitting the channel distribution including corresponding positions with statistical errors. The channel distribution is obviously distinguishable for these two different position scans. The left (right) plot shows the distribution for different angles (vertical positions).

In Figure 6.25, the Cherenkov smiles for MC and data can be seen. The missing chan-

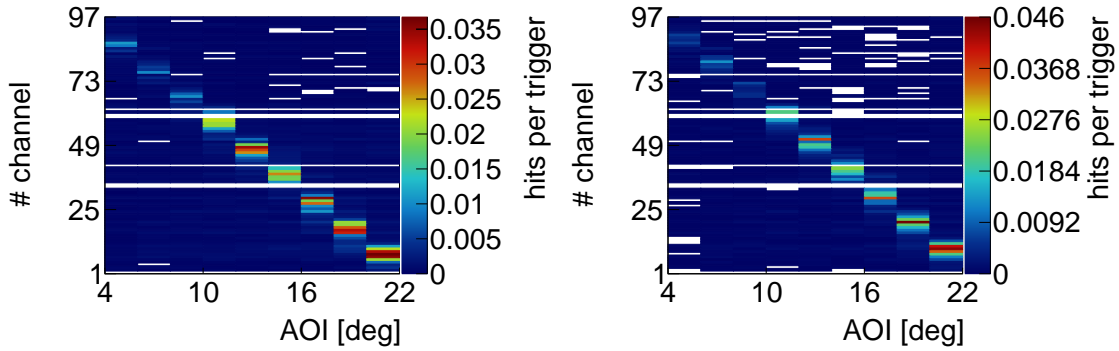


Figure 6.22.: Cherenkov photons depending on the angle of the prototype at 7 GeV/c for pions (left) and protons (right).

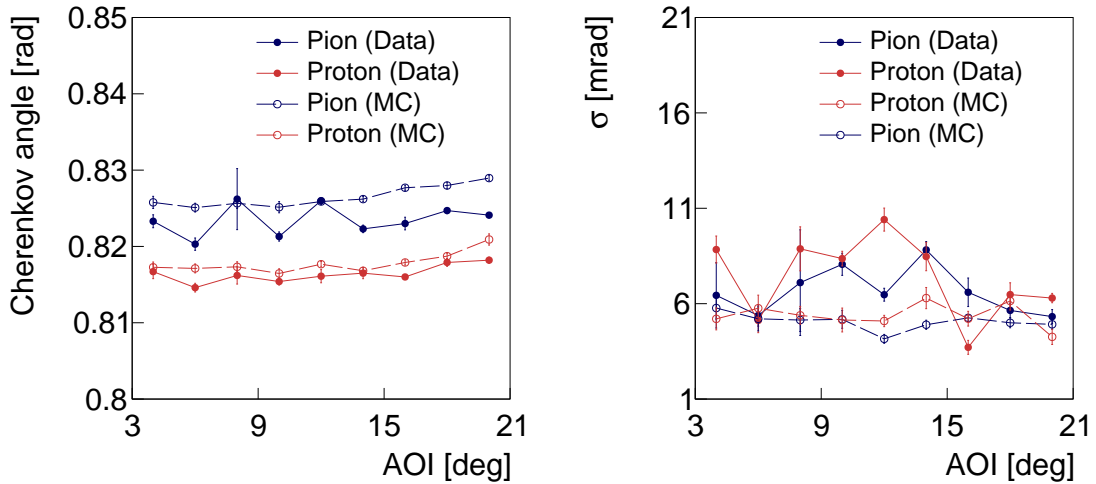


Figure 6.23.: Left: Cherenkov angle reconstruction for different vertical positions. Right: Cherenkov angle reconstruction for different angle settings.

nels are implemented to the MC code to make a reliable comparison. The Cherenkov smiles with almost no background are obtained after extreme cuts for MC and data. The left plot shows the Cherenkov smile for MC without any hit number normalization in color-axis. The normalized number of hits per trigger for MC is shown in Figure 6.26 compared to the data. For data, the number of hits is slightly different for lower vertical positions compared to those larger than 150 mm. The reason of this change can be explained by looking at the Figure 6.25. For the lower vertical positions, coincidence is less than the rest. In addition to the coincidence, the dead channels result in a dropping the number of hits. For MC, the reason of the drop of number of hits is the dead channel

6. CERN Beam Time Experiments

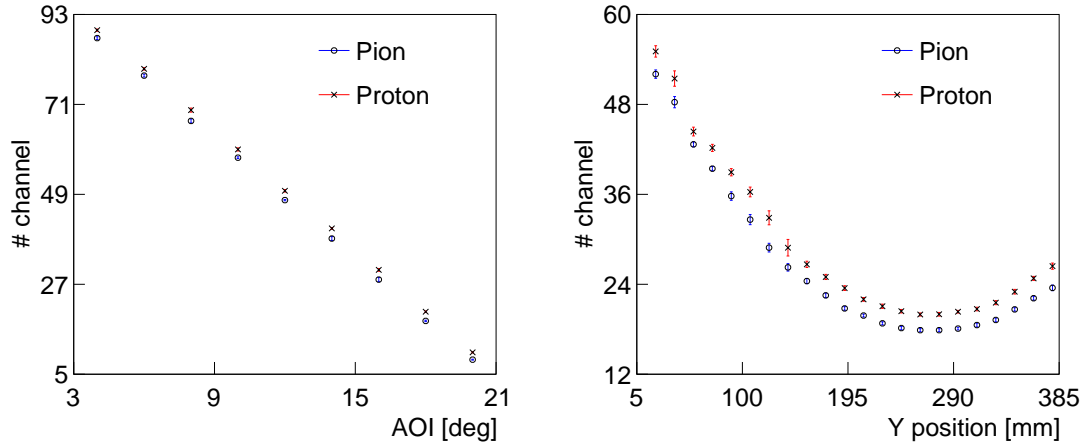


Figure 6.24.: Left: Pixel distributions for proton and pion for AOI at 7 GeV/c. Right: Pixel distribution for different vertical position at 7 GeV/c.

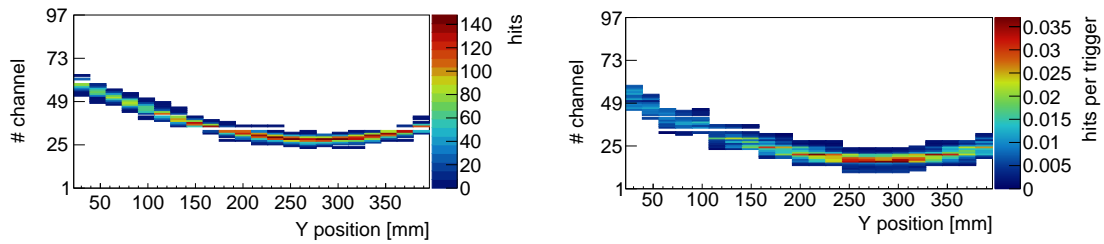


Figure 6.25.: The hit pattern of Cherenkov photons for different vertical positions at 7 GeV/c for MC simulation (left) and measured data (right).

for vertical position. The reason of the difference between the obtained and expected efficiency is the readout problems related to negative signal polarity. A similar result was obtained for 10 GeV/c momentum.

The 6 GeV/c Scan

In the previous section, the angular distribution of Cherenkov photons are shown with corresponding particle identification. The beam height on the prototype is at the same height of the readout system. When the beam height differs such as during the vertical scan at different momenta, more scattered results are obtained due to dominating noise background problems. In this section, the angular distribution results will be discussed when the beam was hitting at a position of $y = 85$ mm on the prototype (Figure 6.27). In Figure 6.27, two examples of the photon trajectories can be seen.

For the analysis, the proton and the pion separation are obtained with the same ex-

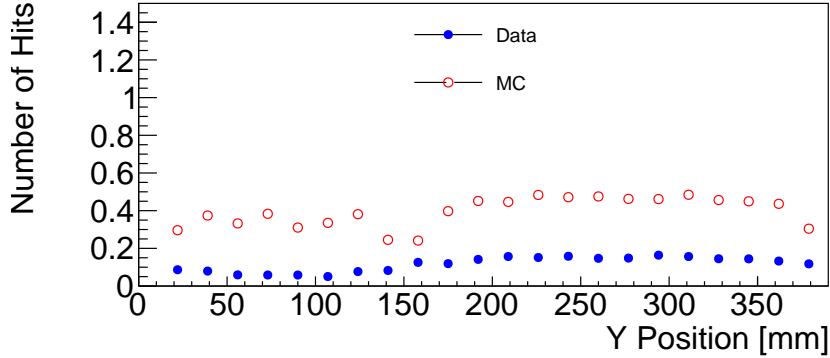


Figure 6.26.: The number of hits of measured data is compared with MC simulations for different positions at 7 GeV/c momentum.

ternal time cut method using MCP-TOF stations. The prototype is rotated as shown in Figure 6.27 starting from 2° to 22° with respect to the normal plane of the beam direction to mimic the polar angles in the PANDA detector. During the experiment the height of the prototype is fixed.

In Figure 6.28, six different angular distribution results of Cherenkov photons can be seen. Starting from the left upper plot, the Cherenkov photons from pions are reconstructed for the highest position of FEL with more statistics, the second highest position of FEL (upper right) and the third highest position of FEL (middle left). For protons, the middle right plot represents the results for FEL9, bottom left and right show for the middle FEL8 and the third FEL7 respectively. A careful reader may realize the differences between Figure 6.22 and Figure 6.28. In these six plots, the data collection statistics are less than the previous angular distribution results at 7 GeV/c. The pattern is slightly shifted to the upwards due to the beam position. In addition to that, small amounts of reflections from the side of the radiator can be seen at the right upper side of the pattern.

These results also indicate how the characteristics of the readout system changed depending on the height of the beam. In spite of the unstable behaviour of the ASICs, the results show the expected patterns of Cherenkov photons.

6. CERN Beam Time Experiments

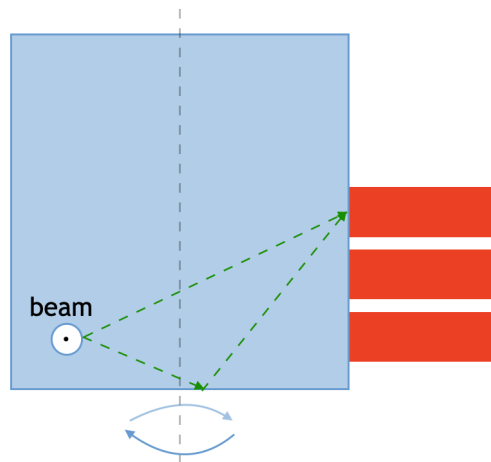


Figure 6.27.: The beam position is shown on the radiator. The green dashed lines represent the track a photon may follow. The gray line shows the rotation of the radiator with respect to normal of the beam axis.

Momentum Scan

After the parameter scan at different momenta, the momentum scan is plotted including the dispersion effect obtained from MC. The motivation of the momentum scan is to prove the performance of the radiator regarding the particle separability depending on the momentum.

The refractive index of a fused silica is a function of wavelength $n = n(\lambda)$ is the dispersion effect of Cherenkov angle for pions and protons. In Figure 6.29, the refractive index is chosen between $1.45 < n < 1.47$ for the fused silica depending on the wavelength is between $300 \text{ nm} < \lambda < 700 \text{ nm}$. The Cherenkov angle is reconstructed for pions and protons by taking the refractive index $n = 1.47$ for fused silica. By receiving the maximum value of refractive index, a momentum scan for pions and protons is done at the upper limit of the theoretical values. Above $6 \text{ GeV}/c$ the resolution of the detector does not allow to separate them externally, and the pion and proton results begin to coincide with increasing momentum. The same effect can be also observed for the theoretical values. For momenta above $4 \text{ GeV}/c$, pions and protons start coinciding.

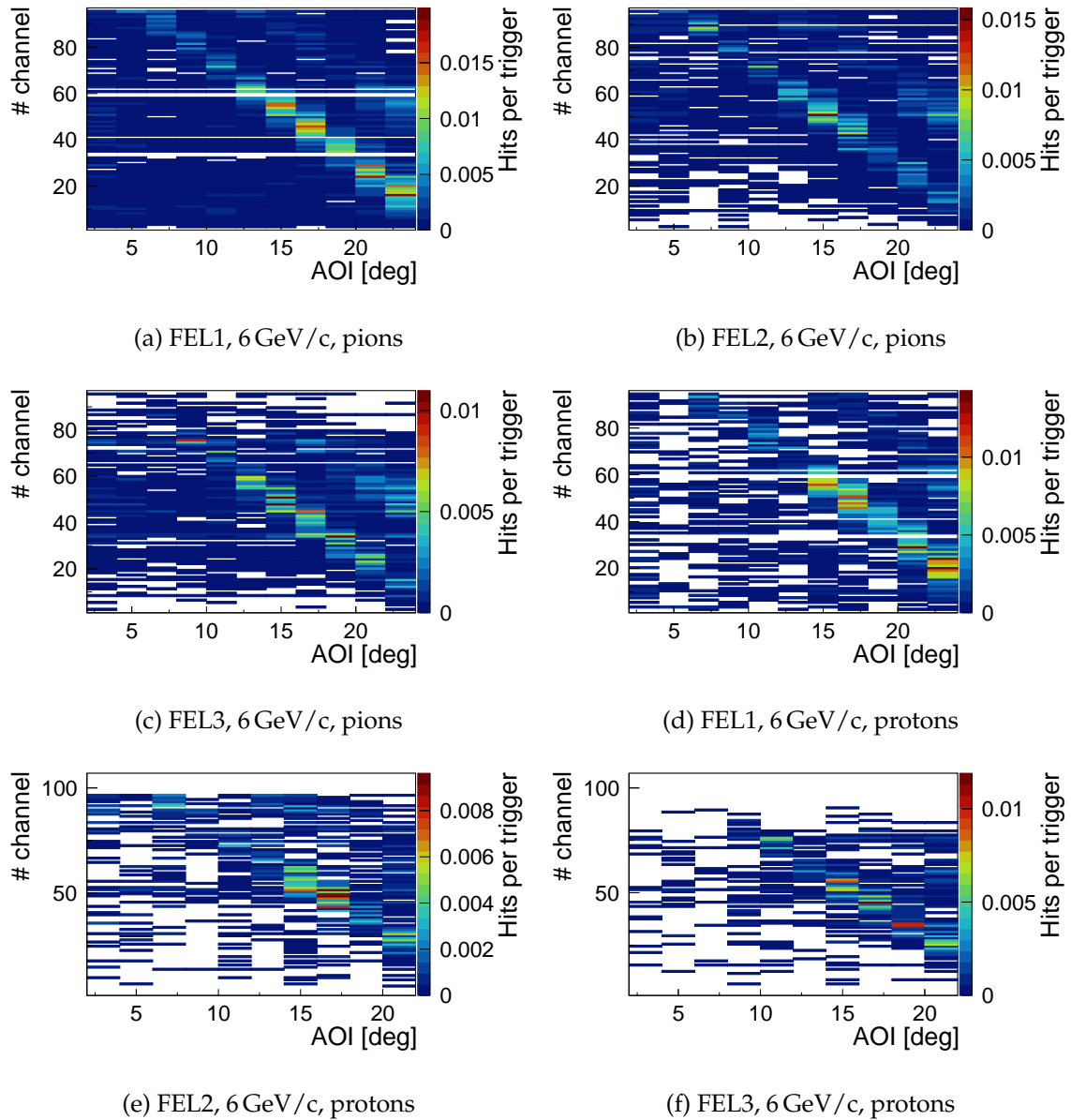


Figure 6.28.: Cherenkov photons as a function of MCP-PMT channel of different FELs for pion and proton is shown at 6 GeV/c.

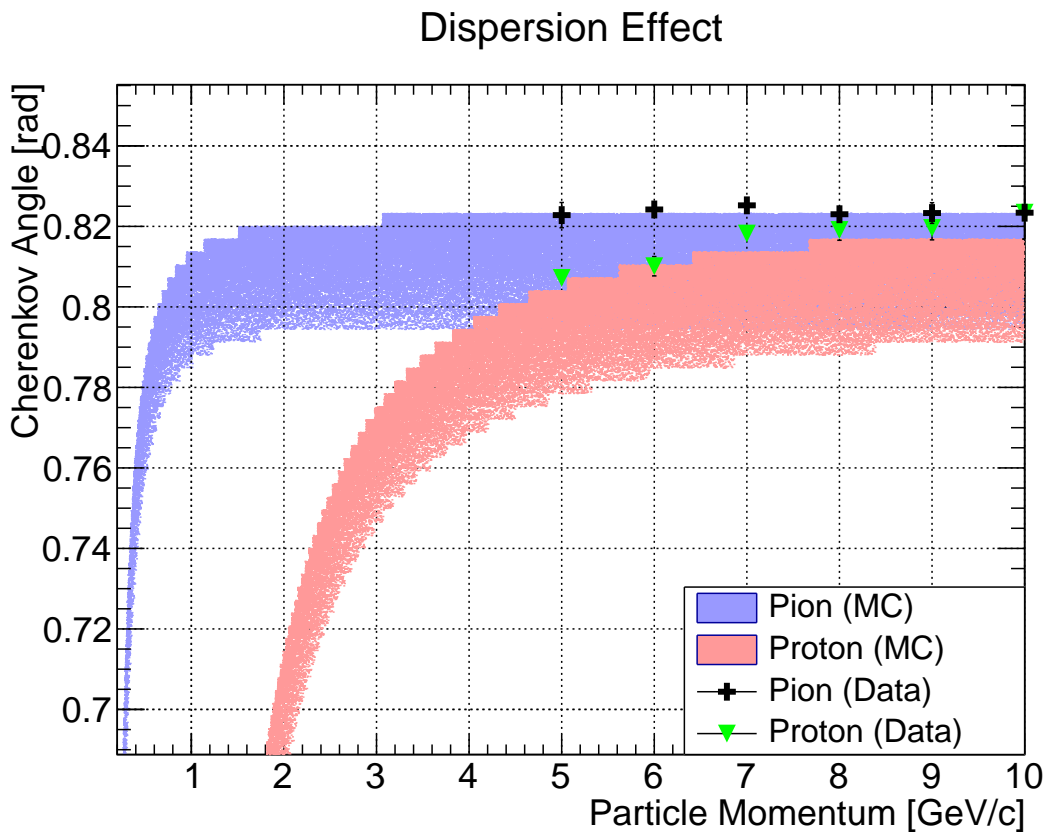


Figure 6.29.: The MC simulation of the dispersion effect is compared to the measured data of pions and protons depending on momentum.

7. Summary and Outlook

This work focused on improving the readout electronics for the final EDD by fixing earlier design deficiencies by considering the challenges on spatial constraints, determining the proper electronic components which can work in the endcap region, designing the efficient permanent cooling system, and testing frontend electronics during all intermediate steps in an upgraded Giessen Cosmic Station (GCS).

The readout system of the EDD is based on TOFPET2 ASICs which were designed by PETsys company for PET applications. To determine the parts to be improved according to the requirements, the bottlenecks of the previous system were determined. Some incompatibilities were realized between the existing readout system and the sensor during the test beam at CERN in 2018. This issue highly affected the calibration of the system and the quality of data acquisition. This incompatibility was confirmed by PETsys company and fixed in the production batch of the 2020 ASICs. With the incompatibility problems in mind, a thorough analysis of test beam data showed that the EDD prototype was able to perform for different momenta.

GCS is a setup that consists of four tracking SiPM boxes for reconstructing the muon tracks and two trigger plates for selecting muons with energies above 600 MeV. It was upgraded with light-tight boxes for the optical components and by providing temperature stabilization with an improved liquid cooling system. The recent production of ASICs and the readout system together with the full-size disc DIRC quadrant were tested by using cosmic muons as a representative source of photons generated by the Cherenkov effect in the radiator. The emitted photons were detected by MCP-PMTs which were connected to the 2020 production of ASICs for digitization purposes. These Cherenkov photons were used for the reconstruction of Cherenkov angles plotted as a function of extrapolated positions of muons on the radiator and MCP-PMT channels. The characteristic patterns of the Cherenkov photons were compared with Monte-Carlo simulation results and the agreement of both was convincing. This shows the reliability of the electronics and the GCS system. MC results were also shown by selecting high energetic muons which are not currently available for measured data due to the unreliable signals from energy selecting trigger plates.

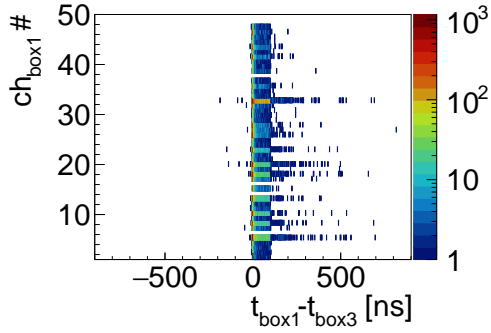
After confirming the performance of the readout system, a custom one-body PCB was designed in collaboration with PETsys company. The new design omits SiPM related parts and adds elements considering radiation hardness, and their compatibility in the magnetic field. Different designs of the custom design PCB were discussed and it was proposed to reduce the number of readout modules (ROM) to 6 per side. A light-tight magnet box was designed to test the custom-designed PCB. Permanent magnets can be added and positioned depending on the experiment goal. To cool the custom-design PCB, a liquid cooling system with an optimized heat pipe layout was implemented into

7. Summary and Outlook

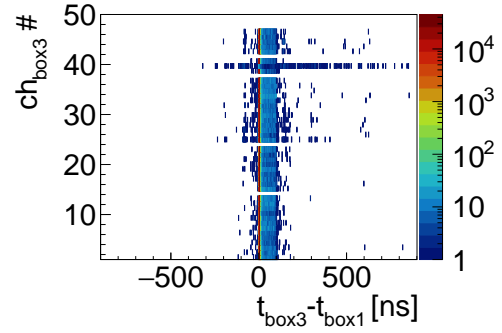
the magnet box.

The successful constructions detailed in the thesis move the EDD closer to its final implementation in PANDA. Promising results were already obtained for the CERN test beam and the GCS, making the signal readout and data acquisition ready for the demands of the physics program in future phases of the PANDA project.

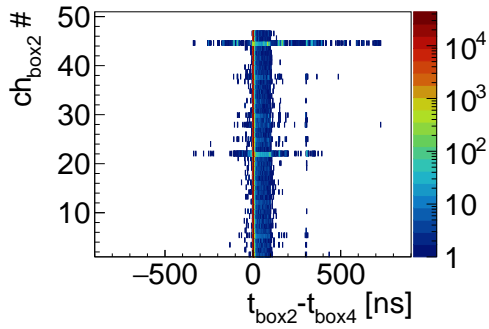
A. Appendix



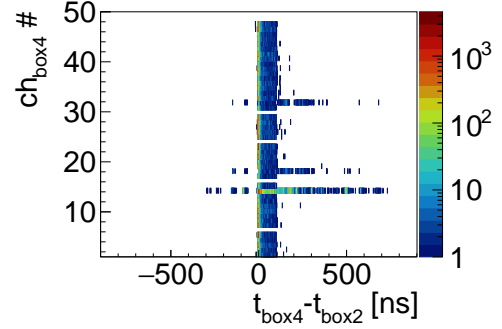
(a) Reconstructed x -position of the muon hits for all MCP-PMT channels.



(b) Reconstructed y -position of the muon hits for all MCP-PMT channels.



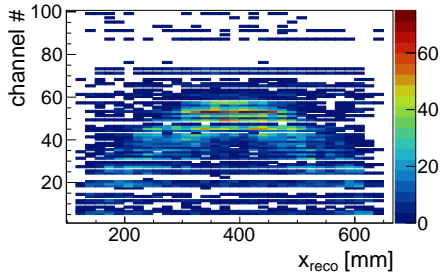
(c) Reconstructed x -position of the muon hits for all MCP-PMT channels.



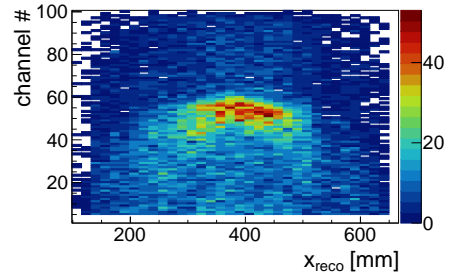
(d) Reconstructed y -position of the muon hits for all MCP-PMT channels.

Figure A.1.: Specific position of the x and y which contributes MCP-PMT hits more than the rest.

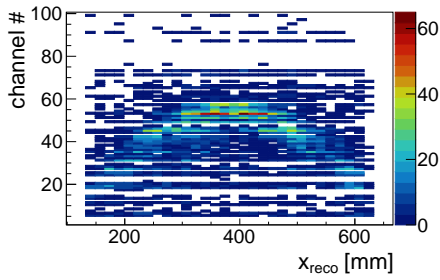
A. Appendix



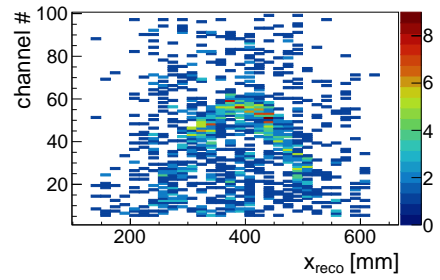
(a) Data, $|\phi| < 0.5 \text{ rad}$, $12^\circ < \theta < 14^\circ$



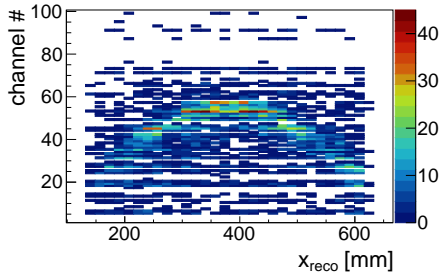
(b) MC, $|\phi| < 0.5 \text{ rad}$, $12^\circ < \theta < 14^\circ$



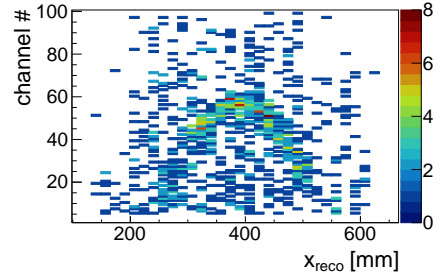
(c) Data, $|\phi| < 0.3 \text{ rad}$, $12^\circ < \theta < 14^\circ$



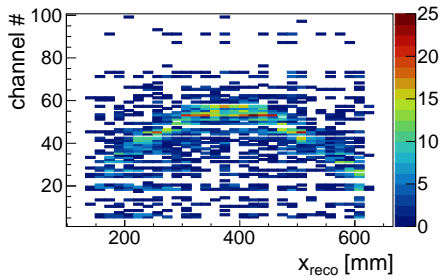
(d) MC, $|\phi| < 0.3 \text{ rad}$, $12^\circ < \theta < 14^\circ$



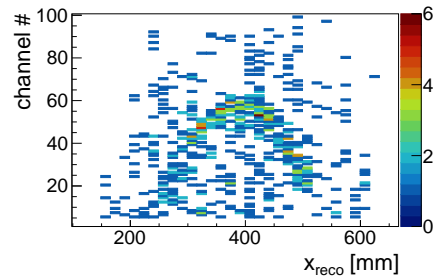
(e) Data, $|\phi| < 0.2 \text{ rad}$, $12^\circ < \theta < 14^\circ$



(f) MC, $|\phi| < 0.2 \text{ rad}$, $12^\circ < \theta < 14^\circ$



(g) Data, $|\phi| < 0.1 \text{ rad}$, $12^\circ < \theta < 14^\circ$



(h) MC, $|\phi| < 0.1 \text{ rad}$, $12^\circ < \theta < 14^\circ$

Figure A.2.: Cherenkov photons as a function of position and MCP-PMT channels.

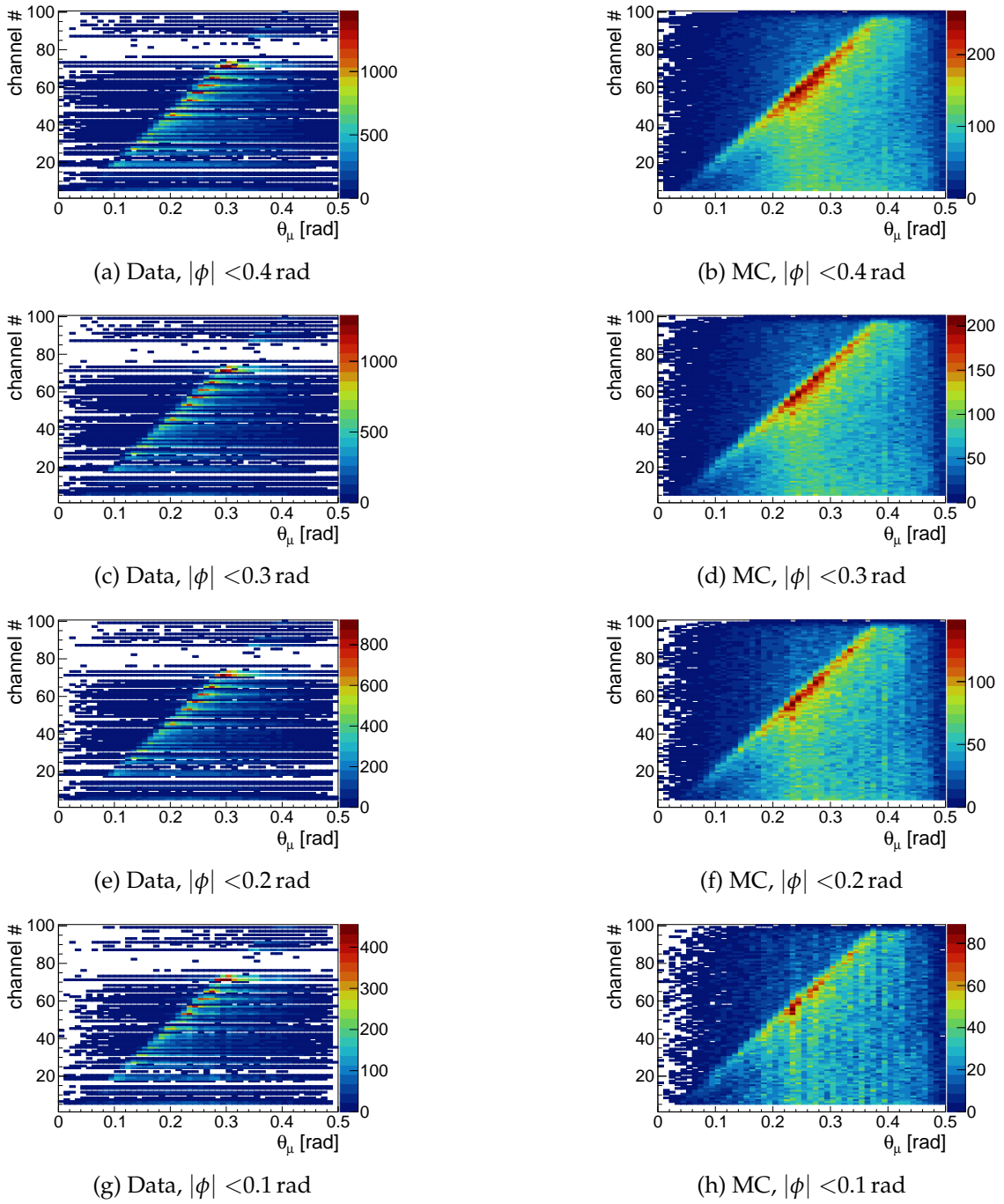
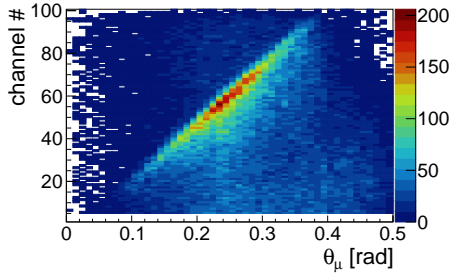
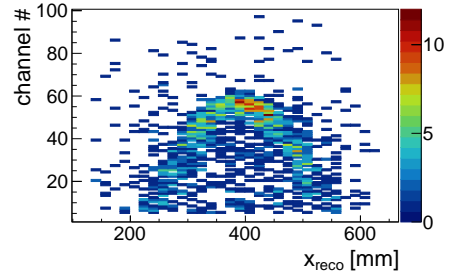


Figure A.3.: Cherenkov photons as a function of polar angle and MCP-PMT channels without energy cut.

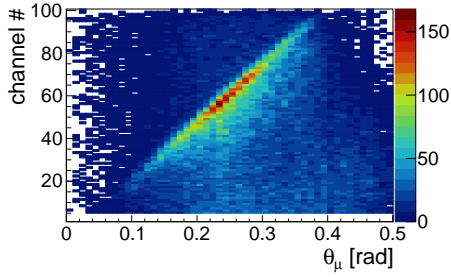
A. Appendix



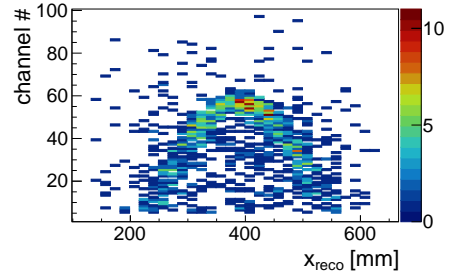
(a) MC, $|\phi| < 0.4$ rad



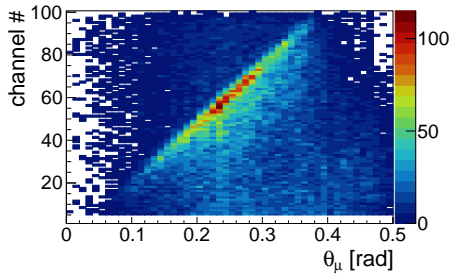
(b) MC, $|\phi| < 0.4$ rad



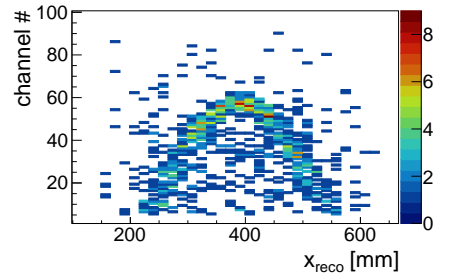
(c) MC, $|\phi| < 0.3$ rad



(d) MC, $|\phi| < 0.3$ rad



(e) MC, $|\phi| < 0.2$ rad



(f) MC, $|\phi| < 0.2$ rad

Figure A.4.: Cherenkov photons as a function of MCP-PMT channels and angle information. The $12^\circ < \theta < 14^\circ$ and energy cut were applied.

Acknowledgements

After the end of this work, I was planning to write this part in Turkish. Fortunately, I ended up to write in both languages since colleagues and my family can understand it. I can easily say that the times I had in this group were the best time of my work-life experience. My most important thanks go to the head of the group who accepted me as a Ph.D. student, Michael Düren. He gave me great support and a lot of freedom about my studies besides his permanent positive attitude. Secondly, I thank HGS-HIRE graduate school for supporting me financially during my Ph.D. studies. Moreover, I want to thank Sören Lange for his suggestions, positive approach, and continuous support during my studies. In addition, I would like to thank my former colleague and Ph.D. mentor Erik Etzelmüller for all information he provided me and his support.

Now, I come to the part to thank my colleagues who became friends during these three years. From time to time it is getting difficult of being an expat in Germany due to the language barrier. During all the struggles I faced, I always know my colleagues were happily ready to help me. These are namely Mustafa Schmidt and Marc Strickert. Mustafa was always very easy to communicate with whenever I have questions. We had many discussions about Ph.D. studies, life, future career plans, etc. I thank him for all. Marc is a great friend and colleague that one can luckily meet. Whenever I had a problem, he took care like it is his problem. I learned him to be patient, focused, efficient, and more environment friendly. I also want to thank him a lot. In addition to them, I would like thank my office-mate Avetik Hayrapetyan for all discussions, laughs, and food we shared. It was my pleasure to share an office with him. Simon Bodenschatz, a Ph.D. student was always there for any discussion. I also thank him for all. Furthermore, the rest of our group, I thank you all for all meetings, discussions we had.

Besides the research community, my all special thanks go to my lovely, supportive, positive, happy tiny family. My father Osman Köseoğlu is the luck of my life. Throughout the years, I never heard him complaining to be tired or bored. Because I had to learn to survive under stress and negative conditions, he was always the first person I call in any situation. My mother Aysel Köseoğlu always had health problems but never quit fighting for life. I learned that attribute from her and always laugh at any time. The love I received from my family was always unconditional. A simple thank is not enough to explain my feelings to them. I dedicate this work to my mother and father. Last but not least, I thank my husband Gökay Sarı for his endless support and loving care.

A. Appendix

Türkçe Versiyonu (Turkish Version)

Tezi bitirdikten sonra bu kısmı Türkçe yazmayı planlamıştım. Sonunda iki dilde yazmaya karar verdim, böylece hem iş arkadaşlarımın hem de ailemin anlayabileceğini düşündüm. Rahatlıkla söyleyebilirimki iş hayatımdaki en iyi deneyim burdaki çalıştığım grupta edindiğim deneyimdi. Teşekkürümün en büyük kısmı grubumuz başı olan ve beni doktora öğrencisi olarak kabul eden Michael Düren'e gidiyor. Michael doktora çalışmalarım süresince her zaman olumlu davrandı, özgür hissetmemi sağladı ve beni hep destekledi. İkinci olarak doktora çalışmalarımı yapabilmem için finansal olarak beni destekleyen HGS-HIRE okuluna da teşekkür ediyorum. Aynı zamanda, Sören Lange'ye önerileri, olumlu yaklaşımı ve devamlı desteği için teşekkür ediyorum. Buna ek olarak, doktora ilerleme komitemdeki mentorum ve eski iş arkadaşım Erik Etzelmüller'e bilgilerini benimle paylaştığı ve beni desteklediği için teşekkür ediyorum.

Artık üç yıl içinde arkadaşlığa dönüşen iş arkadaşlarıma teşekkür ettiğim kısma gelebilirim. Zaman zaman Almanya'da yaşayan bir yabancı olmak dil açısından beni çok zorladı. Bu durumlarda her zaman yardıma hazır iş arkadaşlarımın, Mustafa Schmidt ve Marc Strickert, olduğunu bilmek bana çok büyük bir destek oldu. Mustafa her zaman için rahatlıkla iletişim kurabildiğim, çalışmalarımı, gelecek planlarımı ve hayatla ilgili bir çok konuyu tartıştığım biriydi. Tüm bunlar için kendisine çok teşekkür ediyorum. Marc da bir insanın şans eseri denk gelebileceği kadar iyi bir arkadaş. Ne zaman bir problemim olsa, her zaman kendi sorunuymuş gibi yaklaşıp bana destek oldu. Ondan odaklanmayı sabırlı, verimli ve daha çok çevreci olmayı öğrendim. Her şey için kendisine çok teşekkür ederim.

Tüm araştırma grubumun yanı sıra, tüm özel ve en büyük teşekkürüm sevgi dolu, destekleyici, mutlu küçük aileme gidiyor. Babam Osman Köseoğlu bu hayattaki şansım oldu. Yıllar boyu onun bir kere bile yorulduğunu ya da sıkıldığını görmedim. Tüm zorluklarla ve aşırı stresli durumlarla nasıl mücadele etmem gerektiğini ondan öğrendim. Her zaman başıma ne gelirse gelsin ilk onu aradım. Annem Aysel Köseoğlu sağlık problemlerine rağmen asla pes etmedi ve her zaman hayat içinde mücadelesine devam etti. Gülmeyi, mücadeleyi, koşulsuz sevgiyi onlardan öğrendim. Basit bir teşekkürün duygularımı açıklaması mümkün olmayacaktır. Bu çalışmayı annem Aysel Köseoğlu ve babam Osman Köseoğlu'na adıyorum. En son olarak da ama en çok da eşim Gökay Sarı'ya beni her zaman desteklediği ve sevgi dolu ilgisi için çok teşekkür ediyorum.

List of Figures

2.1. The sketch of FAIR with existing facilities, planned facilities, and experiments [SSS15].	4
2.2. The 3D drawing of PANDA detector [pan20a]. The detectors labeled in red will be installed in second phase of the project.	6
2.3. First: The fixed target system with a beam pipe [tar20]. Second: Cluster jet targets are separated from a hydrogen gas via Laval-type nozzle and the skimmers. Third: The pellet target with a liquid hydrogen is turned out to be frozen pellets via cooling system, nozzle movements and triple-point chamber [Mer14].	7
2.4. The 3D drawings of the target detectors in TS of PANDA. Image sources STT [PANDA13], MVD [E ⁺ 12], Electron microscope picture of a typical GEM structure photo [PANDA14], GEM 3D drawing	8
2.5. The CAD drawings of Cryostat (left) [sol21] in TS and Dipole magnet (right) [dip21] in FS.	10
2.6. The CAD drawing of the calorimeters in PANDA. 1: Barrel EMC and forward Endcap EMC with crystals [Alb15]. 2: 3D drawings from the step file from actual PANDA geometry, Shaslyk calorimeter in the FS. 3: Drawing of Backward Endcap EMC with crystals (blue), beam pipe and MVD tracking detector.	11
2.7. PANDA subdetectors for particle identification in TS and FS [pan20a]. The beam is coming from the left.	12
2.8. Barrel DIRC with its fundamental elements.	13
2.9. Data rates of subdetectors [PAN20b].	15
2.10. PANDA readout system leading from analogue front-ends to a PC farm for final event filtering [PAN20b].	16
2.11. The preliminary design of the data concentrator with labels [PAN20b]. . .	17
2.12. The scheme of the readout system starting from the data concentrator level of the subdetector [PAN20b].	19
2.13. The SODANET based synchronization system of the PANDA readout [PAN20b].	20
2.14. The mass of generated hadronic states as a function of antiproton momentum provided by the PANDA experiment [PANDA09b].	21
2.15. The graph shows the charmonium spectrum with predicted-discovered, predicted-undiscovered and unpredicted-discovered states [BESIII13]. . .	22

List of Figures

3.1.	The location of the particle identification is shown in the scheme depending on the detector type which are Particle Tracking (PT), Electromagnetic Calorimeter (EMC), Hadronic Calorimeter (HCAL) and MUon Chambers (MUC).	24
3.2.	Truncated mean values of dE/dx as a function of reconstructed momentum for electrons, muons, pions, kaons and protons in STT of the PANDA detector [PANDA13].	25
3.3.	π/K separation power for three different σ values as a function of particle momentum and time resolution of ToF stations [Mer14].	27
3.4.	A positively charged particle traverses a transparent medium, it polarizes the atoms nearby. The upper sketch shows the wavefronts when a particle is moving faster than local speed of light ($\beta > 1/n(\lambda)$) in the medium. The bottom left sketch shows when the speed of charged particle is not higher than local speed of light ($\beta < 1/n(\lambda)$). The polarization of this effect is visualized at bottom right.	28
3.5.	Left: Dispersion of Cherenkov angle depending on a wavelength in the visible spectrum which is $300\text{ nm} \leq \lambda \leq 700\text{ nm}$. Right: Zoomed version.	30
3.6.	(a) Thick radiator with a smearing effect, (b) two different aerogel layers with refractive indexes $n_1 < n_2$, (c) two different aerogel layers with the refractive indexes $n_1 > n_2$ causes a larger Cherenkov ring, (d) three different layers with refractive indexes $n_1 < n_2 < n_3$ creates a very precise Cherenkov ring image by index matching, (e) with refractive indexes $n_2 > n_1 > n_4 > n_3$ similar behavior as in scenario (b).	31
3.7.	The upper left sketch illustrates the lens focusing of Cherenkov photons created by charged particle by conserving the angle information during internal reflections. The upper right sketch shows mirror focusing of Cherenkov photons. The bottom left sketch shows the proximity focusing. The bottom right sketch shows the detection without any imaging. Here TOP is used to extract the Cherenkov angle.	32
4.1.	1: Top view of the radiator with three FELs. The angle between the charged particle and the FEL is α_{FEL} . 2: The isometric view of the radiator with the position of charged particle traversed. 3: The side view of the setup with a Cherenkov cone (red) and the angles.	36
4.2.	Exploded CAD view of the EDD with the main components.	37
4.3.	Left: A quadrant with exemplary particle tracks. The green arrow represents the charged particle, where the purple ones are the photons. There are 24 ROMs at the outer rim. Middle: From left drawing, the dashed black rectangular is in side-view. A charged particle traverses the radiator and its emitted Cherenkov photons are internally reflected and focused on the MCP-PMT sensor. Right: The MCP-PMT photocathode and the ASIC readout.	39

4.4.	Left: The TS of the PANDA detector from the side view. The EDD is sandwiched between the Gas Electron Multiplier (GEM) and Electro Magnetic Calorimeter (EMC) detectors. Middle: The EDD view with hidden neighboring detectors. Right: The EDD in full size with its four quadrants.	40
4.5.	Left: The magnetic field depending on the position in the Endcap region ($z = 200$ cm). Right: Magnetic field distribution depending on the distance from the interaction point is shown. The limits of the FEL and the radiator are shown with black frames in the magnetic field region [Mer14].	42
4.6.	The GEM cable bundle is colliding with the MP of EDD.	42
4.7.	Left: The framed parts show the limited spatial regions for EDD in the z -direction. Right: The ROM position differs due to the EMC insulation in the radial direction.	43
4.8.	The efficiency at 4 GeV/c momentum depending on the number of ROMs based on a MC simulation.	44
4.9.	Top: Analog SiPM (aSiPM) structure with a readout system. Bottom: Digital SiPM (dSiPM) structure with a CMOS technology. [HFDT12].	45
4.10.	The working principle of the MCP-PMT is sketched in the left figure. Right side refers to the HV-divider that provides the required voltage gradient between photocathode, MCP-in, MCP-out and ground. The electron multiplication is visualized for adjacent micro-channels. As a result the output signal reaches the MCP pins. The right plot shows the signal amplitudes of three neighboring pins due to the charge sharing [Rie17].	46
4.11.	Left: A straight structure of the MCP-PMT pores with an incoming electron is shown. Right: The Chevron geometry of the pore structure is visualized.	47
4.12.	1: The readout system in 2015 test beam experiment based on TRBv3 with PaDiWa boards [Etz17]. 2: TOFPET readout system was used in 2016 test beam experiments [Sch17]. 3: TOFPET based final readout system was suggested in 2015 [Mer14].	49
4.13.	TOFPET2 system with FEM128 and FEBD-v2 board.	51
4.14.	The bottom side of the mother board is connected to the FEM directly or via cable.	52
4.15.	Space constraints in one of the limited regions.	53
4.16.	Left: The sketch of the signal flow for custom design PCB, starting from the MCP-PMT signals to FPGA board. Right: The sketch of the custom design PCB with inner view focus towards the ROM surface.	54
4.17.	Three different design for the limited regions.	55
4.18.	3D CAD version of the custom design PCB from outer and inner view.	58
4.19.	The sketch of the box designed for testing the custom designed PCB.	59
4.20.	The 3D drawing of the light-tight box for testing purposes of custom design PCB. 1: The isometric view of a closed box. 2: The inside of the box with PCB implemented in a horizontal way. 3: Top view of the box. 4: The box with a vertically positioned PCB.	60

List of Figures

4.21.	The inner side of the PCB is shown with hot spots pointing to the corresponding cooling items in the bottom 3D drawing designed [Was21]. . . .	62
4.22.	1: The sensor holder for the ROM case. Two blue heat pipes aligned on the sides, yellow pipe aligned on top. 2: The side view of the ROM case: bars, FELs, adaptor board between the sensor and PCB, heat pipes and two screw holes for stabilization. 3: The front view of the custom design PCB attached to the ROM.	63
4.23.	The DAQ system for phase-1 will be the same system that is used for GCS.	64
4.24.	Two different communication scenarios between the PANDA DAQ system.	65
5.1.	The momentum spectrum of cosmic muons from different experiments when $\theta = 0^\circ$. The shifted distribution to the right is for $\theta = 75^\circ$. The source of the image is [Group16].	68
5.2.	1: The grid structure of the SiPM layers by aligning them perpendicular each other in two tracking boxes. 2: The full size fused silica radiator plate in the clean-room with the assigned edges. 3: The Giessen Cosmic Station with elements: trigger plates, tracking boxes, radiator and ROMs.	69
5.3.	A sketch of the GCS.	71
5.4.	The design of the light-tight cases for the radiator plate and ROMs from the side view [1] and the isometric view [2]. The isometric view of the ROM case [3] [Was21].	72
5.5.	Three different photos of the radiator case. The upper left one shows the plastic screw for finer horizontal alignment. The upper right photo shows the radiator placed on the soft plastic screws. Lower photo shows the sliding window, and fixed position of the side plate for an example.	73
5.6.	Left: The test setup of the recent production of the ASICs. The negative signals from the pulser are provided Right: One FEM128 board with two ASICs facing to each other. The red cable shows the ground connection between the cable and FEM128 board.	74
5.7.	The MCP-PMT signal (green) and pulser signal (purple).	75
5.8.	1: One ROM is coupled to the edge of the radiator. The red circle shows the coupling between the bars and the radiator. The soft materials provide a distance between the bottom lid and the radiator. 2: The perspective is from the back side of the radiator. Blue Samtec cables from the side of the radiator case carries analog signal from the MCP-PMT pins and reach FEMs. The FEMs are cooled with fans. The red cable from the right side provides high-voltage (2250 V) for the sensor. 3: The cooling system was changed to liquid-based system. This element is 4 m far away from the Huber cooling device. Liquid enters the copper plate from the right copper pipe, travels through the U-shaped copper pipe soldered to the copper plate, and leaves from the left side. 4: The top view of the plate. The sides of A,B,C, and D have a thermal pad to provide a thermal connection. . . .	76
5.9.	The readout scheme of the GCS.	77

5.10. Upper plots: The reconstructed positions of the muon hits on the radiator from the collected data. Bottom plots: The reconstructed position of the muons from generated GEANT4-MC results. The hits are plotted if there is a coincidence with at least one Cherenkov hit.	79
5.11. The polar and azimuth angle distribution of data and MC for four fold coincidence from tracking boxes.	80
5.12. Time difference between MCP-PMT channels and closest tracking box-4. The right plot shows the projection of x -axis of the left plot. There is noise in the shape of the vertical repeating patterns.	81
5.13. Hit count distributions for x and y showing positions with excessive activities.	82
5.14. Time difference between the two boxes independent from MCP-PMT hits. Two bars in box two timing create noise which is shown in right plot as a projection of channel 45 from the left plot.	82
5.15. Cherenkov photons were reconstructed as a function of the polar angle θ and channels of MCP-PMT.	83
5.16. These plots were created in the same way of Figure 5.12 with all bars implemented. The difference is that the bars with bad timing behaviour were excluded for these plots which caused the repeating patterns.	83
5.17. Characteristic Cherenkov photon patterns as a function of polar angle. For upper two plots, no cuts on data and MC were implemented. For the bottom plots, the cuts on azimuth angle and time were implemented $ t_{ch} - t_{box4} < 5 \text{ ns}, \phi < 0.5 \text{ rad}$	84
5.18. Preliminary results of Cherenkov smiles for data (left) and MC (right). Upper plots without any cut and bottom ones show pattern with the cuts $ t_{ch} - t_{box4} < 5 \text{ ns}, \phi < 0.4 \text{ rad}, 12^\circ < \theta < 14^\circ$ applied.	85
5.19. Preliminary results of reconstructed Cherenkov angles for data (left) and MC (right). Upper plots without any cut and bottom ones show pattern with the cuts applied.	86
5.20. Cherenkov angles were fit for MC and data, after the applied cuts. Angle cuts were applied for both: $ \phi < 0.1 \text{ rad}, 12^\circ < \theta < 14^\circ$ Left: Cherenkov angle distribution, Right: with two Gaussian fitting.	87
5.21. MC results with energy cut and angle cuts were applied $ \phi < 0.1 \text{ rad}, 12^\circ < \theta < 14^\circ$	87
6.1. CERN PS/T9 beam time facility. The mixed π/p beam enters from the left.	89
6.2. Upstream view of the Disc DIRC prototype with geometric dimensions in mm. The beam position is indicated by red dots for the scan, and red A represents the fixed beam position while the angle of the prototype is changed with respect to the beam direction.	91
6.3. ROM preparation steps.	92
6.4. The steps of cleaning the radiator and coupling the ROMs.	93
6.5. Simplified diagram of the channel readout architecture [BFF ⁺ 19].	94

List of Figures

6.6.	The readout system of the EDD 2018 prototype.	95
6.7.	The flowchart of the analysis code for the beam time data (left) and MC (right).	97
6.8.	Left: Channel hits as a function of the time difference between the laser signal and the time of the signal, before the correction. Right: Channel hits as a function of time difference between laser signal and signal time, after the correction.	98
6.9.	Left: The time difference between the reference channel and the laser. Right: The delay between the reference channel and the other channels.	98
6.10.	The φ angle distribution as a function of MCP-PMT channels for data and MC.	99
6.11.	The x -axis shows time difference in [ps] between MCP-TOF stations, y -axis shows number of events, starting from left upper to the right bottom, 3 GeV/c to 10 GeV/c respectively.	101
6.12.	The time difference between TOF1 and sensor channels at 10 GeV/c momenta at $y = 243$ mm, $x = 422$ mm	102
6.13.	The distribution of reconstructed Cherenkov angles at different vertical positions at 10 GeV/c momentum.	103
6.14.	Cherenkov photons as a function of channel distribution and vertical axis at 10 GeV/c.	104
6.15.	Single photon resolution and Cherenkov angle distribution at 10 GeV/c.	104
6.16.	The Cherenkov smile for MC (left) and data (right) after excluding background.	105
6.17.	The number of photon hits per trigger for MC simulation and measured data.	106
6.18.	The time difference between two MCP-TOF counters at 7 GeV/c momentum was used for particle identification.	106
6.19.	Cherenkov photons create a pattern for pions (left) and protons (right) as a function of the pixel and vertical position.	107
6.20.	Left: Cherenkov angle reconstruction for different vertical positions. Right: SPR for different vertical positions.	108
6.21.	The angle of the radiator position with respect to beam axis.	108
6.22.	Cherenkov photons depending on the angle of the prototype at 7 GeV/c for pions (left) and protons (right).	109
6.23.	Left: Cherenkov angle reconstruction for different vertical positions. Right: Cherenkov angle reconstruction for different angle settings.	109
6.24.	Left: Pixel distributions for proton and pion for AOI at 7 GeV/c. Right: Pixel distribution for different vertical position at 7 GeV/c.	110
6.25.	The hit pattern of Cherenkov photons for different vertical positions at 7 GeV/c for MC simulation (left) and measured data (right).	110
6.26.	The number of hits of measured data is compared with MC simulations for different positions at 7 GeV/c momentum.	111

6.27. The beam position is shown on the radiator. The green dashed lines represent the track a photon may follow. The gray line shows the rotation of the radiator with respect to normal of the beam axis.	112
6.28. Cherenkov photons as a function of MCP-PMT channel of different FELs for pion and proton is shown at 6 GeV/c.	113
6.29. The MC simulation of the dispersion effect is compared to the measured data of pions and protons depending on momentum.	114
A.1. Specific position of the x and y which contributes MCP-PMT hits more than the rest.	117
A.2. Cherenkov photons as a function of position and MCP-PMT channels. . .	118
A.3. Cherenkov photons as a function of polar angle and MCP-PMT channels without energy cut.	119
A.4. Cherenkov photons as a function of MCP-PMT channels and angle information. The $12^\circ < \theta < 14^\circ$ and energy cut were applied.	120

List of Tables

4.1. Required voltages and currents for the TOFPET2 electronic components.	52
6.1. The position of the ROMs and the FELs during the test beam experiment at CERN.	92
6.2. The scans at different positions and/or different momenta.	100

Bibliography

- [3la21] SCHOTT AG, SCHOTT glass catalogue, https://www.schott.com/d/advanced_optics/094a6f8c-f648-45cd-a5fe-ca7df5474fcb/1.2/schott-optical-glass-pocket-catalog-europe-october-2011-eng.pdf?highlighted_text=N-LaK33B+glass, accessed 2021.
- [A⁺02] N. Akopov et al., *The HERMES dual-radiator ring imaging Cherenkov detector*, Nuclear Instruments and Methods in Physics Research Section A: Accelerators, Spectrometers, Detectors and Associated Equipment **479**(2-3), 511–530 (2002).
- [A⁺03] S. Agostinelli et al., *Geant4 – a simulation toolkit*, Nuclear Instruments and Methods in Physics Research Section A: Accelerators, Spectrometers, Detectors and Associated Equipment **506**(3), 250 – 303 (2003).
- [A⁺05] I. Adam et al., *The DIRC particle identification system for the BaBar experiment*, Nuclear Instruments and Methods in Physics Research Section A: Accelerators, Spectrometers, Detectors and Associated Equipment **538**(1), 281 – 357 (2005).
- [Alb15] M. Albrecht, *The Forward Endcap of the Electromagnetic Calorimeter for the PANDA Detector at FAIR*, Journal of Physics: Conference Series **587**, 012050 (2015).
- [B⁺20] M. Böhm et al., *Performance of the most recent MCP-PMTs*, **15**(11) (2020).
- [BDH⁺20] S. Bodenschatz, M. Düren, A. Hayrapetyan, I. Köseoglu, M. Strickert and M. Schmidt, *The Giessen Cosmic Station—A muon telescope for tests of particle detectors*, Journal of Instrumentation **15**(06) (2020).
- [BESIII13] J. Messchendorp (BESIII Collaboration), *Physics with Charmonium – A few recent highlights of BESIII*, PoS , 043 (2013), 1306.6611.
- [BFF⁺19] R. Bugalho, A. D. Francesco, L. Ferramacho, C. Leong, T. Niknejad, L. Oliveira, M. Rolo, J. Silva, R. Silva, M. Silveira, S. Tavernier and J. Varela, *Experimental characterization of the TOFPET2 ASIC*, Journal of Instrumentation **14**(03) (2019).
- [BR97] R. Brun and F. Rademakers, *ROOT: An object oriented data analysis framework*, Nucl. Instrum. Meth. A **389**, 81–86 (1997).

Bibliography

- [C⁺11] E. Cowie et al., *A focussing disc DIRC for PANDA*, Nuclear Instruments and Methods in Physics Research Section A: Accelerators, Spectrometers, Detectors and Associated Equipment **639**(1), 181–184 (2011), Proceedings of the Seventh International Workshop on Ring Imaging Cherenkov Detectors.
- [C⁺17] M. Caselle et al., *A high-speed DAQ framework for future high-level trigger and event building clusters*, Journal of Instrumentation **12**(03) (2017).
- [CER] CERN, *FEASTMP, Radiation and magnetic field tolerant 10W DC/DC converter module*.
- [Che34] P. A. Cherenkov, *Visible emission of clean liquids by action of γ radiation*, Doklady Akademii Nauk **2**(451) (1934).
- [Cho10] W. S. Choong, *Investigation of a Multi-Anode Microchannel Plate PMT for Time-of-Flight PET*, IEEE Transactions on Nuclear Science **57**(5), 2417–2423 (2010).
- [Col15] T. G. Collaboration, *GlueX FDIRC Technical Design Report*, https://halldweb.jlab.org/DocDB/0028/002809/003/dir_c_tdr.pdf, 2015.
- [Dim14] C. Dimopoulou, *Beam Cooling Systems and Activities at GSI and FAIR*, in *5th International Particle Accelerator Conference*, page MOPRI067, 2014.
- [dip21] Dipole Magnet, <https://panda.gsi.de/article/dipole-magnet>, accessed January 2021.
- [E⁺12] W. Erni et al., *Technical Design Report for the: PANDA Micro Vertex Detector*, 2012.
- [Etz17] E. Etzelmüller, *Developments towards the technical design and prototype evaluation of the PANDA Endcap Disc DIRC*, PhD thesis, University of Giessen, Gießen, 2017.
- [Fas17] J. Fast, *The Belle II imaging Time-of-Propagation (iTOP) detector*, Nuclear Instruments and Methods in Physics Research Section A: Accelerators, Spectrometers, Detectors and Associated Equipment **876**, 145–148 (2017), The 9th international workshop on Ring Imaging Cherenkov Detectors (RICH2016).
- [Föh09] K. Föhl, *A Focussing Disc DIRC design for particle identification in PANDA*, Hyperfine Interactions **194**(1), 171 (2009).
- [FT37] I. M. Frank and I. E. Tamm, *Coherent visible radiation of fast electrons passing through matter*, Compt. Rend. Acad. Sci. URSS **14**(3), 109–114 (1937).

- [G⁺83] H. D. Glass et al., *Construction and Operation of a Large Ring Imaging Cherenkov Detector*, IEEE Trans. Nucl. Sci. **30**, 30–34 (1983).
- [Group13] M. Adinolfi et al. (LHCb RICH Group Collaboration), *Performance of the LHCb RICH detector at the LHC*, Eur. Phys. J. C **73**, 2431 (2013), 1211.6759.
- [Group16] C. Patrignani et al. (Particle Data Group Collaboration), *Review of Particle Physics*, Chin. Phys. **C40**(10), 100001 (2016).
- [H⁺20] T. H. Hancock et al., *Beam tests of a large-scale TORCH time-of-flight demonstrator*, Nucl. Instrum. Meth. A **958**, 162060 (2020), 1904.11235.
- [HAM] HAMAMATSU, <https://www.hamamatsu.com/eu/en/index.html>, accessed 2020.
- [HERMES98] K. Ackerstaff et al. (HERMES Collaboration), *The HERMES spectrometer*, Nucl. Instrum. Meth. A **417**, 230–265 (1998), hep-ex/9806008.
- [HFDT12] Y. Haemisch, T. Frach, C. Degenhardt and A. Thon, *Fully Digital Arrays of Silicon Photomultipliers (dSiPM) a Scalable Alternative to Vacuum Photomultiplier Tubes (PMT)*, Physics Procedia **37**, 1546 – 1560 (2012), Proceedings of the 2nd International Conference on Technology and Instrumentation in Particle Physics (TIPP 2011).
- [JT] L. O. J. Troska, C. Soos, *The Versatile Link+ Application Note*, CERN.
- [Kal20] G. Kalicy, *Developing high-performance DIRC detector for the future Electron Ion Collider experiment*, Journal of Instrumentation **15**(11) (2020).
- [KAO⁺96] T. Kamae, K. Arai, T. Ohtsuka, N. Tsuchida and H. Aihara, *Focussing DIRC — A new compact Cherenkov ring imaging device*, Nuclear Instruments and Methods in Physics Research Section A: Accelerators, Spectrometers, Detectors and Associated Equipment **382**(3), 430–440 (1996).
- [KPS⁺07] U. Krause, W. Panschow, V. Schaa, W. Schiebel, P. Schuett and R. Baer, *The New FAIR Accelerator Complex at GSI: Project, Controls challenges and First steps*, (2007).
- [L⁺20] A. Lehmann et al., *Latest improvements of microchannel-plate PMTS*, Nucl. Instrum. Meth. A **958**, 162357 (2020).
- [Mer14] O. Merle, *Development, design and optimization of a novel Endcap DIRC for PANDA*, PhD thesis, University of Giessen, Gießen, 2014.
- [PAN05] PANDA collaboration, *Technical Progress Report*, FAIR-ESAC/Pbar **75** (2005).

Bibliography

- [PAN12] PANDA collaboration, *Technical Design Report for the PANDA muon system*, (2012).
- [PAN18] PANDA collaboration, *Technical Design Report for the PANDA Luminosity Detector*, (2018).
- [pan20a] Clickable PANDA detector, <https://panda.gsi.de/panda>, accessed December 2020.
- [PAN20b] PANDA collaboration, *Technical Design Report for the: PANDA Data Acquisition and Event Filtering*, (2020).
- [PANDA08] W. Erni et al. (PANDA Collaboration), *Technical Design Report for PANDA Electromagnetic Calorimeter (EMC)*, (2008), 0810.1216.
- [PANDA09a] W. Erni et al. (PANDA Collaboration), *Technical Design Report for the PANDA Solenoid and Dipole Spectrometer Magnets*, (2009), 0907.0169.
- [PANDA09b] I. Lehmann (PANDA Collaboration), *Physics Programme of PANDA at FAIR*, in *18th International Conference on Particles and Nuclei*, pages 408–410, 2009.
- [PANDA09c] M. Lutz et al. (PANDA Collaboration), *Physics Performance Report for PANDA: Strong Interaction Studies with Antiprotons*, (2009), 0903.3905.
- [PANDA12] A. Khoukaz et al. (PANDA Collaboration), *Technical Design Report for the PANDA Internal Targets: The Cluster-Jet Target and Developments for the Pellet Target*, (2012).
- [PANDA13] W. Erni et al. (PANDA Collaboration), *Technical design report for the PANDA (AntiProton Annihilations at Darmstadt) Straw Tube Tracker*, *Eur. Phys. J. A* **49**, 25 (2013), 1205.5441.
- [PANDA14] B. V. D. Melnychuk and B. Zwieglinski (PANDA Collaboration), *Study of resolution of the PANDA GEM detector with Garfield*, (2014).
- [PANDA17a] W. Kühn et al. (PANDA Collaboration), *Data Acquisition and Online Event Selection for the PANDA Experiment*, doi:10.7566/JPSCP.18.011035, 2017.
- [PANDA17b] B. Singh et al. (PANDA Collaboration), *Technical Design Report for the PANDA Barrel DIRC Detector*, (2017), 1710.00684.
- [PANDA17c] B. Singh et al. (PANDA Collaboration), *Technical Design Report for the Panda Forward Spectrometer Calorimeter*, (2017), 1704.02713.
- [PANDA20] I. Köseoglu (PANDA Collaboration), *Design of the barrel and endcap DIRC detectors for particle identification in PANDA*, *Int. J. Mod. Phys. A* **35**(34n35), 2044020 (2020).

- [PANDA21] G. Barucca et al. (PANDA Collaboration), *PANDA Phase One*, (2021), 2101.11877.
- [pet20] PETsys Electronics, <https://www.petsyselectronics.com/web/>, accessed January 2020.
- [PHO] PHOTONIS, <https://www.photonis.com>, accessed 2020.
- [Pra14] D. Prasuhn, Status HESR, in *Status HESR*, 2014.
- [Rie17] J. Rieke, *Design of a compact photon detection system for the PANDA Disc DIRC prototype*, PhD thesis, University of Giessen, Gießen, 2017.
- [RV20] B. Ratcliff and J. Va'vra, *DIRC: Internally reflecting imaging Cherenkov detectors*, Nuclear Instruments and Methods in Physics Research Section A: Accelerators, Spectrometers, Detectors and Associated Equipment **970**, 163442 (2020).
- [S⁺94] H. W. Siebert et al., *The Omega RICH*, Nuclear Instruments and Methods in Physics Research Section A: Accelerators, Spectrometers, Detectors and Associated Equipment **343**, 60–67 (1994).
- [S⁺20] C. Schwarz et al., *The PANDA DIRCs*, JINST **15**(09), C09059 (2020), 2101.10930.
- [sam21] Samtec, <https://www.samtec.com>, accessed January 2021.
- [SC00] M. S. S. Cecchini, *Cosmic Ray Muon Physics*, CERN Document Server (hep-ex/0002052) (2000).
- [Sch17] M. A. Schmidt, *Particle identification with the Endcap Disc DIRC for PANDA*, PhD thesis, University of Giessen, Otto-Behaghel-Str. 8, 35394 Gießen, 2017.
- [SKS⁺12] P. Sievers, K. Knie, M. Steck, B. Franzke and V. Gostishchev, *Concept for the Antiproton Production Target at FAIR*, Conf. Proc. C **1205201**, 2570–2572 (2012).
- [sol21] Solenoid Magnet, <https://panda.gsi.de/article/solenoid-magnet>, accessed January 2021.
- [SSS15] H. Stöcker, T. Stöhlker and C. Sturm, *FAIR - Cosmic Matter in the Laboratory*, Journal of Physics: Conference Series **623**, 012026 (2015).
- [SuperB13] M. Baszczyk et al. (SuperB Collaboration), *SuperB Technical Design Report*, (2013), 1306.5655.
- [tar20] Target and Beamline, <https://panda.gsi.de/article/target-and-beamline>, accessed December 2020.

Bibliography

- [U⁺13] C. Uğur et al., 264 Channel TDC Platform applying 65 channel high precision (7.2 psRMS) FPGA based TDCs, in *2013 IEEE Nordic-Mediterranean Workshop on Time-to-Digital Converters (NoMe TDC)*, pages 1–5, 2013.
- [Uhl15] F. Uhlig, *Charakterisierung und Anwendung von schnellen Photosensoren im Hinblick auf ihren Einsatz im PANDA Experiment*, doctoralthesis, Friedrich-Alexander-Universität Erlangen-Nürnberg (FAU), 2015.
- [uni20] UNILAC Overview, https://www.gsi.de/en/work/accelerator_operations/accelerators/unilac/unilac.htm, accessed December 2020.
- [Va'14] J. Va'vra, *Optical properties of RICH detectors*, Nuclear Instruments and Methods in Physics Research Section A: Accelerators, Spectrometers, Detectors and Associated Equipment **766**, 189–198 (2014), RICH2013 Proceedings of the Eighth International Workshop on Ring Imaging Cherenkov Detectors Shonan, Kanagawa, Japan, December 2-6, 2013.
- [Was21] T. Wasem, private communication, 2021.
- [Z⁺19] S. Zimmermann et al., *The PANDA barrel-TOF detector at FAIR*, Nuclear Instruments and Methods in Physics Research Section A: Accelerators, Spectrometers, Detectors and Associated Equipment **936**, 590 – 591 (2019), Frontier Detectors for Frontier Physics: 14th Pisa Meeting on Advanced Detectors.

Selbstständigkeitserklärung

Ich erkläre: Ich habe die vorgelegte Dissertation selbstständig und ohne unerlaubte fremde Hilfe und nur mit den Hilfen angefertigt, die ich in der Dissertation angegeben habe. Alle Textstellen, die wörtlich oder sinngemäß aus veröffentlichten Schriften entnommen sind, und alle Angaben, die auf mündlichen Auskünften beruhen, sind als solche kenntlich gemacht. Ich stimme einer evtl. Überprüfung meiner Dissertation durch eine Antiplagiat-Software zu. Bei den von mir durchgeführten und in der Dissertation erwähnten Untersuchungen habe ich die Grundsätze guter wissenschaftlicher Praxis, wie sie in der „Satzung der Justus-Liebig-Universität Gießen zur Sicherung guter wissenschaftlicher Praxis“ niedergelegt sind, eingehalten.